TECHNISCHE UNIVERSITÄT MÜNCHEN

Max-Planck-Institut für Quantenoptik

Coherent Dynamics and State Detection of Single Atoms in a Cavity

Jörg Bochmann

Vollständiger Abdruck der von der Fakultät für Physik
der Technischen Universität München
zur Erlangung des akademischen Grades eines

Doktors der Naturwissenschaften (Dr. rer. nat.)

genehmigten Dissertation.

Vorsitzender: Univ.-Prof. Dr. H. Friedrich

Prüfer der Dissertation:

1. Hon.-Prof. Dr. G. Rempe
2. Univ.-Prof. Dr. Dr. h.c. A. Laubereau

Die Dissertation wurde am 17.06.2010
bei der Technischen Universität München eingereicht
und durch die Fakultät für Physik am 12.07.2010 angenommen.

Abstract

A single quantum emitter embedded in an optical resonator provides a model system for the interaction of light and matter. This thesis reports on experiments in which a single Rubidium atom is coupled to a high-finesse optical cavity. For this purpose, a new apparatus has been constructed which enables quasi-permanent trapping of single atoms.

First, we study the excitation of the atom-cavity system with short laser pulses. We observe vacuum Rabi oscillations between the atom and the cavity field. Further, we show how the wave packet shape and frequency spectrum of the emitted single photons can be controlled. Our results are in excellent agreement with theory and illustrate the fundamentals of cavity quantum electrodynamics.

In a second experiment, we introduce efficient state detection of single neutral atoms based on cavity-enhanced fluorescence. We achieve a hyperfine-state detection fidelity of 99.4 % within 85 μs while the atom can be interrogated many hundreds times without loss from its trap.

Further, this thesis reports on the observation of electromagnetically induced transparency with a single atom and on the control of the optical phase of single-photon wave packets.

Kurzfassung

Ein einzelner Quantenemitter in einem optischen Resonator stellt ein Modellsystem für die Untersuchung der Wechselwirkung von Licht und Materie dar. Die vorliegende Arbeit beschreibt Experimente, in denen ein einzelnes Rubidiumatom an einen optischen Resonator hoher Finesse koppelt. Zu diesem Zweck wurde eine Apparatur aufgebaut, welche die quasi-permanente Speicherung einzelner Atome erlaubt.

Zunächst untersuchen wir die Anregung des gekoppelten Atom-Resonator-Systems mittels kurzer Laserpulse. Wir beobachten Vakuum-Rabi-Oszillationen zwischen Resonatorfeld und Einzelatom. Ferner zeigen wir, wie die Wellenpaketform und das Spektrum der emittierten Einzelphotonen kontrolliert werden können. Unsere Beobachtungen stimmen exzellent mit theoretischen Vorhersagen überein und illustrieren grundlegende Phänomene der Resonator-Quantenelektrodynamik.

Danach stellen wir eine effiziente Methode zur Zustandsdetektion einzelner Neutralatome vor. Mittels resonatorverstärkter Fluoreszenz erreichen wir eine Hyperfeinzustandsdetektion mit einer Sicherheit von 99,4 % innerhalb von 85 μs. Der Hyperfeinzustand kann dabei mehrere hundert Male ohne Atomverlust ausgelesen werden.

Desweiteren beschreibt die vorliegende Arbeit Experimente zur elektromagnetisch-induzierten Transparenz eines Einzelatoms und zur Kontrolle der optischen Phase einzelner Photonen.

Contents

1 Introduction

Current efforts in experimental physics aim at gaining control over fundamental quantum systems. On the one hand, this development is driven by scientific curiosity. What had been gedankenexperimente in the past can now be tested in real-world experiments ranging from tests of local realism to investigations of the measurement process in quantum physics [1, 2, 3, 4, 5, 6, 7]. On the other hand, the control of quantum phenomena is of increasing importance for technological progress. Already today, quantum effects are the basis for applications ranging from medical diagnostics [8] to information technology [9] and time standards [10, 11, 12]. These examples indicate that future technologies may not only need to cope with quantum phenomena but use them as a resource. What we witness today has therefore been termed a *second quantum revolution* which is marked by the control and application of quantum effects [13].

In modern quantum physics, information has become a central concept which reaches far beyond the traditional wave-particle duality and uncertainty relations. The potential of quantum physics for computing or communication purposes has already been recognized in the 1980's [14, 15, 16, 17]. In recent years, the promises of quantum information science have been driving forces for the progress of experimental quantum physics. A yet-to-be-built universal quantum computer not only incorporates all capabilities of a classical computer, but also solves certain problems more efficiently than its classical counterpart [18, 19, 20, 21, 22]. Alternatively, well-controlled model quantum systems are proposed to simulate problems of quantum physics [14, 23, 24, 25, 26]. Finally, quantum cryptography can provide intrinsically secure communication [27, 28, 29]. Some of the basic experimental requirements for exploring these vistas [30] have been summarized by diVincenzo [31].

Achieving control over fundamental quantum systems faces two conflicting requirements. While the "fragile" quantum objects must be isolated from the environment to avoid decoherence, the manipulation and measurement of the quantum system necessarily requires interaction with the environment. A desirable controlled coupling between quantum system and environment can be established using, for example, well-tailored electromagnetic fields which control isolated trapped atoms. Indeed, the interaction of light with matter is at the heart of quantum control as light can be used to prepare, manipulate, readout, and to connect quantum systems.

In this thesis, the interaction of light and matter is controlled at the level of single atoms and single photons. Scaling into this regime is achieved by coupling individual atoms to the mode of a high-finesse optical cavity. In this model system of quantum optics, the dynamics of a single atom interacting with single photon fields can be measured and controlled. The observed physical phenomena are naturally described by cavity quantum electrodynamics (CQED).

CQED is an active and rapidly progressing field of research. Today, its basic concepts have spread across very different fields of physics. A central idea of CQED is that the

radiative properties of a quantum emitter can be dramatically altered when boundary conditions are imposed on the electromagnetic field. It has been pointed out early by Purcell [32] that the atomic spontaneous emission rate is modified in the presence of a resonator. Moreover, embedding an atom into a cavity affects the energy spectrum of the system such that atom and resonator field can no longer be considered as separate entities [33, 34]. In fact, correlations between atomic state and cavity field occur and lead to intrinsic entanglement [35]. Likewise, a cavity can establish long-range interactions among multiple quantum emitters coupled to its field mode [36, 37].

Pioneering experiments in CQED have been performed with Rydberg atoms coupled to microwave cavities [38, 39, 40, 41, 42, 43] and have soon been followed by experiments in the optical domain [44, 45, 46, 47, 48, 49, 50]. The concepts of CQED are, however, applicable to a variety of other physical realizations, for example quantum dots embedded in microcavities [51, 52, 53, 54] or superconducting circuits coupled to strip-line cavities [55, 56, 57]. In the optical domain, new resonator concepts are currently emerging [58, 59, 60, 61, 62] aiming at ever higher coupling strength between light and matter. Another subject of interest is the study of back-action of the cavity field onto intracavity atoms or the resonator itself – which can be exploited for cooling and quantum state squeezing [63, 64, 65, 66, 67]. A fascinating perspective are distributed quantum networks of atom-cavity systems which allow the distribution and exchange of quantum information over large distances [68, 69].

This thesis reports on experiments in which a single Rubidium atom is coupled to a high-finesse optical cavity. These experiments have been performed in a new CQED apparatus which has been entirely constructed during the course of this thesis. The findings presented here are fundamental examples of quantum optics and mark a high level of control over single quanta of matter and light.

The new atom-cavity system is an ideal interface between single atoms and single photons. The parameters of the cavity are chosen to provide sufficient coupling of the intracavity field to a single atom as well as an efficient mapping of the intracavity field to the cavity output mode. Hence, the new system is well-suited for the controlled generation of single photons and for the readout of the intracavity field and atomic state. Moreover, quantum networking experiments based on the emission and retrieval of single photons are within reach.

Preparation and quasi-permanent storage of single atoms is achieved using different strategies of laser cooling and trapping. Naturally, individually trapped neutral atoms present well-defined single quantum systems and are prime candidates for quantum information science [70, 71, 72, 73, 74, 75]. Embedding the atoms in an optical resonator boosts these capabilities by enhancing control and connectivity.

The content of this thesis is organized as follows.

Chapter (2) introduces the essential features of the new single atom-cavity setup. The chapter briefly describes the apparatus, the methods with which cold atoms are prepared inside the cavity, and the detection tools for atoms and photons. The overall performance

of the new setup is characterized using the example of a single photon server based on one atom. This example demonstrates that a quantum protocol can be efficiently run on a single atom which is quasi-permanently trapped in the cavity.

In chapter (3), we study the excitation of the atom-cavity system by short laser pulses. We observe vacuum Rabi oscillations between an atom and a single photon in the cavity field. The dynamics of the coupled system and the suitability of short pulse excitation for photon generation are analyzed in detail. We use the fast excitation scheme to generate single photons at a high repetition rate and with a tunable wave packet shape. The experimental results are in excellent agreement with theory and illustrate a textbook-type example of CQED in the optical domain.

In chapter (4), we investigate schemes for internal state detection of single neutral atoms by means of a cavity. A theoretical analysis of atomic hyperfine state detection identifies problems associated with state readout of neutral atoms and indicates how they can be solved in a CQED setting. We introduce a readout technique based on cavity-enhanced fluorescence which enables the efficient detection of the atomic hyperfine state. Most important, this technique does not cause the loss of the atom upon readout and establishes single atoms as truly stationary carriers of quantum information. The experiments on cavity-enhanced fluorescence are complemented by an investigation of atomic state detection using differential cavity transmission. The two methods are compared and specific advantages are discussed.

Chapter (5) briefly describes an experiment on electromagnetically induced transparency (EIT) with a single atom. We observe the interaction of two weak light beams mediated by a single atom. This proof-of-principle experiment opens perspectives for the controlled generation, retrieval and storage of photons in single atom-cavity systems.

Chapter (6) reports on a study of phase-controlled single-photon wave packets. By imprinting phase patterns on propagating photon wave packets we are able to control two-photon interference. A time-resolved analysis of the experiment leads to a generalized description of two-photon interference in which the usual Hong-Ou-Mandel effect can be modified and even reversed.

2 Experimental Setup

2.1 A new single atom-cavity setup

A major goal of this thesis work was the construction of a new CQED experiment in which a single Rb atom is permanently coupled to a high-finesse optical resonator. The new apparatus conceptually follows a prototype by S. Nußmann and co-workers [76, 77, 78]. Improvements in the new setup described here aim at simplification, increased reliability and extended functionality. To this end, improved optical access, additional degrees of control, new software and new detection schemes have been implemented. After three years of construction, the new experiment became operational in 2008.

The parameter ranges of this experiment span many orders of magnitude - from macroscopic dimensions to the quantum regime (Fig. 2.1). Atoms at temperatures of only a few μK coexist with materials at temperatures of many hundred Kelvin in the vicinity of a few mm. The strength of optical fields ranges from 10 W continuous laser power for the optical dipole traps to the level of single photons generated in the cavity output. The time scales of the experiment span from atom trapping times on the order of many seconds to monitoring the cavity output with nanosecond resolution.

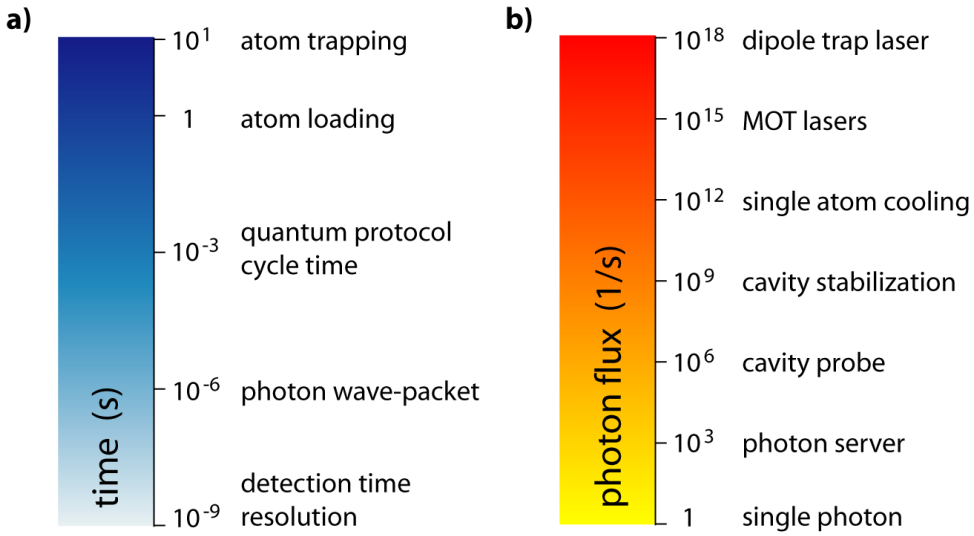

Figure 2.1: Time and energy scales of the experiment. a) The macroscopic time scale of the experiment is given by the trapping time of single atoms in the cavity of up to 60 s. The shortest time scale is given by the time resolution of single-photon detection (1 ns). Typical cycle times of the measurement protocol are on the order of 1 ms. **b)** The flux of photons along different axes of the experiment spans 18 orders of magnitude. The dipole trap laser beam traversing the cavity has a power of a few Watts, while simultaneously we observe single photons in the cavity output.

At the heart of the experimental setup is a high-finesse optical cavity (Sec. 2.3). The cavity operates in an intermediate regime of atom-cavity coupling with $(g;\kappa;\gamma)/2\pi = (3;3;3)$ MHz where g denotes the coherent atom-cavity coupling rate, and (κ,γ) denote the decay rates of cavity field and atomic polarization, respectively. Quasi-permanent storage of a single ^{87}Rb atom inside this resonator is achieved by a combination of different techniques for laser cooling and trapping of neutral atoms [79].

The basic operating principle of the apparatus follows a three-step process (Fig. 2.2). First, a magneto-optical trap (MOT) provides a reservoir of cold ^{87}Rb atoms. Second, the atoms are loaded into a running wave dipole trap and are probabilistically transferred into the cavity mode. Inside the cavity, single atoms are localized in a standing wave optical dipole trap and are cooled by transversally applied laser beams. The number and location of atoms trapped inside the cavity is determined with a high numerical aperture CCD-camera system. As a third step, a repetitive measurement protocol is applied with one atom permanently trapped inside the cavity mode. Information about the quantum state of the atom-cavity system is obtained by monitoring the cavity output at the single photon level.

The details of this setup and a first benchmark measurement in which the new apparatus is operated as a single photon server (Sec. 2.6) are presented in the following sections.

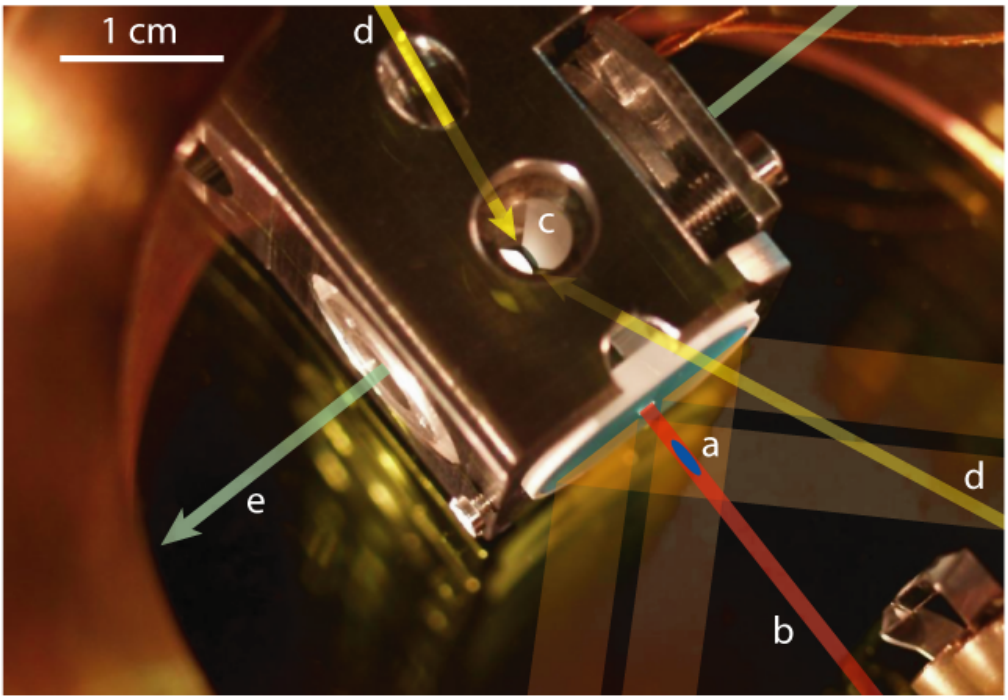

Figure 2.2: Experimental setup. A reservoir of cold ^{87}Rb atoms (a) is prepared in a magneto-optical trap. An optical dipole trap (b) guides a few atoms into the high-finesse cavity (c). There, a single atom is quasi-permanently trapped and a repetitive measurement protocol is applied using near resonant laser beams (d). The cavity output mode (e) is coupled to a detection setup and monitored at the single photon level.

2.2 Vacuum system and lasers

The vacuum system used for the experiment is similar to the design described in [76] and a technical drawing can be found in the appendix (8.3). It consists of an octagon-shaped steel chamber (415LN, non-magnetic) which is designed for maximum optical access. While eight of its ten ports are used as optical windows (optical quality fused silica, AR coating 750-1100 nm), two ports are occupied by electrical feedthroughs and the connection to a pump system (Titan sublimation pump, Ion-getter pump). The system operates in the 10^{-10} mbar regime at room temperature. The background gas pressure would limit the lifetime of a trapped Rb atom to between 30 s and 1 min (estimated). A major difference to the original design by S. Nußmann is the mounting of the cavity holder. In the new system, the holder can be retracted from the vacuum system by only opening two of the small side flanges ("rear window" and electrical feedthroughs). This means that the cavity can be exchanged more easily for repair or mirror replacement. So far, neither mechanical instability nor additional vibration noise have been observed for the altered cavity-holder design.

In the new experiment, the atom-cavity setup is separated from the remaining infrastructure: One separate optical table carries the vacuum chamber with cavity and essential optics. A second optical table carries all lasers, optics and electronics. The two tables are only coupled by optical fibers which deliver all necessary light beams to the experiment. Thereby, the experiment is mechanically (vibrations) and electronically (grounding of voltages, shielding from radio-frequency cross-talk) decoupled from the laser table. Additionally, the optical fibers precisely define spatial modes. In combination with short optical path lengths at the experiment, this ensures stable adjustment of the laser beams directed onto the single atom-cavity system. A layout sketch of the experimental table is presented in the appendix (8.4).

As light sources we use 3 diode lasers (Toptica models DL100 and DLX110) operating at wavelengths of 780 nm and 785 nm and one high-power fiber laser at 1064 nm (IPG YLM-1064-10). The laser light at 780 nm is frequency-shifted and intensity-controlled by several acousto-optic modulators (AOM's) to address each transition of the Rb D2-line. The two diode lasers at 780 nm are locked to Rb vapour cells with the Pound-Drever-Hall technique (linewidth 100-500 kHz). The light at 785 nm is used as a reference to stabilize the cavity length. This diode laser is locked to a frequency comb reference using a beat-lock scheme (linewidth <100 kHz). The high-power fiber laser is not frequency stabilized and delivers a single mode (spatial and frequency) beam at a cw-power of up to 10 W which is split and independently controlled by two electro-optic modulators (Linos EOM LM0202 high power, 3 mm aperture, control voltage 0-600 V provided by TREK PZD700). This light is used to create two far-detuned optical dipole traps.

In our laboratory, we have introduced a frequency comb laser system as an absolute frequency standard. The frequency comb was manufactured by MenloSystems and was installed in 2009. At its core is a pulsed fiber laser with a repetition rate $f_{rep} = 250$ MHz. As a 10 MHz reference signal for the beat note stabilization (repetition rate, carrier-envelope offset) we use a stable hydrogen maser signal supplied by the group of Prof. Hänsch. Ad-

ditionally installed modules amplify and frequency-double the optical output spectrum for use in the spectral ranges 775 to 795 nm and 1000 to 2000 nm. The comb delivers approx. 100 mW of optical power in the spectral range 760 to 800 nm. This output is coupled into an optical fiber network which supplies the laboratories of our group. Typically 10 mW of optical power are delivered to each laboratory. More information on the frequency comb system can be found in the appendix (8.5).

2.3 Cavity

At the heart of the experimental setup is a high-finesse optical cavity. The cavity parameters have been chosen to achieve an intermediate regime of atom-cavity coupling and a highly directional optical output.

The cavity consists of two fused silica conic substrates with high-reflectivity dielectric coatings on their top faces (coating: REO, Boulder, USA). The total round trip losses of the cavity (113 ppm) are dominated by the transmission of one of the mirrors (101 ppm). Therefore, photons present inside the cavity are mapped to the well-defined output mode through this outcoupling mirror with 89 % probability. The mirror distance of d=495 μm is chosen small enough for a sufficient atom-cavity coupling g, but large enough to accomodate traversing laser beams (diameters approx. 200 μm). The measured cavity parameters for light at wavelength 780 nm are summarized in the following table. The measured cavity linewidths at 785 nm and 795 nm agree with the value at 780 nm and we therefore assume all other parameters are identical as well.

mirror transmission	$T_1 = (2 \pm 0.5)$ ppm, $T_2 = (101 \pm 2)$ ppm
mirror distance	$d = (495 \pm 2)\,\mu$m
mirror curvature	$r = 50$ mm
mode waist	$w = 29.6\,\mu m$ ($1/e^2$ intensity radius)
mode Rayleigh length	$z_R = 3.5$ mm
dissipative loss	$L = (10 \pm 1)$ ppm
total round-trip loss	$L = (113 \pm 2)$ ppm
cavity finesse	$\mathcal{F} = 56\,000$ (TEM_{00})
free spectral range	$FSR = 303$ GHz
cavity decay rate	$\kappa/2\pi = (2.8 \pm 0.1)$ MHz
cavity decay time	$\tau = 26$ ns (1/e intensity decay)
power enhancement	$\eta = 630$ (circulating/impinging power)
maximum transmission	$T_{cav} = 6\,\%$
output directionality	$\eta_{out} = 89\,\%$

Mechanically, the cavity mirrors are mounted into the cavity holder in a stack of mirror holders, ceramic spacers and a piezo-electric element ("piezo"). The mirror holders clamp the mirror substrates with even pressure around the circumference to avoid unidirectional mechanical stress and concomitant optical birefringence. The cavity has been tested after

bake-out in the vacuum system and no birefringence was found. The piezo is of cylindrical shape and has 8 drilled holes of diameters between 1.5 mm and 7 mm which allow for optical access perpendicular to the cavity mode. The inner and outer surface of the piezo are metal-coated and constitute the electrical contacts.

Precise tuning of the cavity frequency is achieved by applying control voltages of 0-150 V with sub-mV precision to the piezo. The control voltages are derived from an active feedback loop which stabilizes the cavity frequency to better than ± 0.5 MHz, corresponding to an uncertainty in the absolute cavity length of approx. 1 pm. The cavity stabilization is based on the Pound-Drever-Hall technique. A phase-modulated laser beam at wavelength 785 nm (modulation frequency 20 MHz) serves as a reference and is detected in transmission. This was found to improve the signal-to-noise ratio compared to a lock based on the signal reflected by the cavity. The reference light is allowed to have arbitrary polarization and is separated from light at 780 nm after the cavity by a dichroic mirror.

The coherent atom-cavity coupling rate g is determined by the atomic transition strength (dipole matrix element μ_{ge}) and the cavity mode volume V. It is further spatially modulated by the standing wave structure of cavity field $\psi_c(\mathbf{r})$.

$$g(\mathbf{r}) = \psi_c(\mathbf{r}) \sqrt{\frac{\omega_c}{2\epsilon_0 V \hbar}} \cdot \mu_{ge} \tag{2.1}$$

The effective atom-cavity coupling depends on the atomic position via $\psi_c(\mathbf{r})$ and on the internal atomic state and the polarization of the cavity field mode via μ_{ge}. Thus, certain averaging strategies must be applied to account for atomic motion or undefined light polarization (appendix 8.1). For the strongest dipole transition $|F = 2, m_F = 2\rangle \leftrightarrow |F' = 3, m'_F = 3\rangle$ and an atom localized at a cavity field maximum, the coupling is as large as $g_{max}/2\pi = 7.9$ MHz. Combined spatial and polarization averaging reduce the effective coupling to $g \approx 3$ MHz on the transition $F = 2 \leftrightarrow F' = 3$. Indeed, we have observed in several experiments that the measured effective g is typically 40 % of the theoretical maximum of g for a given atomic transition (see appendix 8.1 for details).

2.4 Trapping and transporting atoms

The single Rb atoms which are eventually transported to and stored in the cavity are taken from a larger ensemble of cold atoms provided by a magneto-optical trap (MOT). A MOT combines radiation pressure and position-dependent atomic Zeeman shifts to achieve phase space reduction of atomic motion in the momentum and spatial domain [79]. For the described experimental setup, a new geometry has been invented which further simplifies existing mirror-MOT schemes. The new scheme reduces the number of laser beams, the necessary optical power and the number of optical elements (see appendix). This MOT typically operates with a total optical power of 2 mW for the cooling laser while the number of atoms in the MOT is efficiently controlled by varying the power of the repump laser between 0 and 100 μW. As a source of Rb atoms we use an ohmically heated dispenser ca. 1 cm away from the location of the MOT. The steady state temperature of atoms in

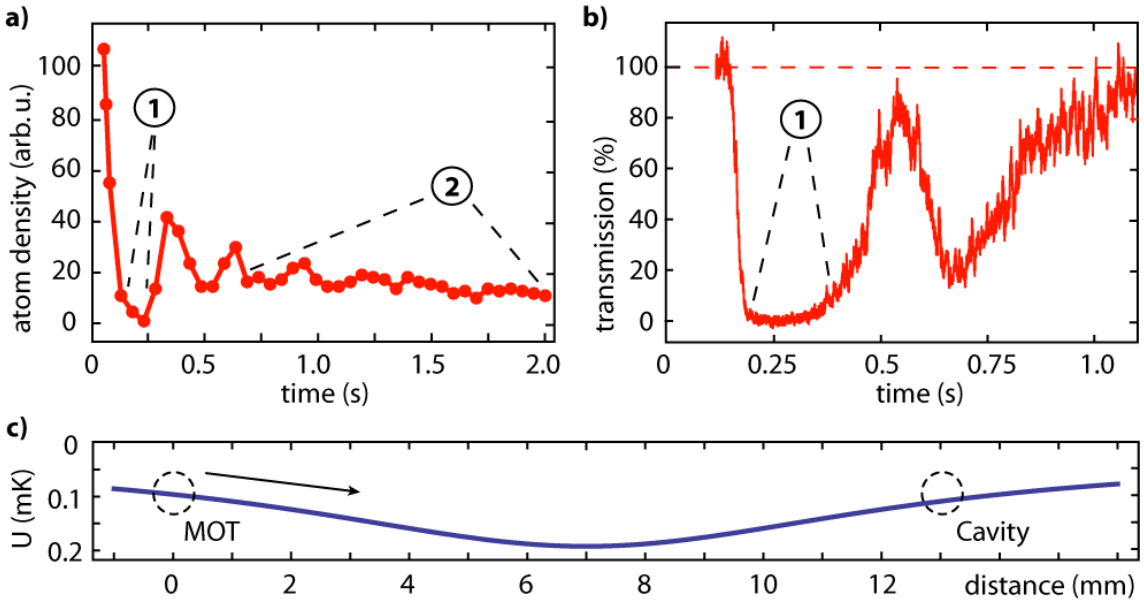

Figure 2.3: Transport of atoms and cavity loading regimes. **a)** Atom density in the transport dipole trap at the location of the MOT (red data points) is deduced from absorption images taken with a certain time delay after atoms have been released from the MOT into the dipole trap. The atoms perform oscillations (period $T \approx 0.3\,\mathrm{s}$) in the transport trap potential. After two oscillations the atomic density distribution is nearly constant due to the anharmonicity of the trap potential. This establishes two regimes for atom transport into the cavity: 1) Atoms perform half an oscillation and are immediately stored in the cavity. 2) The cavity is supplied with a constant flux of atoms. **b)** Atom density in the cavity mode as measured by cavity transmission. The transmission of cavity probe light (red solid line) is reduced due to the arrival of atoms in the cavity. The empty cavity transmission (red dashed line) is given as a reference. Maxima of atomic density at the cavity mode correspond to minima of the atomic density at the position of the MOT. **c)** Calculated transport trap potential with a minimum at the focus of the trap laser beam between MOT and cavity region.

the MOT is $\leq 100\,\mu\mathrm{K}$. The typical atom number in the MOT is chosen to be only a few thousand Rb atoms.

Two optical dipole traps provide conservative potentials in which Rb atoms are transported and trapped. Optical dipole traps are based on the AC Stark effect arising in intense light fields. We use a single-mode fiber laser delivering up to 10 W cw-power at a wavelength of 1064 nm. The light is far red-detuned from the Rubidium D1 and D2 lines (795 and 780 nm) and thus generates optical potentials in which Rb atoms are attracted to regions of highest intensity [80]. The resonant excitation rates due to trap light are negligible.

Atoms are transported from the MOT to the location of the cavity by a shallow running wave dipole trap ("transport trap"). The transfer efficiency from the MOT into this trap is typically 50 %, limited by atom temperature and by spatial overlap. The focus of the transport trap lies in between MOT position and cavity. Atoms released from the MOT are accelerated towards this focus and reach the turning point of motion approximately at the cavity location (13 mm distance from the MOT). At this point, the atoms are

tranferred into a second dipole trap ("storage trap") which has a tight focus at the cavity location. It is retro-reflected by a piezo-tiltable mirror creating a periodic standing wave potential. The properties of transport and storage trap are summarized in the following table (calculations based on [80]).

	transport trap	storage trap
Focus size ($1/e^2$ radius)	$45\,\mu$m	$16\,\mu$m
Rayleigh length	6 mm	0.7 mm
Trap depth at focus	$48\,\mu$K/W	1.5 mK/W
D2-line Stark shift	1.6 MHz/W	52 MHz/W
Typical input power	4 W	2.5 W

The motion of atoms in the anharmonic potential of the transport trap has been numerically and experimentally studied. We identify two regimes for loading atoms into the cavity (Fig. 2.3). In the first and most often used regime, the atoms are released from the MOT, drift to the cavity region, and are immediately localized in the storage trap. In the second regime, the storage trap is not used and the atoms perform oscillations in the transport trap (Fig. 2.3). However, the anharmonicity of the trap potential leads to dispersion. After a few hundred milliseconds, a stable density distribution of atoms is established across the whole transport trap. In this regime, the cavity is supplied with a constant flux of slow atoms. Despite its probabilistic nature, operation in this regime has several advantages. As the maximum AC-Stark shifts are small ($\Delta_s \leq 6$ MHz), the atomic level structure is only minimally disturbed. Also, when permanent trapping of atoms is abandoned, arbitrarily high magnetic fields and arbitrary cavity and laser frequencies can be used. Further, the slow overall atom loss in this regime can be compensated by intermittent use of the MOT while the transport trap remains permanently present.

In addition to the dipole traps at 1064 nm, the cavity reference light at 785 nm provides a standing-wave potential which is oriented along the cavity axis. The trap depth for Rb ground state atoms is approximately $3\,\mu$K per $1\,\mu$W of linearly polarized light impinging on the cavity. This value holds for perfect mode-overlap (spatial and frequency) of the cavity input coupling. The value includes power-built up inside the cavity (4x630 at a field antinode) and the combined ground state level shifts due to coupling to the Rb D2 transition (780 nm, red-detuned) and D1 transition (795 nm, blue-detuned). In practice, the spatial input mode-matching is on the order of 50 %. For typical stabilization light powers of $20\,\mu$W, we find an intracavity dipole trap depth of $30\,\mu$K. The exact frequency of the cavity reference light is chosen to be an even number (N=8) of free spectral ranges detuned from the cavity mode at 780 nm. As a consequence, the cavity field at 780 nm and the dipole potential at 785 nm wavelength exhibit a spatial beat pattern with a periodicity of $50\,\mu$m. The anti-nodes of the two fields overlap at the geometric center of the cavity (see appendix for an image). Atoms trapped in the 785 nm trap in these anti-nodes should therefore optimally couple to the resonant cavity mode at 780 nm. However, an enhancement of the atom-cavity coupling due to atomic confinement in this intracavity trap has not been convincingly demonstrated in our experiment.

2.5 Single atom imaging and single photon detection

A CCD-camera system with a high numerical aperture objective images the fluorescence of atoms during optical cooling inside the cavity. The objective has a numerical aperture of NA = 0.4 and a spatial resolution of 1.3 μm in the object plane. With a total magnification of $M = 29$, one pixel in the image plane (CCD-camera chip, actual pixel size 16×16 μm) corresponds to 0.55 μm in the object plane (all values confirmed by calibration measurements). The objective is homebuilt and follows the design described in [81], but it deviates in the use of the final focussing lens (see appendix) and the mechanical mounting. The objective is mechanically disconnected from the camera and the vacuum system. It can be independently translated along all three spatial axes with μm-precision. The mechanics of mounting is reduced to a minimum in weight and size while the overall stability remains excellent. The CCD-camera chip (AndorIXON DU897) is Peltier-cooled to 170 K and optimized for high quantum efficiency (specified 90 %, back-illuminated design). Low intrinsic noise and near-perfect stray light shielding enable high-contrast fluorescence imaging of single trapped atoms within 100 ms exposure time. The typical exposure time during a measurement protocol with intermittent cooling is 400 ms. Single-shot raw images are evaluated in real-time to determine the number and location of atoms loaded in the cavity TEM_{00} mode profile. Based on this evaluation, a software trigger can either start a new loading attempt or the repetitive measurement protocol. However, we can not resolve single anti-nodes of the dipole trap potential or the cavity mode. In future experiments, advanced algorithms for image evaluation may be used to achieve single site resolution beyond the standard resolution limit of the objective [82]. A detailed technical sketch of the single atom imaging system is given in the appendix (8.2). A sample fluorescence image of a single atom is shown in figure (2.4a).

Alternatively, the atom-cavity system can be probed via the cavity output at the level of single photons and with high temporal resolution. A single photon present inside the cavity is emitted through the outcoupling mirror with a probability of 89 % (Sec. 2.3) and is detected with a total efficiency above 30 %. After the cavity output mirror and just outside the vacuum system, the cavity output mode is collimated and after free propagation for less than 1 m it is coupled into a single-mode optical fiber with up to 90 % efficiency. Along the free propagation path, the stabilization light at 785 nm is separated from light at 780 nm with three filters (Semrock Laserline, specified transmission at 780 nm: 99.9 %, at 785 nm: 10^{-5}). With these filters, the measured total transmission of 785 nm light is less than 10^{-11}, the total transmission at 780 nm is better than 95 %. Finally, the optical fiber delivers light at 780 nm to a single photon counting module (SPCM, Perkin Elmer AQR-16 avalanche photodiodes). The SPCM has an intrinsic electronic dark count rate of 25 Hz. The total "dark count rate" of the detector is typically 50 Hz including an additional 25 Hz stray light count rate. This background signal is extremely low and requires light-tight housing of the detection path from the fiber input coupler to the detector – even the optical fiber itself must be covered. The quantum efficiency of the AQR-16 model is 50 % (measured) in accordance with the technical specifications (50 to 60 %). The total scattering and absorption losses along the whole detection path (10 optical elements) amount to approximately 10 %. Taken together, the measured total detection efficiency

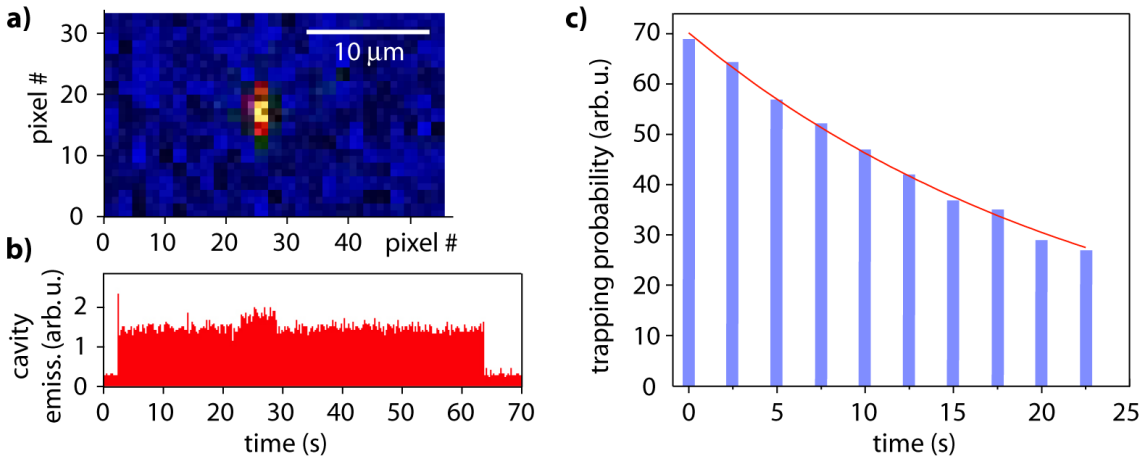

Figure 2.4: Observation and storage of single atoms. a) Typical CCD-camera image of a single trapped atom (exposure time 400 ms, raw data). The size of the fluorescence spot of the atom (2×6 pixels) is due to the resolution of the objective (2 pixels correspond to 1.1 μm) and finite atomic temperature. Along the dipole trap axis, the atom is confined to less than half a wavelength of light ($<$ 500 nm, horizontal axis in the image). Along the radial direction of the standing wave trap, the spatial confinement is weaker and the finite atomic temperature results in a atomic position spread within an anti-node of the dipole trap (6 pixels correspond to 3.3 μm and temperatures below 100 μK, vertical axis in the image). **b)** The coupling of the atom to the cavity mode is signalled by emission of cooling light into the cavity output. Shown is a single atom trace with a trapping time of 65 s. **c)** The probability distribution of observed atom trapping times (permanent optical cooling) is well described by an exponential decay with time constant $\tau = 24 \pm 0.5$ s.

is 34 ± 3 %. This number refers to the probability to obtain a detector click for a single photon present inside the cavity. The electronic output pulses of the SPCM are recorded by a counter card (FastComTec P7888) with a time-resolution of 2 ns in four separate channels (1 ns resolution when only two channels are used). For Hanbury Brown-Twiss and for two-photon interference measurements, the single mode fiber in the detection path is replaced by one or more single mode fiber beam splitters coupled to up to four SPCM's. The fiber beam splitters exhibit near perfect mode overlap and power splitting ratio. The observed visibility of interference fringes is better than 99 % for coherent probe light.

2.6 Performance of the new atom-cavity system

The apparatus described in this thesis became operational in 2008 and has worked reliably since. In this section, the standard performance of the system is briefly characterized using the example of a single photon server [83].

A first important result of the new setup is the observation of efficient trapping and cooling of single atoms outside the previously studied cavity-cooling regime [78]. The new regime explored here is characterized by frequencies of the cooling laser which are red-detuned by $\Delta = 1 \ldots 10\,\gamma$ with respect to the unperturbed atomic $5^2S_{1/2}$ $F = 2$ to $5^2P_{3/2}$ $F = 3'$

transition. Atomic cooling is observed to work well for all cavity frequencies which are at least one γ blue-detuned of the cooling laser. This suggests that the dominant cooling mechanism is independent of the cavity, i.e. Doppler and Sisyphus-like cooling [84]. As a consequence, we obtain the cavity frequency as a quasi-free experimental parameter. As a standard parameter set, the cooling beam (45° axis, retro-reflected, lin$\perp$lin, power 2 μW) is set to a frequency 10 MHz red-detuned of the unperturbed $F = 2$ to $F' = 3$ transition. Along the same beam axis, we apply a repump laser (power 0.5 μW) resonant with the unperturbed atomic $F = 1$ to $F' = 2$ transition. The dipole traps operate at powers of 4 W (transport trap) and 2.5 W (storage trap, measured Stark shift 100 to 120 MHz). The presence of atoms in the cavity is monitored with the CCD-camera and by emission of cooling light into the cavity output mode. A typical cavity emission trace is shown in figure (2.4). An evaluation of the trapping times of individual atoms yields a 1/e lifetime of 24 s for continuous optical cooling.

A complete atom loading cycle, including MOT (0.2 s), transport (0.2 s) and real-time evaluation (0.7 s) of atom location in the cavity takes about 1 s. The ratio between useful measurement time and total experimental run time is termed duty cycle of the experiment. For long trapping times ($\geq$ 5 s), the duty cycle is governed mainly by the repetitive measurement protocol itself. However, taking into account failed attempts of probabilistic atom loading reduces the duty cycle which can partly be compensated by quick reloading after failure.

From the camera images we can not only count atoms, but also estimate their temperature. In our setup, a trapped single atom typically creates a fluorescence spot of 2×6 pixels. The small extension along the axis of strong atomic confinement in the standing wave trap is dominated by the resolution of the objective. The fluorescence spot extension along the long axis stems from the spread of atomic position transverse to the dipole trap axis. Compared with a single well of the optical dipole potential, this is consistent with an average atomic temperature of $T \leq 100\mu$K.

As an example, we have implemented a protocol for the generation of single photons with a vacuum STIRAP process [85, 83]. A beautiful second-order correlation function recorded with only one atom is shown in figure (2.5). In these first trials, the photon production efficiency was 20 % for a photon wave packet duration of 300 ns. By the time of writing this thesis, photon production efficiencies of up to 60 % have been measured at photon durations of 2 μs.

Measuring a photon correlation function with only one atom (Fig. 2.5) nicely summarizes the capabilities of the new setup: A single atom is quasi-permanently stored in the cavity, its presence and location are verified in real-time. We can further run a repetitive quantum protocol on this atom and efficiently measure the cavity output at the single photon level.

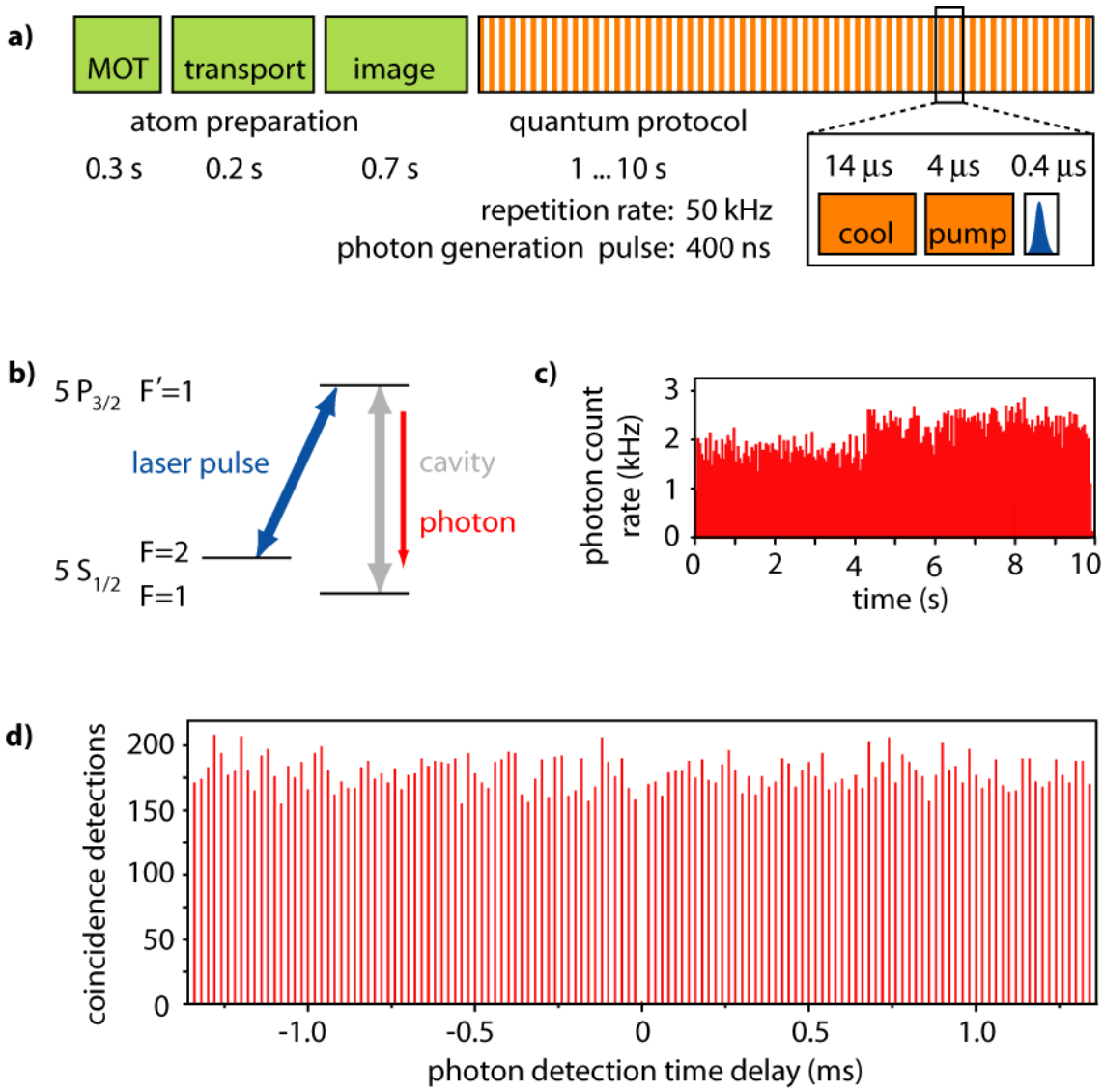

Figure 2.5: Performance of the new CQED apparatus. a) Overview of an experimental sequence consisting of preparation of a cold ensemble of Rb atoms in the MOT, transport of atoms to the cavity region, fluorescence image analysis of the number and location of atoms in the cavity mode. If exactly one atom is present in the cavity, the actual quantum protocol is applied with high repetition rate. **b)** In the quantum protocol applied here, single photons are generated in a Raman process with a single atom coupled to the cavity. The Λ-level scheme is comprised of a driving laser field connecting the atomic hyperfine states F=2 and F'=1 and of the cavity mode resonant with the atomic F=1 to F'=1 transition. **c)** The emitted stream of photons is detected in the cavity ouput mode. Shown is a 10 s emission trace of a single atom causing a single photon count rate of more than 2 kHz at the detectors. **d)** The emission trace given in c) has been evaluated for detection event correlations in a Hanbury Brown-Twiss setup and photon antibunching is observed. The high total number of correlations obtained within 10 s demonstrates the efficient generation and detection of photons using just one atom.

3 Short pulse excitation of a single atom-cavity system

In this chapter, we investigate the excitation of a single atom coupled to an optical cavity by means of short laser pulses. The observed dynamics present a fundamental example of cavity quantum electrodynamics in the optical domain. The emitted single photons exhibit distinct wave packet shapes and are in a superposition of two tunable frequencies. We investigate possible control parameters and the efficiency of this photon generation process.

After a brief introduction of pulsed atomic excitation in free space (section 3.1), we theoretically describe the dynamics of the coupled atom-cavity system (section 3.2) and analyze the photon emission process (section 3.3). We then present the experimental results (section 3.4), followed by a discussion (section 3.5).

The content of this chapter has partially been published in:
"Fast Excitation and Photon Emission of a Single-Atom-Cavity System",
J. Bochmann, M. Mücke, G. Langfahl-Klabes, C. Erbel, B. Weber, H. P. Specht, D. L. Moehring, and G. Rempe, *Physical Review Letters* **101**, 223601 (2008).

3.1 Single photons from an atom in free space

We introduce the basic nomenclature by considering the case of a single two-level atom in free space excited by a near resonant continuous wave laser beam. The light emitted by the atom exhibits photon-antibunching which is characterized by an intensity correlation function $g^{(2)}(\tau = 0) = 0$. Under the influence of the driving laser field the atomic population performs coherent Rabi oscillations between the ground state $|g\rangle$ and the excited state $|e\rangle$ at a Rabi frequency Ω_R. The coherent oscillation is randomly interrupted by spontaneous decay from $|e\rangle$ to $|g\rangle$ accompanied by the emission of a single photon. The probability of spontaneous emission events is proportional to the excited state decay rate $\Gamma = 2\gamma$. When averaging over many emission events one obtains a characteristic $g^{(2)}(\tau)$ function (Fig. 3.1). We find antibunching at $\tau = 0$ because detection of a photon at $\tau = 0$ projects the atom into $|g\rangle$. Thus the probability of a second photon emission at $\tau = 0$ vanishes. In the transient regime ($0 < \tau < 5/\Gamma$), oscillations at the Rabi frequency Ω_R appear and fade to uncorrelated emission for $\tau \gg \Gamma$. We conclude that in the case of continuous excitation, antibunching only occurs on time scales much shorter than the inverse Rabi frequency.

For a useful single photon source, however, one requires to find no more than one photon in any given macroscopic time interval of length T such that $g^{(2)}(0 \leq \tau \leq T) = 0$. The interval $[0, T]$ constitutes a single photon pulse if it contains exactly one excitation of the

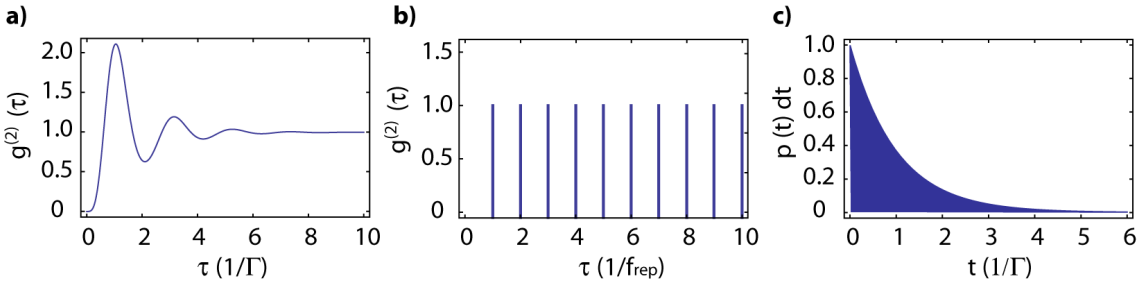

Figure 3.1: Photon emission of a single atom in free space. a) The atom is continuously driven by a coherent field. Rabi oscillations of the atomic population lead to modulations of intensity correlation function $g^{(2)}(\tau)$ of the emitted light. **b)** The atom is excited by short laser pulses. The expected intensity correlation function $g^{(2)}(\tau)$ shows discrete peaks at a distance given by the pulse repetition rate f_{rep}. c) Wave packet shape (exponential decay) of single photons emitted after short pulse excitation.

electromagnetic field. Such single photon pulses can be generated by exciting a single atom with a laser pulse of duration τ_p much shorter than the spontaneous decay time $1/\Gamma$. After the excitation, the atom is subject to spontaneous decay. It will emit a single photon with a temporal probability distribution $\rho_{phot}(t) = \Gamma e^{-\Gamma t}$ which is equivalent to the wave packet shape of the photon (Fig. 3.1). For example, upon excitation of the atom at $t = 0$ a photon is emitted in the time interval $t = [0; 5/\Gamma]$ with 99.3% probability and no photon emission occurs with a probability of 0.7%. For the Rb D2-transition ($\Gamma = 2\pi\, 6\,\mathrm{MHz}$, $1/\Gamma = 26.2\,\mathrm{ns}$) this yields $T = 131\,\mathrm{ns}$ and a maximum repetition rate of the excitation pulses $f_{rep} = 7.6\,\mathrm{MHz}$.

The probability $p_m(\tau_p)$ to generate more than one photon from one excitation pulse of duration τ_p is bounded by the probability of spontaneous atomic decay during the excitation pulse. This would allow a second sequential excitation of the atom and a second photon emission event. For infinite excitation pulse power the bound p_m is given by:

$$p_m(\tau_p) \leq 1 - e^{-\Gamma\,\tau_p}. \tag{3.1}$$

Any higher order multiple photon emission events are included in this bound. For the ^{87}Rb D2-line and a pulse duration of $\tau_p = 1\,\mathrm{ns}$ we obtain $p_m = 3.7\,\%$.

All in all, the generation of single photons by short pulse excitation in free space has proven as a versatile method in a multitude of physical systems such as neutral atoms, ions, quantum dots, NV-centers in diamond and molecules [86, 87, 88, 89, 90]. Exploiting the multi-level structure of atoms, short pulse excitation can be extended to generate entanglement between the internal atomic state and the emitted photon [86]. The scheme offers high repetition rates and its conceptual simplicity facilitates implementation.

A severe drawback of short pulse excitation in free space is its low photon collection efficiency. The photon generation process is mediated by spontaneous emission which occurs in random directions. Only a small fraction of all emitted photons can be coupled into a single spatial mode which may eventually be used for an experiment. Typical single photon retrieval efficiencies are on the order of 1 %. Further research towards the entanglement of

remote atoms and the demonstration of quantum repeaters in single-atom single-photon networks would benefit if the advantages of short pulse excitation could be combined with controlled emission schemes as provided by cavity quantum electrodynamics.

3.2 Dynamics of the atom-cavity system

In this section, we analyze the evolution of a coupled atom-cavity system after short pulse excitation. This provides the basis for the description of the photon emission process, which is the subject of section (3.3).

Similar to the excitation of an atom in free space, a short laser pulse can transfer an intracavity atom to the excited state $|e\rangle$. However, the state $|e, n = 0\rangle$, where n is the intracavity photon number, is not an eigenstate of the coupled atom-cavity system. In the following, we restrict ourselves to the case of exactly one excitation in the system. The evolution of the coupled atom-cavity system is determined by the Jaynes-Cummings Hamiltonian

$$H = H_a + H_c + H_{ac}. \tag{3.2}$$

Here, $H_a = \hbar\omega_{eg}\sigma^+\sigma$ is the Hamiltonian of a two-level atom with transition frequency ω_{eg} using the convention $\sigma^+ = |e\rangle\langle g|$ and $\sigma = |g\rangle\langle e|$. The energy of the cavity mode at frequency ω_c is given by $H_c = \hbar\omega_c(a^\dagger a)$ using the bosonic annihilation and creation operators a and $a^\dagger$. The atom-cavity coupling Hamiltonian $H_{ac} = \hbar g(a^\dagger\sigma + \sigma^+ a)$ scales with the atom-cavity coupling constant g. Here, we have implicitly assumed the rotating wave and dipole approximation. When allowing an atom-cavity detuning $\Delta_{\mathrm{ac}} = \omega_{eg} - \omega_c \ll (\omega_{eg}, \omega_c)$ we find for the eigenenergies of the coupled system:

$$E_\pm = \hbar\omega_c + \hbar\frac{\Delta_{\mathrm{ac}}}{2} \pm \frac{\hbar}{2}\sqrt{4g^2 + \Delta_{\mathrm{ac}}^2}. \tag{3.3}$$

These eigenvalues correspond to the first excited state doublet of the Jaynes-Cummings model with the eigenvectors (dressed states):

$$\begin{aligned} |+\rangle &= \cos\theta\,|e,0\rangle + \sin\theta\,|g,1\rangle \\ |-\rangle &= \sin\theta\,|e,0\rangle - \cos\theta\,|g,1\rangle\,. \end{aligned} \tag{3.4}$$

The mixing angle θ is defined as

$$\tan\theta = \frac{2g}{\Delta_{\mathrm{ac}} + \sqrt{4g^2 + \Delta_{\mathrm{ac}}^2}}. \tag{3.5}$$

It corresponds to a basis rotation in Hilbert-space $\{|e,0\rangle, |g,1\rangle\} \overset{\theta}{\Longleftrightarrow} \{|+\rangle, |-\rangle\}$ and quantifies the mixing of the bare states caused by the atom-cavity coupling.

We can express the time evolution of the system again in the uncoupled basis using equations (3.4). For the resonant case $\Delta_{\mathrm{ac}} = 0$ and starting in $|e,0\rangle$, this leads to a full-amplitude vacuum Rabi oscillation of the bare-state amplitudes at frequency g (while the vacuum Rabi frequency is defined as $\Omega_0 = 2g$):

$$|\Psi(t)\rangle = \cos(gt)\,|e,0\rangle - i\sin(gt)\,|g,1\rangle\,. \tag{3.6}$$

This evolution constitutes a coherent exchange of one energy quantum between the atom and the cavity field. These vacuum Rabi oscillations have been studied in some detail in microwave CQED experiments [91]. The phenomenon contains rich physics both from a basic CQED and a quantum information perspective [35]. For example, the dressed states exhibit entanglement between atom and field.

In any real experiment, the coherent evolution considered above is accompanied by dissipation. The two dissipation channels present in our system are atomic polarization decay quantified by a rate γ and damping of the intracavity field quantified by a rate κ. The spontaneous atomic decay rate γ is in good approximation unaffected by the presence of the cavity because the cavity mode covers only a negligible part of the solid angle.

The description of dissipation in open quantum systems requires considerable effort. One possibility is to derive a master equation which describes the time evolution of the system's density matrix under inclusion of the coupling to the environment. Detailed descriptions can be found in [76, 92, 93, 94, 95]. However, the correct solutions for the evolution of the atom-cavity system coincide with a phenomenological treatment of decay when the environmental bath is large and has negligible back-action on the system. Assuming time-independent coupling and decay constants, the time-evolution $c_i(t)$ of the bare state populations

$$|\psi(t)\rangle = c_e(t)\,|e,0\rangle + c_g(t)\,|g,1\rangle + c_0(t)\,|g,0\rangle \tag{3.7}$$

is given by a system of differential equations of the form:

$$\begin{aligned} \dot{c_e} &= igc_g - i\frac{\Delta_{\rm ac}}{2}c_e - \gamma c_e \\ \dot{c_g} &= igc_e + i\frac{\Delta_{\rm ac}}{2}c_g - \kappa c_g\ . \end{aligned} \tag{3.8}$$

An analysis of limiting cases gives insight into the physical processes at play. In the limit of strong atom-cavity coupling ($g \gg (\kappa, \gamma)$), the amplitudes $c_{e,g}$ oscillate at frequency $2g$ as expected from the dissipation-free Jaynes-Cummings model. However, in the bad cavity regime ($\kappa \gg (\gamma, g)$) the oscillations are strongly suppressed. In fact, for a resonant "bad" cavity ($\Delta_{\rm ac} = 0$), the atomic excited state population decays exponentially at a rate $2\gamma' = 2\gamma + 2g^2/\kappa$ which is a manifestation of the Purcell effect. Another limiting case is defined by large atom-cavity detuning $\Delta_{\rm ac} \gg (g, \kappa, \gamma)$ where the mixing angle θ is small. Here, the system evolves with a high-frequency low-amplitude oscillation close to the uncoupled states of atom and cavity.

The exact solutions of equations (3.8) for different parameter sets are given in figure (3.2). The different temporal evolutions illustrate the influence of $(g, \kappa, \gamma, \Delta_{\rm ac})$ on the dynamics of an atom-cavity system which is initialized in state $|e,0\rangle$ by a short pulse.

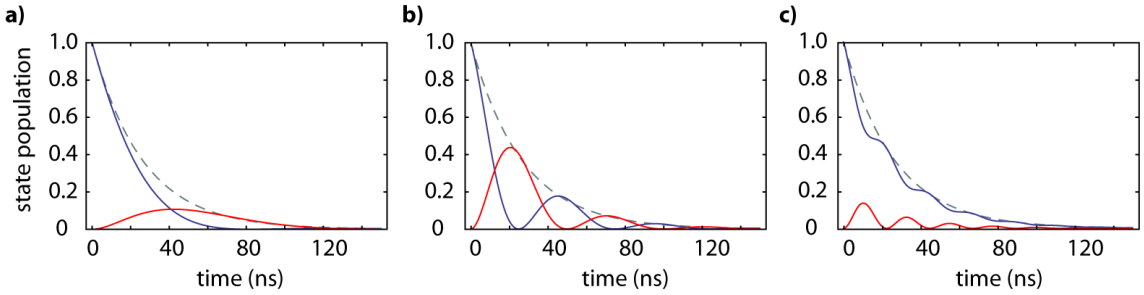

Figure 3.2: Time evolution of bare state populations for different parameter sets. The probabilities $|c_g(t)|^2$ (red solid line) and $|c_e(t)|^2$ (blue solid line) are shown for a system initialized in $c_e(0) = 1$ and $c_g(0) = 0$. The exponential decay of atomic excitation in free space is given as a reference (dashed line). **a)** Intermediate coupling regime, resonant case: The coherent oscillations are damped by cavity and atomic decay. Parameters: $(g, \kappa, \gamma, \Delta_{\mathrm{ac}})/2\pi$=(3.0, 2.8, 3.0, 0) MHz. **b)** Strong coupling regime, resonant case: Vacuum Rabi oscillations are well resolved and exhibit a conversion of atomic excitation into a cavity photon and vice versa. Parameters: $(g, \kappa, \gamma, \Delta_{\mathrm{ac}})/2\pi$=(10.0, 2.8, 3.0, 0) MHz. **c)** Strong coupling regime, detuned case: The atom-cavity detuning increases the generalized vacuum Rabi frequency and decreases the mixing angle of the bare states. Parameters: $(g, \kappa, \gamma, \Delta_{\mathrm{ac}})/2\pi$=(10.0, 2.8, 3.0, 40) MHz.

3.3 Single photons from a coupled atom-cavity system

The evolution of the atom-cavity system as described in the previous section governs the photon emission from the cavity. In this section, we first derive the properties of the emitted single photons and then investigate the efficiency of photon generation.

The excitation of the cavity mode is mapped to the cavity output via $|g,1\rangle \otimes |n=0\rangle_{out} \xrightarrow{\kappa} |g,0\rangle \otimes |n=1\rangle_{out}$. Therefore, the photon inherits its properties from the atom-cavity dynamics. The temporal wave packet shape of the single photon in the cavity output $|\Psi_{phot}(t)|^2$ is equivalent to the probability density to emit a photon at time t:

$$\int_t^{t+dt} \left|\Psi_{phot}(t')\right|^2 dt' = 2\kappa \left|c_g(t)\right|^2 dt. \tag{3.9}$$

Typical wave packet shapes of the emitted single photon are shown in figure (3.3). The modulations of the envelope reflect the evolution of $c_g(t)$. Alternatively, the emission process can be interpreted as a quantum beat of the two normal-modes of the atom-cavity system. The frequency components of the single photon correspond to the energies of the first excited doublet of the dressed states. The relative phase of the frequency components is set by the initialization in state $|e,0\rangle$.

In the remainder of this section, we analyze the efficiency with which single photons are created with the short pulse scheme. We define the photon generation efficiency p_{phot} as the probability to retrieve a single photon in the cavity output mode after the atom-cavity system has been initialized in $|e,0\rangle$. We calculate:

$$p_{phot} = \frac{2\kappa \int_0^\infty |c_g(t)|^2 \, dt}{2\kappa \int_0^\infty |c_g(t)|^2 \, dt + 2\gamma \int_0^\infty |c_e(t)|^2 \, dt}. \tag{3.10}$$

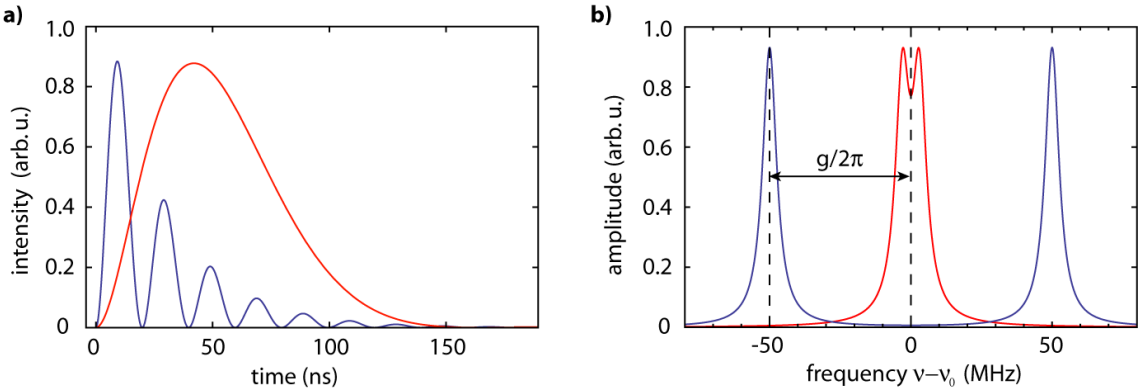

Figure 3.3: Photon shape and spectrum. **a)** Calculated wave packet shape of the emitted single photon for parameters $(g, \kappa, \gamma, \Delta_{\mathrm{ac}})/2\pi$=$(3, 3, 3, 0)$ MHz (red curve) and for $(g, \kappa, \gamma, \Delta_{\mathrm{ac}})/2\pi$=$(50, 3, 3, 0)$ MHz (blue curve). The amplitudes of the wave packets are independently normalized. **b)** Frequency spectrum of the photons of a). The two frequency components of each spectrum correspond to the dressed state energies of the coupled atom-cavity system. The normal-mode splitting is clearly visible for large g. The frequency axis is offset by the eigenfrequency of the uncoupled atom and cavity $\nu_0 = \nu_{\mathrm{c}} = \nu_{\mathrm{eg}}$.

This equation can be solved based on the known time evolution of c_e and c_g. In figure (3.4), the efficiency p_{phot} is plotted as a function of atom-cavity detuning Δ_{ac} and for different parameter sets $(g; \kappa; \gamma)$ close to our experiment. In general, we find that the efficiency is highest for small detunings Δ_{ac} and large coupling g.

In order to obtain analytic expressions for p_{phot}, we now consider limiting cases of equation (3.10). When the coherent oscillation between $|e, 0\rangle$ and $|g, 1\rangle$ is much faster than the incoherent decay, the average population of the bare states is determined by the mixing angle θ (Eq. 3.5) such that $\overline{|c_e(t)|^2} = 1 - 2\sin^2\theta\cos^2\theta$ and $\overline{|c_g(t)|^2} = 2\sin^2\theta\cos^2\theta$. Hence, the photon generation efficiciency simplifies to

$$p_{phot} = \frac{\kappa\ 2\sin^2\theta\cos^2\theta}{\kappa\ 2\sin^2\theta\cos^2\theta + \gamma\,(1 - 2\sin^2\theta\cos^2\theta)}. \tag{3.11}$$

It follows that

$$p_{phot} = \begin{cases} \frac{\kappa}{\kappa+\gamma} & \text{for } g \gg \Delta_{\mathrm{ac}} \\ \frac{\kappa}{\gamma}\frac{2g^2}{\Delta_{\mathrm{ac}}^2} & \text{for } g \ll \Delta_{\mathrm{ac}}. \end{cases} \tag{3.12}$$

For large g, the photon production efficiency is solely determined by the ratio of cavity and free space decay rate $p_{phot} = \kappa/(\kappa + \gamma)$. The obtained expression is an important benchmark. It presents a universal upper bound for the photon production efficiency with the short pulse scheme. For large detunings Δ_{ac}, the photon production efficiency decreases quadratically with atom-cavity detuning while cavity and free space decay are weighted by the ratio κ/γ.

We conclude that the efficiency of photon generation with the fast excitation scheme is generally not correctly described by a Purcell factor of the type g^2/κ. However, based on

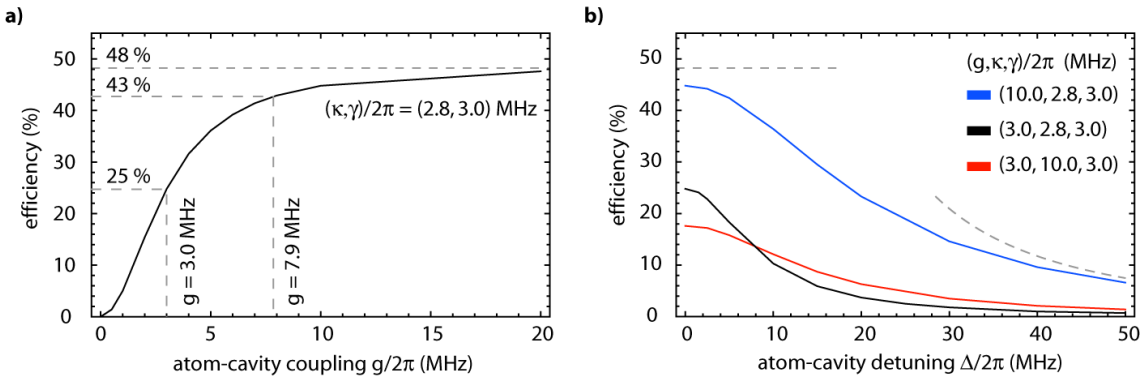

Figure 3.4: Photon generation efficiency. a) Calculated photon generation efficiency (solid line) as a function of atom-cavity coupling g on resonance ($\Delta = 0$). For large values of g, the efficiency approaches the value $\kappa/(\kappa + \gamma)$ (horizontal line). **b)** Calculated photon generation efficiency as a function of atom-cavity detuning Δ for different parameter sets (g, κ, γ). For large detunings, the efficiency scales as $1/\Delta^2$ as indicated by the dashed curve (calculated for $(g, \kappa, \gamma)/2\pi = (10, 2.8, 3.0)\,\mathrm{MHz}$). The dashed horizontal line marks the maximum achievable efficiency for $(\kappa, \gamma)/2\pi = (2.8, 3.0)\,\mathrm{MHz}$.

the evolution of $c_e(t)$ (Sec. 3.2) in the bad cavity limit on resonance ($\Delta_{\mathrm{ac}} = 0$) we find for the efficiency $p_{phot} = g^2/(\kappa\gamma)$.

In any real atom-cavity setup, the ideal value of p_{phot} must be corrected to a smaller effective photon generation efficiency p'_{phot}. First, one needs to account for the output directionality of the optical cavity. Only photons which leave the cavity through the designated outcoupling mirror will be useful for an experiment. Second, the short excitation pulse may not initialize the system in $|e, 0\rangle$ in every attempt such that on average $|c_e(t = 0)| < 1$. Introducing an average excitation probability p_{exc} and output directionality p_{dir}, the effective photon generation efficiency can be described as $p'_{phot} = p_{exc} \times p_{dir} \times p_{phot}$.

In our setup, the theoretical photon generation efficiency for an atom maximally coupled to the resonant cavity ($g/2\pi = 7.9\,\mathrm{MHz}$, $\Delta_{\mathrm{ac}} = 0$) is a remarkable $p_{phot} = 43\,\%$. However, we need to take into account a reduced coupling $g/2\pi = 3\,\mathrm{MHz}$ due to spatial and polarization averaging and an output directionality of $p_{dir} = 89\,\%$. Assuming an atomic excitation probability of $p_{exc} = 50\,\%$, we should expect an effective photon generation efficiency $p'_{phot} \approx 11\,\%$.

For conceptual reasons, the probability of producing two photons in the cavity mode from one excitation pulse is strongly reduced in a cavity QED setting as compared to the free-space case. The excitation initially deposited in the atom is only slowly transferred to the cavity field on the time scale of half a vacuum Rabi oscillation. Consequently, spontaneous atomic decay and subsequent atomic excitation during one excitation pulse mainly results in the emission of a first photon into free space. Only the second photon has a non-vanishing probability to be emitted into the cavity output. In our setup, the excitation laser pulse ($\tau_p = 3\,\mathrm{ns}$) is significantly shorter than the on-resonance build-up time for a field inside the cavity ($\tau_{\mathrm{field}} \approx 50\,\mathrm{ns}$). The probability to emit two photons into the cavity is 1×10^{-4}. This is a remarkable suppression by three orders of magnitude below the

free-space bound $p_m(\tau_p = 3\,\text{ns}) = 11\,\%$ deduced in section (3.1).

The possible repetition rate of photon generation is given by the duration of the photon wave packet. The short pulse scheme is based on an atomic two-level system and does not require atomic state repumping. In our system, the photon wave packet amplitude vanishes approximately 150 ns after the excitation pulse. The repetition rate of the excitation pulses may therefore be as high as 6.7 MHz. At reasonable photon generation efficiencies, a single photon source with an emission rate of 1 MHz into a single mode seems feasible.

In summary, the short pulse scheme applied in a cavity QED setting compares well to the free-space case. The retrieval efficiency of photons in a designated spatial output mode is intrinsically high and the contribution of higher order Fock states in the output field is significantly suppressed. We find that the photon generation efficiency is highest on resonance ($\Delta_{\text{ac}} = 0$) and is ultimately bound by the ratio $\kappa/(\kappa + \gamma)$. Compared to the previously studied STIRAP process for photon generation (see section 2.6), the short pulse scheme can produce short photon wave packets (≈100 ns) while potentially operating at MHz repetition rates.

3.4 Experiment and results

3.4.1 Experimental protocol

Single ^{87}Rb atoms are trapped inside the cavity mode at the focus of a standing wave optical dipole trap as described in chapter (2). The experimental protocol for a trapped atom consists of atom cooling intervals (25 μs) alternating with photon production intervals (25 μs). During the photon production intervals, the atom is repeatedly excited with short pulses at a rate of 670 kHz propagating along the $+45^\circ$ axis of the setup. Each photon production interval contains 15 short pulses. The pulses are near-resonant with the atomic $F = 2 \leftrightarrow F' = 3$ transition. A schematic of the experimental setup and the sequence timing is displayed in figure (3.5).

Short excitation pulses with a duration of $\tau_p = 3$ ns are created by amplitude modulation of continuous-wave light using a fiber-coupled electro-optic modulator (EOM)[1]. The on:off ratio of the EOM is finite (company specified 800:1) and we use different strategies to improve the on:off ratio eventually "seen" by the atom. In a first step, we pre-chop the EOM input light with an AOM (AOM pulse duration 300 ns). Secondly, we trigger the EOM to switch only at the end of every AOM pulse such that the trailing edges of AOM pulse and EOM pulse coincide and both contribute to a rapid intensity reduction. We measure an intensity reduction of better than 10^{-3} reached within 8 ns after the pulse peak and decreasing further thereafter (3.6). We observe drifts in the EOM contrast at a

[1] Jenoptik model AM780HF, half-wave voltage 3 V, modulation frequencies DC to 5 GHz, insertion loss 6 dB. The functional principle of the EOM is that of a Mach-Zehnder interferometer in which the path length difference is controlled by an electro-optically induced phase shift. The transmitted optical power can be controlled by tuning the interferometer from constructive to destructive interference at its output.

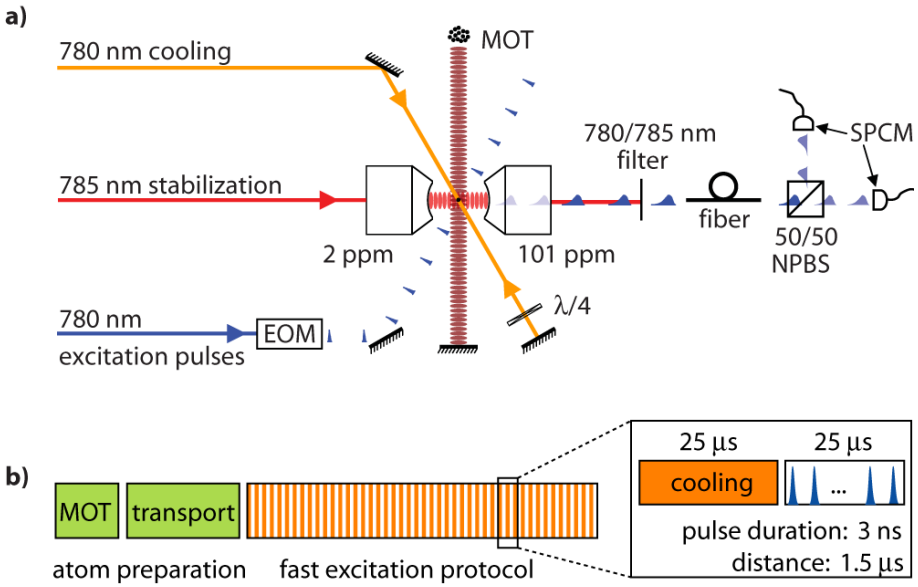

Figure 3.5: Experimental setup for the fast excitation scheme. a) Single Rb atoms are trapped within the TEM_{00} mode of the cavity at the focus of the standing wave dipole trap. Two resonant beams at $\pm 45°$ with respect to the standing wave trap and perpendicular to the cavity axis provide cooling and short pulse excitation. The cavity output is coupled to an optical fiber and guided to the detection setup. SPCM: single photon counting module, NPBS: non-polarizing beam splitter, $\lambda/4$: quarter-wave plate, EOM: electro-optic modulator, MOT: magneto-optical trap. **b)** Experimental protocol used for short pulse excitation. Intervals of atom cooling are interleaved with intervals for fast excitation of the atom-cavity system. One excitation interval contains 15 short laser pulses with a duration of 3 ns at a temporal distance of 1.5 μs.

given fixed offset voltage due to patch charges and thermal effects. Therefore, the optical output of the EOM is permanently monitored and the applied offset voltage is adapted in a feedback loop. Finally, we detune the center frequency of the cw-input light from the Stark shifted atomic resonance and cavity resonance by -30 MHz to suppress continuous-wave excitations [96]. Nevertheless, the atom is excited by the short pulse (measured bandwidth ~ 100 MHz). The excitation pulse energy impinging on the atom (pulse area) is chosen high enough such that the average atomic excitation probability saturates at p_{exc}=50%. We have not been able to reproducibly apply exact π-pulses as the Rabi frequency varies from shot to shot. This is due to atomic Stark shift variations and indeterminate transition strengths because the atom is not prepared in a well-defined Zeeman sublevel.

The cavity output mode is coupled into a single-mode optical fiber and directed to a Hanbury Brown-Twiss photon detection setup consisting of a nonpolarizing beamsplitter and two single-photon counting modules. The total detection efficiency for a single photon present inside the cavity is 34%. The photon detection events on each detector and a trigger time stamp of every short excitation pulse (gate signal) are recorded on a digital counter card (P7888, time resolution 1 ns).

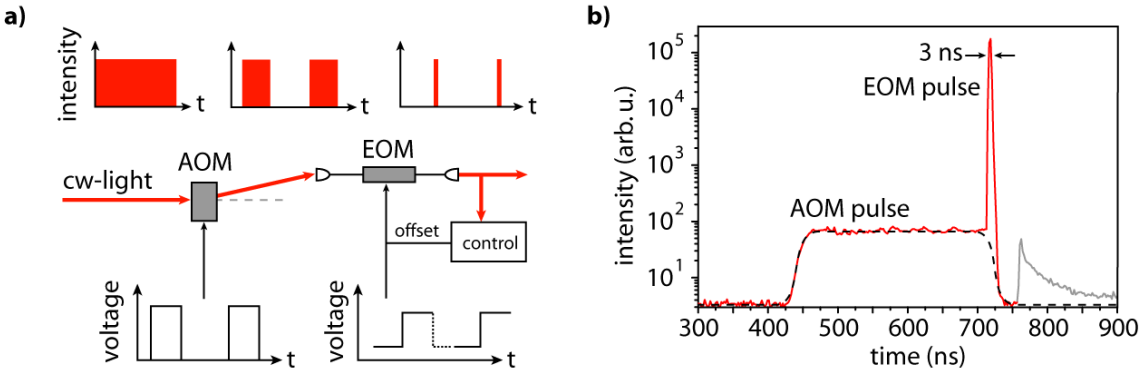

Figure 3.6: Generation of short laser pulses. a) Schematic of the pulse generation setup. Light from a cw-source is chopped by an acousto-optic modulator (AOM) and an electro-optic modulator (EOM) to achieve a high on:off ratio. **b)** The measured pulse intensity shows a peak with 3 ns full width at half maximum. Electronic after-pulsing of the photodetector (grey signal) appears with a probability of 10^{-3} approx. 50 ns after a detection event. This effect is negligible in our measurements.

3.4.2 Single photon generation with a resonant cavity

In a first measurement, we set the cavity frequency resonant with the Stark-shifted $F = 2$ to $F' = 3$ transition (atom-cavity detuning $\Delta_{\mathrm{ac}} = 0\,\mathrm{MHz}$). We infer the wave packet shape of the emitted photons from the temporal probability distribution of photon detection events after each excitation pulse. The measured shape of the photon wave packet is shown in figure (3.7). The peak of the photon emission probability is significantly delayed with respect to a free space exponential decay. The photon wave packet exhibits a smooth envelope function as the vacuum Rabi oscillation is critically damped due to atomic and cavity decay.

Quantitatively, the measured data agrees well with theory. From a numerical fit to the measured wave packet, we obtain a vacuum Rabi frequency $\Omega = 5 \pm 1\,\mathrm{MHz}$ which is consistent with an expected average coupling $g = 3\,\mathrm{MHz}$. The extracted incoherent damping rate of $3.0 \pm 0.2\,\mathrm{MHz}$ matches the a priori known values $\kappa = 2.8\,\mathrm{MHz}$ and $\gamma = 3.0\,\mathrm{MHz}$. The measured probability of emitting a photon into the cavity mode following an excitation pulse is $p'_{phot} = 8 \pm 1\,\%$ close to the theoretical prediction (section 3.3). The photon generation efficiency is mainly limited by spatial g-averaging due to residual atomic motion and by the average atomic excitation probability of $p_{exc} \approx 50\,\%$. Options for improvement are the localization of the atom at a cavity field maximum and improved atomic excitation using well-tailored π-pulses. Together this could lead to an effective photon production efficiency of up to $p'_{phot} = 38\,\%$ in the existing experimental setup.

The single-photon nature of emission is verified by an analysis of the intensity correlation function $g^{(2)}(\tau)$ evaluated from photons arriving within 200 ns after each excitation pulse. We find a $g^{(2)}(\tau)$ function with three distinct features (Fig. 3.7). The comb-like time structure with separations of 1.5 μs corresponds to the succession of short excitation pulses with a repetition rate of 670 kHz. The probability to record coincidences in each

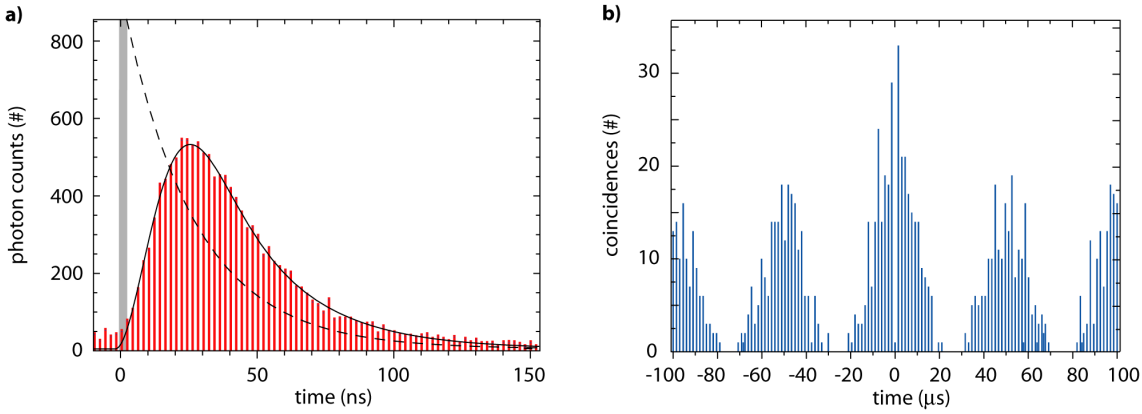

Figure 3.7: Single photons from pulsed excitation. a) Histogram: Shape of the emitted photon wave packets as given by the detection event distribution after the excitation pulse (grey bar). The observed wave packet shape agrees well with theory (black solid line). A calculated photon wave packet shape for emission in free space is given for comparison (dashed line). **b)** Measured second-order correlation function $g^{(2)}(\tau)$ (gated) of the emitted photons. The suppression of coincidences at $\tau = 0$ verifies the single photon character of the emission. The triangular envelope function is a convolution of photon production and cooling intervals (see text for details).

of these time bins is modulated with a triangular envelope function. It stems from the convolution of photon production intervals (25 μs) with interleaved cooling intervals of the same duration. Most important, we observe a high suppression ($> 90\,\%$) of coincidence events at time $\tau = 0$ demonstrating that the protocol does indeed result in single photons. The remaining coincident detections stem from dark counts of the SPCM's ($\leq 2\,\%$) and from multiple trapped atoms ($\leq 8\,\%$ due to probabilistic atom loading, single atom imaging was not implemented at this point).

3.4.3 Observation of vacuum Rabi oscillations

The coherent exchange of energy between a single atom and the cavity mode is most strikingly observed when the characteristic oscillation frequency is higher than the incoherent damping rates (see section 3.2). In the following measurements, we increase the generalized vacuum Rabi frequency Ω by detuning the cavity frequency from the Stark-shifted atomic resonance by Δ_{ac}. The system then oscillates at a frequency

$$\Omega = \sqrt{4g^2 + \Delta_{\mathrm{ac}}^2} \tag{3.13}$$

between the states $|e,0\rangle$ and $|g,1\rangle$ (Eq. 3.3). Note that $\kappa \approx \gamma$ in our setup and hence frequency shifts due to damping are negligible. However, for single atoms loaded into the deep standing-wave dipole trap, Stark shift variations lead to an uncertainty in Δ_{ac}. A more precise Ω is maintained in the shallow running-wave dipole trap. In this dipole trap configuration, atoms drift through the cavity at low overall densities. We ensure that the average number of atoms in the cavity is much less than one (verification by $g^{(2)}(\tau)$ measurements). The intermittent atom cooling and photon production intervals are simply replaced by one long photon production interval spanning the whole experimental

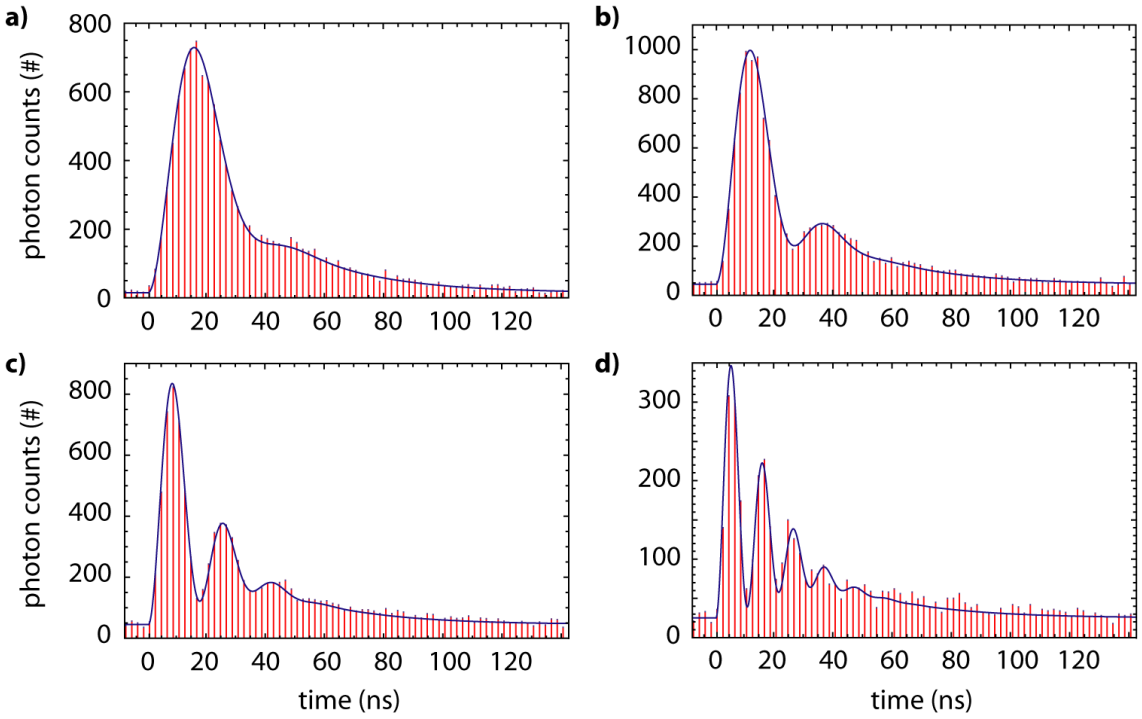

Figure 3.8: Observation of vacuum Rabi oscillations. The red histograms show the wave packet shape of the emitted single photons for different atom-cavity detunings $\Delta_{ac}/2\pi$: **a)** 25 MHz, **b)** 35 MHz, **c)** 55 MHz, **d)** 95 MHz. The distinct modulations stem from the population dynamics of state $|g,1\rangle$ and correspond to the coherent exchange of energy between atom and cavity field. The solid lines are numerical fits (see text for details).

sequence. For controlling Δ_{ac}, we vary the cavity frequency while keeping the trap depth and atomic frequency constant.

The measured single-photon wave packets at different detunings Δ_{ac} are shown in figure (3.8). The wave packet envelopes exhibit strong modulations corresponding to the population dynamics of state $|g,1\rangle$. Note that no externally applied driving field is present during the oscillations, and the observed features are not due to many-photon or many-atom effects [91, 97, 98]. Qualitatively, we find good agreement between the measured photon wave packet shapes and the theoretical prediction (section 3.3). For quantitative agreement, the analytical fit model applied here (solid lines in Fig. 3.8) also includes an experimental shot-to-shot uncertainty of the generalized vacuum Rabi frequency Ω using a Gaussian distribution of fixed width (10 MHz). This phenomenologically accounts for the combined effects of small variations of Δ_{ac} and the position-dependence of g. From the numerical fits to the data, we extract values of the oscillation frequency Ω as a function of atom-cavity detuning Δ_{ac} (Fig. 3.9). The extracted frequencies match well the predicted hyperbolic function (Eq. 3.13) with a reduced chi-squared $\chi^2 = 1.13$. These observations testify to the high degree of control which is achieved in this system of one atom and one photon.

Our results represent normal-mode spectroscopy of the coupled single atom-cavity system

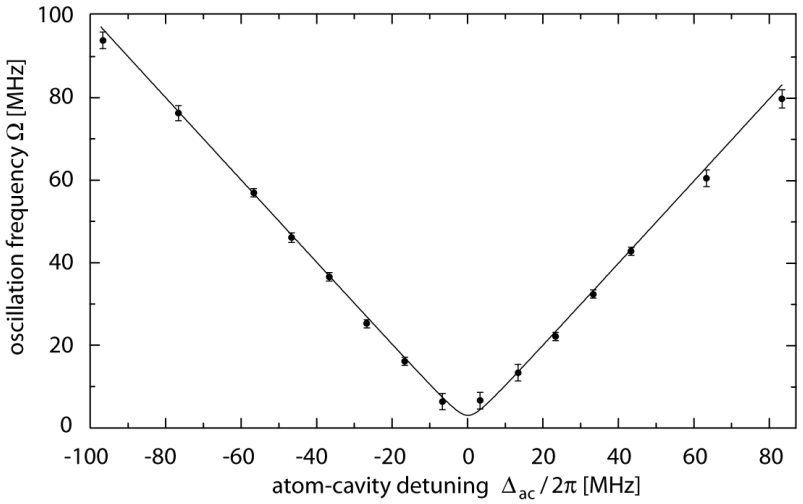

Figure 3.9: Normal-mode spectroscopy in the time domain. From numerical fits to the measured photon shapes we extract the coherent atom-cavity oscillation frequencies (dots) as a function of atom-cavity detuning Δ_{ac}. The solid line shows the calculated generalized vacuum Rabi frequency $\Omega = \sqrt{4g^2 + \Delta_{\mathrm{ac}}^2}$. Our data matches this hyperbolic function with a reduced chi-squared $\chi^2 = 1.13$. The deduced average coupling constant is $g = 2\pi \times (2 \pm 1)\,\mathrm{MHz}$.

in the time domain. The observed modulation in the photon shape originates from a quantum beat of the first pair of atom-cavity dressed states [99]. The emitted single photons are in a superposition of two frequencies with a fixed relative phase.

3.4.4 Short pulse excitation of the cavity mode

A complementary illustration of the coherent exchange of one quantum of energy between atom and cavity is investigated by short pulse excitation of the cavity mode. In this case, the system is (approximately) initialized in state $|g, 1\rangle$. With respect to the previous experiments, this swaps the role of $c_g(t)$ and $c_e(t)$ in the temporal evolution of the coupled system (Fig. 3.10).

The experimental protocol follows that of the experiment described in section (3.4.3) but with on average one atom present in the cavity (continuous loading regime, chapter (2)). The excitation pulses are coupled into the cavity through the input mirror. The pulses are weak such that one photon is deposited in the cavity in only 10 % of all attempts and contributions of higher Fock states are negligible. The atom-cavity detuning is set to $\Delta_{\mathrm{ac}} = 0$.

The light pulse emitted from the atom-cavity system exhibits a clear deviation from a purely exponential decay of the intracavity field (Fig. 3.10). The observed behavior is explained by the temporary storage of excitation in the atom during half of a vacuum Rabi oscillation. Quantitatively, we can retrieve the temporal evolution of the population in state $|e, 0\rangle$ by subtracting the measured pulse from the exponential decay curve of the

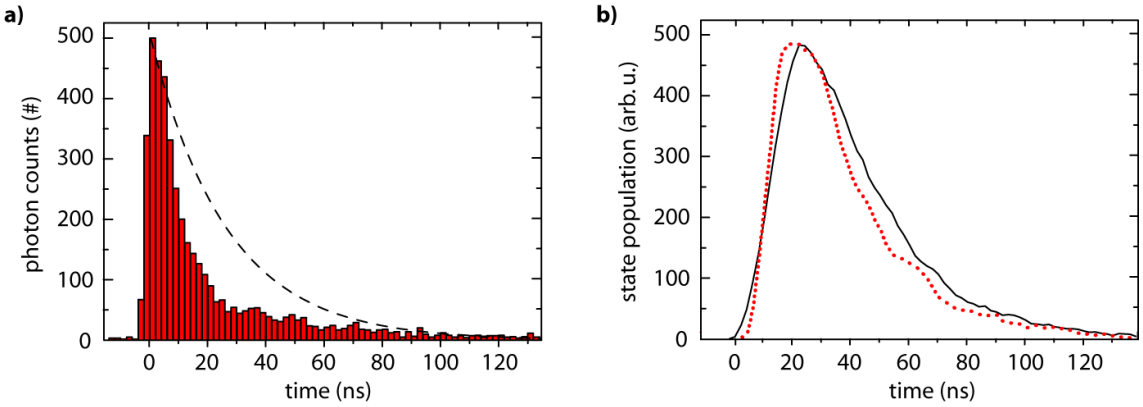

Figure 3.10: Short pulse excitation of the cavity mode. a) Histogram: Measured photon arrival time distribution after excitation of the cavity with ~ 1 atom present. Dashed line: Exponential decay of the cavity field intensity without atoms. **b)** The difference between the two curves in a) reflects the occupation of state $|e,0\rangle$. This extracted difference signal (dots) is compared with the emitted photon shape when the atom is excited (solid line, data of section 3.4.2). The nearly identical time evolution of $c_g(t)$ when the atom-cavity system is initialized in state $|e,0\rangle$ (solid line) and the evolution of $c_e(t)$ when the system is initialized in $|g,1\rangle$ (dots) illustrates the complementary role of $c_g(t)$ and $c_e(t)$ in the coupled atom-cavity system.

empty cavity. In Fig. (3.10b), the obtained curve for $c_e(t)$ is compared with the measured evolution of $c_g(t)$ (i.e. photon shape) from the experiment of section (3.4.2). The nearly identical time dependence of the two signals shows the complementary role of $c_g(t)$ and $c_e(t)$ when the system is initialized in either $|e,0\rangle$ or $|g,1\rangle$.

3.5 Discussion and Outlook

In this chapter we have theoretically analyzed and experimentally implemented short pulse excitation of a single atom-cavity system. The presence of the cavity dramatically alters the dynamics of the emission process compared to an atom in free space. The coupled system evolves with a coherent oscillatory energy exchange between the atom and the cavity, damped by atomic and cavity decay. The wave packet of the emitted photon is governed by the evolution of the coupled atom-cavity system – independent of the excitation pulse shape and frequency. The cavity frequency constitutes a control parameter by which the shape and the frequency spectrum of the emitted photon can be controlled. The observed behaviour constitutes a fundamental example of cavity QED at the level of one atom and one photon.

Compared to photon generation with an atom in free space, the cavity scheme benefits from a high efficiency with which photons are generated in a designated output mode. Further, two-photon emission events are strongly suppressed. A single photon generation efficiency of 8 % at a repetition rate on the order of 1 MHz has been achieved in the experiment. The parameters of our setup may in the future allow a generation efficiency of close to 40 % when a single atom can be permanently located at a maximum of the

cavity field.

Photon generation by the short pulse scheme also presents an alternative to the previously studied cavity-mediated STIRAP process (chapter 2, [100]). Pulsed excitation is based on a closed two-level transition and does not require atomic state repumping. The generated photons are much shorter (100 ns) than photons typically created in the STIRAP process (1 μs). Even at moderate absolute efficiency, this potentially translates into the generation of single photons in a well-defined mode at a retrieval rate on the order of 1 MHz.

A drawback of the pulse scheme is the mapping of atomic Stark shift variations onto the frequency spectrum of the photon. This problem can be avoided by using very shallow dipole traps (low absolute Stark shifts), using traps at "magic wavelengths" or by cooling the atom to the ground state of a deep trap. Further, the generation of time symmetric photon wave packets can only be accomplished at low efficiencies [101] – while such photons would be desirable for quantum networking [68]. The generation of frequency entangled atom-photon pairs from short pulse excitation [102] is complicated by the spectral filtering of the cavity. However, a solution to this might be frequency matching of an integer multiple of the atomic hyperfine splitting with the free spectral range of the cavity.

In future experiments, our scheme may find application in the investigation of higher-lying dressed states in cavity QED systems [50] and for generation of multi-photon Fock states [103]. Additionally, a single photon in a superposition of two tunable frequencies, as demonstrated here, may be useful as a frequency qubit [104, 105]. Finally, this technique can improve existing atom-photon entanglement experiments by reducing unwanted multiple-photon events [100] and is extendable to multi-photon entanglement protocols [106].

4 State detection of a single atom in a cavity

Efficient internal state detection of single neutral atoms is at the basis of atomic physics and is highly relevant for quantum information science. In a single atom, the quantum bit (qubit) is often encoded in or mapped onto atomic hyperfine states. In this chapter, we show that coupling the atom to a cavity establishes a superior readout channel for internal atomic states. We introduce a state detection scheme based on cavity-enhanced fluorescence and realize state readout by differential cavity transmission. In an experiment with a single trapped ^{87}Rb atom, we achieve a hyperfine state detection fidelity of 99.4% in 85 μs while a result is obtained in every readout attempt. Most important, the qubit is interrogated many hundred times without loss of the atom. This presents an essential advancement for the speed and scalability of quantum information protocols based on neutral atoms. Further, the general principles outlined here may be applied to the readout of other optically accessible systems such as cold molecules, NV-centers in diamond or quantum dots.

This chapter is organized as follows. We first introduce basic concepts of state detection and give a definition of the readout fidelity (sec. 4.1). In section (4.2), cavity-enhanced fluorescence detection is theoretically studied, followed by the presentation of the experimental results (sec. 4.2.4). The use of a cavity also allows for atomic hyperfine state readout via differential transmission (sec. 4.3). A comparative discussion of the two detection schemes is given in section (4.4). Finally, we present applications of the cavity-enhanced fluorescence method for Stark shift spectroscopy and magnetic field measurement (sec. 4.5).

The results presented in this chapter have partially been published in:
"Lossless state detection of single neutral atoms"
J. Bochmann, M. Mücke, C. Guhl, S. Ritter, G. Rempe, and D. L. Moehring,
Physical Review Letters **104**, 203601 (2010).

4.1 Introduction

4.1.1 Methods for atomic state detection

In view of quantum information, internal atomic states may serve as stationary quantum bits. In a single atom, the quantum bit (qubit) is typically encoded in or can be mapped onto atomic hyperfine states. However, hyperfine qubit readout has proven remarkably difficult for neutral atoms and an adequate concept remained to be shown. Existing protocols either do not obtain an answer in every readout attempt [107, 108], they require strong atom-cavity coupling [109, 110, 111] or they are intrinsically destructive and cause loss of the atom during detection [112, 113, 114, 115, 71, 43, 116]. In this chapter, we

investigate means of single atom readout which can overcome these problems.

The performance of a method for internal state detection can be judged by its speed, fidelity and repeatability. Following an interpretation by diVincenzo [31], a readout protocol should be qubit-specific, efficient, fast, and non-destructive. The qubit-specific aspect refers to the addressability of single carriers of quantum information. Efficiency implies that an answer should be obtained in most readout attempts and this answer should be correct. Further, a readout scheme is fast, when it operates well within the qubit decoherence time. The non-destructive aspect of the measurement process refers to the possibility of repeated measurement of the qubit while the same result is obtained in every attempt. However, if the efficiency of the readout protocol is high this requirement may be dispensable. Nevertheless, it would be advantageous to not destroy the physical carrier of the qubit upon readout and we rephrase this requirement as "lossless".

The most widely used method for atomic state readout is fluorescence detection. Today, it is the standard technique in experiments with single trapped ions. In this scheme, a single atom is state-selectively excited by a probe laser and the scattered fluorescence light is detected. Atomic hyperfine states can be distinguished as the probe laser resonantly couples only one of them (the "bright state") to an excited state. If the atom is in the other hyperfine state ("dark state"), no excitation occurs and no fluorescence light is detected. This method has been successfully applied to single ions in Paul traps [117, 118, 119, 120, 121]. Recent experiments report readout fidelities as high as 99.99% with a single trapped calcium ion [122]. Although a powerful tool, fluorescence state detection has never been realized with a trapped neutral atom. This is due to the difficulty to detect a sufficient number of scattered photons from an atom in the bright state before ejecting it from an optical dipole trap. Instead, this loss can be used to signal the atomic state.

Hyperfine state-dependent loss of atoms has been used for atomic state detection with push-out schemes [112, 113, 114, 115, 71]. A resonant probe laser ejects atoms in the bright state from the optical dipole trap by means of radiation pressure. Atoms in the dark state are unaffected and remain in the trap. After a push-out attempt, the presence of atoms in the trap is tested by detecting light scattered by an atom from cooling and repumping laser beams in an optical molasses configuration. Note that this type of fluorescence collection itself is not useful for internal state detection. It employs repumping light and is therefore not state-specific. The push-out scheme is intrinsically destructive and results in loss of the atom. Its fidelity is limited by concurrent loss of dark state atoms. In state-of-the-art experiments, fidelites of up to 98 % within 10 to 30 ms can be achieved [115, 113].

Another destructive approach is state-dependent ionization of atoms [116, 42]. Here, the atoms are state-selectively ionized by laser light. In a static electric field, the charged fragments are attracted to detectors (multi-channel plates) and cause an electronic signal. While this technique is destructive, the fragments can be detected with almost unit efficiency. In combination with the high detection speeds (limited only be the drift time of the fragments), state-dependent ionization is in principle capable of closing the locality and detection loop-hole in Bell inequality tests (fidelity above 95 % within 1 μs) [116].

In this chapter we show that optical readout of the atomic state can benefit from the use

of a cavity in two ways. On the one hand, the optical resonator can amplify the coupling between the probing light field and the atom. In a typical realization, the probe light transmission of the atom-cavity system depends on the hyperfine state of the atom. This concept is well suited for the strong-coupling regime of cavity QED [111]. On the other hand, the optical resonator can amplify the coupling between the atom and the detector via the Purcell effect. This situation corresponds to cavity-enhanced fluorescence detection and is well suited for the "bad cavity" regime of CQED.

The theoretical analysis and experimental implementation of both differential transmission and cavity-enhanced fluorescence detection are the subject of the following sections.

4.1.2 Definition and calculation of the fidelity

We consider a physical system prepared in one of the two quantum states $|0\rangle$ and $|1\rangle$. We define the fidelity $\mathcal{F}$ of state detection as the minimum probability with which the correct quantum state is obtained in any readout attempt. First, we identify all possible decisions for a given measurement outcome in a tree diagram (Fig. 4.1). The probability for a false decision is $E_{|0\rangle}$ and $E_{|1\rangle}$ respectively. The probabilities for correct or no answer are labelled C_i and N_i ($i \in \{|0\rangle, |1\rangle\}$) with $C_i + N_i + E_i = 1$.

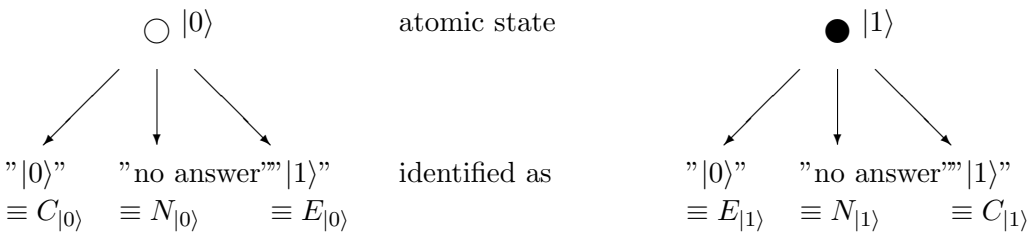

Figure 4.1: Tree diagram of state detection. We can identify all possible decisions for a given measurement outcome. The probability for a false decision is $E_{|0\rangle}$ and $E_{|1\rangle}$ respectively. The probabilities for correct or no answer are labelled C_i and N_i ($i \in \{|0\rangle, |1\rangle\}$) with $C_i + N_i + E_i = 1$.

We require that a decision is made for every measurement outcome and therefore $N_i = 0$. We can now define the fidelity as

$$\mathcal{F} = 1 - \max\left\{E_{|0\rangle}, E_{|1\rangle}\right\} = \min\left\{C_{|0\rangle}, C_{|1\rangle}\right\}. \tag{4.1}$$

We note that this is a conservative yet not the only possible definition of a state detection fidelity. In the literature, one also finds $\mathcal{F} = 1 - \left(E_{|0\rangle} + E_{|1\rangle}\right)/2$ [122], which a priori assumes preparation of the atom in either of two states with equal probability.

In optical state readout schemes, a certain number of photons N_{det} is detected in a given readout attempt. A decision about the atom's state is made by comparison of N_{det} with a discrimination level d: $N_{det} \leq d$ or $N_{det} > d$. The fidelity of the readout protocol can be optimized by appropriate choice of d. The number of detected photons may be given by probability distributions $p_{|0\rangle}(n)$ and $p_{|1\rangle}(n)$ with mean values $\lambda_{|0\rangle}$ and $\lambda_{|1\rangle}$. We choose

$\lambda_{|0\rangle} \leq \lambda_{|1\rangle}$. Using the relations

$$C_{|0\rangle} = \sum_{n=0}^{d} p_{|0\rangle}(n) \quad \text{and} \quad C_{|1\rangle} = \sum_{n=d+1}^{\infty} p_{|1\rangle}(n) \tag{4.2}$$

we can find the optimum discrimination level d by calculating the achievable fidelity according to:

$$\mathcal{F} = \max_{d} \left\{ \min \left\{ \sum_{n=0}^{d} p_{|0\rangle}(n), 1 - \sum_{n=0}^{d} p_{|1\rangle}(n) \right\} \right\}. \tag{4.3}$$

The probability distributions $p_i(n)$ are normalized to 1 ($\sum_{n=0}^{\infty} p_i(n) = 1$). While the actual probability distributions $p_{|0\rangle}(n)$ and $p_{|1\rangle}(n)$ may take arbitrary forms, shot-noise dominated Poisson distributions with mean values $\lambda_{|0\rangle}$ and $\lambda_{|1\rangle}$ are often reasonable approximations:

$$p\left(\lambda_i, n\right) = \frac{\lambda_i^n}{n!} e^{-\lambda_i}. \tag{4.4}$$

The standard deviation $1/\sqrt{\lambda_i}$ is relatively large for small λ. The overlap of the two distributions can be reduced by detecting a larger number of photons.

We can obtain a first insight into the achievable fidelity by introducing a contrast parameter $K \equiv 1 - \lambda_{|0\rangle}/\lambda_{|1\rangle}$ taking values between 0 and 1. The fidelity $\mathcal{F}(K, \lambda_{|1\rangle})$ as a function of contrast and mean detected photon number is depicted in (Fig. 4.2). At high values of contrast ($K \simeq 1$), a fidelity of more than 99% is achievable with $\lambda_{|1\rangle} \geq 5$. At a contrast of $K = 50\%$, a fidelity of 99% requires appriximately $\lambda_{|1\rangle} = 80$ detected photons ($\lambda_{|0\rangle} = 40$). We will see later, that these two cases correspond to the experimental situations of cavity-enhanced fluorescence detection and differential cavity transmission.

4.2 Cavity-enhanced fluorescence state detection

4.2.1 Fluorescence scattering of an atom coupled to a cavity

We consider a single atom coupled to a cavity and continuously driven by a probe laser which is applied transverse to the cavity axis. The rate of scattered photons R_{scat} at the cavity output can be obtained from a master equation approach [92, 76]. The rate scales with the excitation probability P_{e} of the intracavity atom as

$$R_{\text{scat,cav}} = 2\kappa \frac{g^2}{\Delta_c^2 + \kappa^2} P_{\text{e}}, \tag{4.5}$$

where the excitation probability of the atom in free space $P_{\text{e,free}}$ is affected by the presence of the cavity as

$$P_{\text{e}} = P_{\text{e,free}} / (|1 - \nu|^2) \tag{4.6}$$

$$\nu = g^2 / \left((\Delta_a - i\gamma) (\Delta_c - i\kappa) \right). \tag{4.7}$$

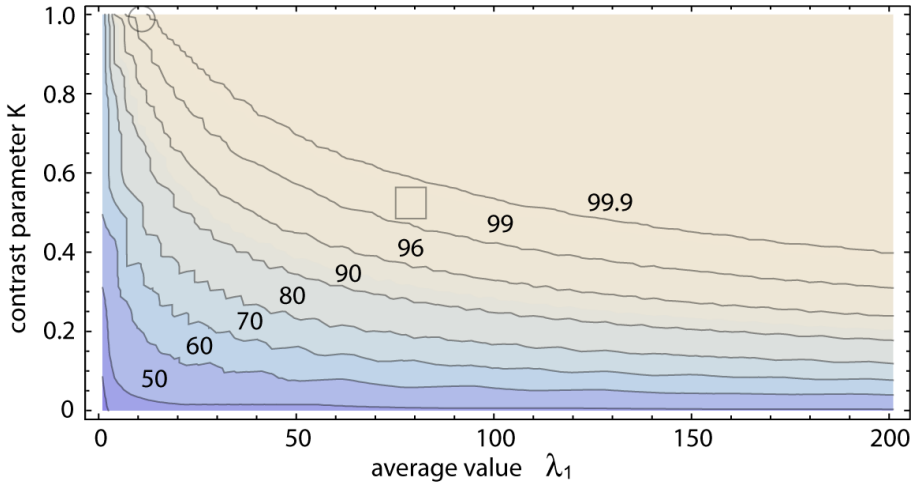

Figure 4.2: Fidelity of state detection for Poissonian detection event distributions. Shown here is the maximum achievable fidelity as a function of contrast $K \equiv 1-\lambda_{|0\rangle}/\lambda_{|1\rangle}$ and mean number of detected photons $\lambda_{|1\rangle}$ assuming Poissonian probability distributions $p_{|0\rangle}(n)$ and $p_{|1\rangle}(n)$ for the number of detected photons n. In view of the experiments presented in this chapter, the regimes of cavity-enhanced fluorescence detection (circle) and of differential transmission (square) are indicated. The numbers in the graph indicate the achievable fidelity in (%).

The complex cooperativity ν includes the detuning of atom Δ_a and cavity Δ_c with respect to the probe laser, where γ and κ are the atomic polarization and the cavity field decay rate and g is the coherent atom-cavity coupling constant. Equation (4.5) is valid in the limit of weak driving (low saturation of the atom) and care must be taken for correctly evaluating the limit $\Delta_c \to 0$ and $\kappa \to 0$ [92].

4.2.2 Statistical analysis

In this section, we derive a statistical description of the fluorescence state detection method. Our main goal is to calculate the achievable fidelity. The central problem we need to solve is the analytic description of the probability distribution $p(n)$ for n detection events taking into account optical pumping and dark counts.

We want to distinguish the two hyperfine ground states $|5^2\mathrm{S}_{1/2}\, F=2\rangle$ and $|5^2\mathrm{S}_{1/2}\, F=1\rangle$ of a single ^{87}Rb atom by the number of detected fluorescence photons in a given probe pulse of duration τ_D. We choose probe laser and cavity frequencies to be resonant with the cycling transition $|5^2\mathrm{S}_{1/2}\, F=2\rangle \leftrightarrow |5^2\mathrm{P}_{3/2}\, F'=3\rangle$, making $F=2$ the bright state and $F=1$ the dark state. While for an atom in $F=2$ the scattering rate $R_{\mathrm{scat,cav}}$ is high, for an atom prepared in $F=1$ it vanishes due to a large detuning $\Delta_a/2\pi \simeq 6.8\,\mathrm{GHz}$. This contrast should in principle allow a high state detection fidelity. However, the fidelity is limited by the occurence of detector dark counts and atomic hyperfine state pumping induced by the probe laser. The probability distributions for the number n of detection events $p_{\mathrm{k}}(n)$ with k=(dark, bright) are affected by these processes in a complex way.

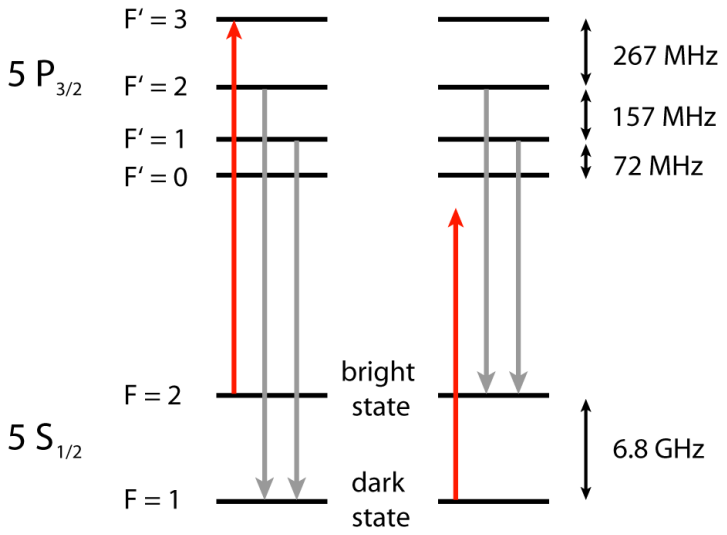

Figure 4.3: Off-resonant optical pumping induced by the probe laser. The probe laser (red arrow) is near-resonant with the $F = 2 \leftrightarrow F' = 3$ transition (D2 line of ^{87}Rb). Off-resonant excitation of $F' = 2$ und $F' = 1$ can lead to spontaneous decay into either of the ground states $F = 1$ and $F = 2$ which introduces an unwanted pumping process between the hyperfine ground states during state detection (gray arrows). However, the large ground state hyperfine splitting $\omega_{\mathrm{HFS}} = 6.8$ GHz effectively suppresses dark-to-bright state pumping via $F = 1 \leftrightarrow F' = 1, 2$ as the probe is then detuned by the same amount. Bright-to-dark pumping is governed by the much smaller excited state hyperfine splittings $\omega_{\mathrm{HFP}}/2\pi \approx 0.3$ GHz but its probability is significantly affected by probe laser polarization (see text for details).

Atomic state pumping induced by the probe laser is a fundamental problem of fluorescence state detection (Fig. 4.3). While resonant with the cycling transition $F = 2 \leftrightarrow F' = 3$, the probe laser can off-resonantly couple the dark state $F = 1$ to the excited states $F' = 1, 2$ from where decay into the bright state $F = 2$ can occur. If the probe polarization is not well-defined, the probe laser can also off-resonantly couple $F = 2$ to $F' = 1, 2$ from where decay into the dark state $F = 1$ is possible. In the following, we neglect higher order processes (multiple pumping between bright and dark state). The probability of optical pumping at time t is given by

$$f(t) = \frac{1}{\tau_k} e^{-\frac{t}{\tau_k}} \tag{4.8}$$

where τ_k is the average time until optical pumping occurs and $0 \leq t \leq \tau_D$. The average number of detected photons λ' is proportional to the time the atom is in the bright state:

$$\lambda'(t) = \begin{cases} \left(1 - \frac{t}{\tau_D}\right)\lambda & \text{(atom initially in dark state)} \\ \left(\frac{t}{\tau_D}\right)\lambda & \text{(atom initially in bright state)} \end{cases} \tag{4.9}$$

with λ the mean detected photon number for an atom in the bright state during the whole probe interval. The time-based probability distribution $f(t)$ can be transformed into a distribution $g_k(\lambda')$. We define

$$\alpha_k = \frac{\tau_D \eta}{\tau_k \lambda} \tag{4.10}$$

as the probability per scattered photon to pump out of state k. It is scaled by the total detection efficiency η of a scattered photon. We use (4.9) and substitute $t(\lambda')$ in (4.8) to obtain probability distributions $g_k(\lambda')$ for the mean number of detected photons:

$$g_{dark}(\lambda') = \begin{cases} \frac{\alpha_{dark}}{\eta} e^{(\lambda'-\lambda)\alpha_{dark}/\eta} & \lambda' > 0 \\ e^{-\alpha_{dark}\lambda/\eta} & \lambda' = 0 \end{cases} \tag{4.11}$$

$$g_{bright}(\lambda') = \begin{cases} \frac{\alpha_{bright}}{\eta} e^{-\alpha_{bright}\lambda'/\eta} & \lambda' < \lambda \\ e^{-\alpha_{bright}\lambda/\eta} & \lambda' = \lambda \end{cases} \tag{4.12}$$

For the cases in which no optical pumping occurs during τ_D, the functions $g_k(\lambda')$ are separately defined.

The probability distribution $p_k(n)$ for the number of detected photons is a convolution of the mean value distributions $g_k(\lambda')$ with the Poisson distributions $P(n,\lambda') = \frac{e^{-\lambda'}\lambda'^n}{n!}$. We find for an atom initially prepared in the dark state:

$$p_{\mathrm{dark}}(n) = \delta_{n0} e^{-\alpha_{dark}\lambda/\eta} + \int_\epsilon^\lambda \frac{e^{-\lambda'}\lambda'^n}{n!} \frac{\alpha_{dark}}{\eta} e^{(\lambda'-\lambda)\alpha_{dark}/\eta} d\lambda' \tag{4.13}$$

with δ_{ij} the Kronecker-Delta symbol and $\epsilon \to 0$. This exact function can be rewritten [119] in terms of the regularized Gamma function $\mathcal{P}(a,x) = \frac{1}{(a-1)!}\int_0^x e^{-y} y^{a-1} \mathrm{d}y$ as

$$p_{\mathrm{dark}}(n) = e^{-\alpha_{dark}\lambda/\eta} \left[\delta_{n0} + \frac{\alpha_{dark}/\eta}{(1-\alpha_{dark}/\eta)^{n+1}} \mathcal{P}(n+1, (1-\alpha_1/\eta)\lambda) \right]. \tag{4.14}$$

Note that in this form the function is not defined for $\alpha_{dark}/\eta = 1$, while in integral form it is well defined. Equivalent to the dark state case, we can deduce the probability distribution for the number of detected photons for an atom initially prepared in the bright state.

$$p_{\mathrm{bright}}(n) = e^{-(1+\alpha_{bright}/\eta)\lambda} \frac{\lambda^n}{n!} + \int_0^\lambda \frac{e^{-\lambda'}\lambda'^n}{n!} \frac{\alpha_{bright}}{\eta} e^{\lambda'\alpha_{dark}/\eta} d\lambda' \tag{4.15}$$

$$p_{\mathrm{bright}}(n) = \frac{\lambda^n e^{-(1+\alpha_{bright}/\eta)\lambda}}{n!} + \frac{\alpha_{bright}/\eta}{(1+\alpha_{bright}/\eta)^{n+1}} \mathcal{P}(n+1, (1+\alpha_{bright}/\eta)\lambda) \tag{4.16}$$

In addition to the scattered photon signal, dark counts contribute to the number of detection events from each probe interval. Dark counts originate from intrinsic electronic noise of the detector and from stray light impinging on the detector. The average number of dark counts λ_{dc} in a given detection time window τ_D is given by $\lambda_{\mathrm{dc}} = R_{\mathrm{dc}}\,\tau_D$ where R_{dc} is the average dark count rate. The probability distribution $p_{\mathrm{dc}}(\lambda_{\mathrm{dc}}, n)$ of the number of dark counts n is assumed to be Poissonian. Finally, we obtain for the probability distribution of n detection events and an atom intially prepared in state k:

$$p_{\mathrm{k,total}}(n) = \sum_{i=0}^{n} p_k(i) \cdot p_{\mathrm{dc}}(n-i). \tag{4.17}$$

For high fidelity readout, α_k must be small. For our choice of the fluorescence detection scheme, the most relevant process is bright-to-dark state pumping enabled by off-resonant excitation of the $F' = 2$ ($F' = 1$) level which is only separated by 267 MHz (424 MHz) from $F' = 3$ (Fig. 4.3). These hyperfine splittings must be compared with the transition linewidth of $2\gamma = 6\,\mathrm{MHz}$. Bright-to-dark pumping can be significantly suppressed by defining a quantization axis (magnetic field) in combination with circularly polarized probe light which renders the off-resonant transitions dipole-forbidden. However, dark-to-bright state pumping can not be avoided although it generally occurs with very low probability (Fig. 4.3). The reason is the large S-state hyperfine splitting ($\omega_{HFS} = 6.8$ GHz $\gg$ $\omega_{HFP} = 267$ MHz).

In the following, we determine α_k quantitatively. The concept is straightforward: We need to evaluate the probabilities of all dipole-allowed paths connecting possible initial and final atomic states for a fluorescence photon scattering event. From these values, the relative probability of paths which lead to hyperfine ground state pumping can be determined. Hence we find for the normalized optical pump probabilities α_k per scattered photon:

$$\alpha_k = \frac{\sum_{e,i\neq f} p_{\mathrm{i,e,f}}}{\sum_{i,e,f} p_{\mathrm{i,e,f}}}. \tag{4.18}$$

The indices (i,e,f) denote the initial hyperfine ground state F=i, the excited hyperfine state F'=e and the final hyperfine ground state F=f. The probability $p_{\mathrm{i,e,f}}$ of a single excitation-decay path is a product of three terms:

$$p_{\mathrm{i,e,f}} = \mathrm{CG}_{\mathrm{i,e,f}} \times \frac{s/2}{1 + s + (\delta_{i,e}/\gamma)^2} \times \beta_{e,f}. \tag{4.19}$$

The first term incorporates the transition probabilities as given by the dipole matrix elements (Clebsch-Gordan coefficients) of the path. The second term determines the probability with which state F'=e is excited by the probe laser. The third term takes into account the Purcell-enhancement of certain decay paths due to the presence of the cavity.

The Clebsch-Gordan term $\mathrm{CG}_{\mathrm{i,e,f}}$ is a sum of all paths from i via e to f over all allowed Zeeman-sublevel transitions. However, in the excitation step of each path (i→e) only Zeeman-levels coupled by the probe laser polarization $q = (-1, 0, 1) = (\sigma^-, \pi, \sigma^+)$ must be taken into account whereas in the decay process all polarizations q' are allowed.

$$\mathrm{CG}_{\mathrm{i,e,f}} = \sum_q \frac{1}{q_{rel}} \sum_{m_F=-F}^{+F} \left[C(F = i, F' = e; m_F, m_F + q) \sum_{q'=-1}^{+1} C(F = f, F' = e; m_{F'} - q', m_{F'}) \right] \tag{4.20}$$

Here, $C(F, F'; m_F, m_{F'})$ is the squared Clebsch-Gordan coefficient of the transition $|F, m_F\rangle \leftrightarrow |F', m_{F'}\rangle$ (following the conventions in [79, 119]) and q_{rel} is the relative power of each probe laser polarization component with sum normalized to 1.

The second term of (Eq. 4.19) determines the probability with which state F'=e is excited by the probe laser with a detuning $\delta_{i,e}$ from the i→e transition and a saturation parameter $s = I/I_{\mathrm{sat}}$.

The third term $\beta_{e,f}$ of equation (4.19) makes a correction to the free space atomic transition probabilities as given by the Clebsch-Gordan coefficients. The presence of the cavity enhances the atomic polarization decay by means of the Purcell effect. For an atom in the excited state, this leads to a competition between emission into 4π solid angle and emission into the cavity mode. In analogy to equation (4.5), we find $\beta_{e,f} = 1 + |\nu_{e,f}|$. The presence of the cavity changes the branching ratio for decay into the two hyperfine ground states by means of a Purcell enhancement. With regard to state detection, this leads to a relative suppression of unwanted bright-to-dark state pumping.

We are now able to calculate the values α_k for our experiment. For low saturation ($s \approx 0.1$), lin⊥lin-polarized probe laser and vanishing probe detuning ($\delta_{2,3} = 0$), the pump probabilities per scattered photon are $\alpha_{\mathrm{dark}} = 5 \times 10^{-8}$ and $\alpha_{\mathrm{bright}} = 2 \times 10^{-5}$. Equation (4.18) for the pump probabilities α_k usually involves a large number of terms and requires numerical evaluation. However, many of these terms are small. We can obtain a simplified expression when $\delta_{2,3} \ll \omega_{HFP}$ and $s \leq 0.1$. The denominator of equation (4.18) is then dominated by the (2,3,2) path, all other terms are strongly suppressed by $(\delta_{i,e}/\gamma)^2$. The approximated bright-to-dark state pump probability per scattered photon reads:

$$\alpha_{\mathrm{bright}} = \left(\frac{\mathrm{CG}_{2,2,1}}{1 + (\delta_{2,2}/\gamma)^2} + \frac{\mathrm{CG}_{2,1,1}}{1 + (\delta_{2,1}/\gamma)^2} \right) \frac{1 + (\delta_{3,2}/\gamma)^2}{\beta_{3,2}} \tag{4.21}$$

An equivalent expression can be obtained for α_{dark}.

The analytic expressions for $p_{\mathrm{dark,total}}(n)$ and $p_{\mathrm{bright,total}}(n)$ derived in this section are the basis for calculating the state detection fidelity. The achievable fidelity is calculated for a given parameter set $(\lambda, s, \tau_D, R_{dc}, \eta, \delta_{i,e})$ by numerically finding an optimum discrimination level d for the two detection event distributions.

$$\mathcal{F} = \max_d \left\{ \min \left\{ \sum_{n=0}^{d} p_{\mathrm{dark,\ total}}(n), 1 - \sum_{n=0}^{d} p_{\mathrm{bright,\ total}}(n) \right\} \right\}. \tag{4.22}$$

In practice, the atomic transition frequencies and detunings $\delta_{i,e}$ may not be well-defined, for example due to variation of the atomic Stark shift Δ_s. We can include this effect into our model by using a probability distribution of Stark shifts $\rho(\Delta_s)$. The resulting detection event distributions and the achievable fidelity $\mathcal{F}_{\mathrm{Stark}}$ are an integral over all possible distributions $p_{\mathrm{k,total}}(n)$ weighted with $\rho(\Delta_s)$ such that

$$\mathcal{F}_{\mathrm{Stark}} = \int_{-\infty}^{\infty} \rho(\Delta_s) \times \mathcal{F}(\Delta_s) d\Delta_s. \tag{4.23}$$

4.2.3 Simulation of fluorescence state detection

In this section, we use the model introduced above to analyze the hyperfine state readout of a single ^{87}Rb atom. We contrast the case of an atom coupled to a cavity with the case of an atom in free space. The fluorescence signal is therefore either collected in the cavity output mode or with a high numerical aperture (NA) objective. With regard to

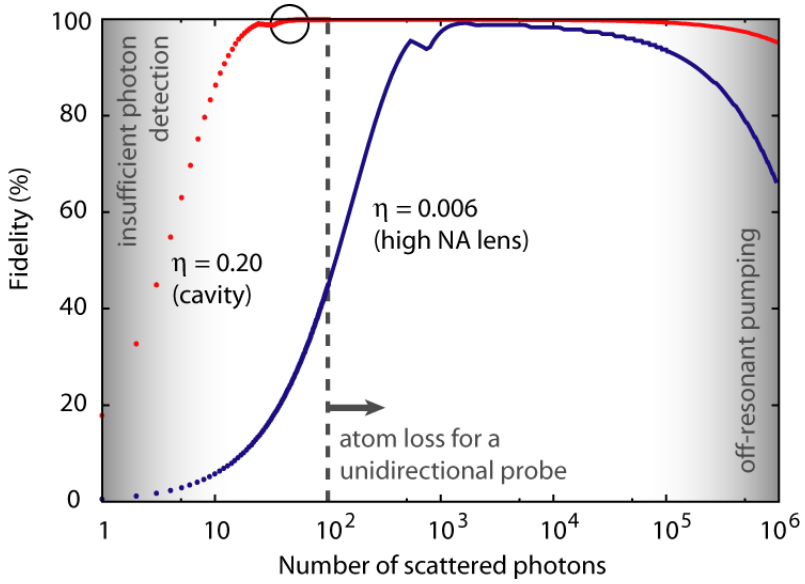

Figure 4.4: Fidelity in free space and with a cavity (fluorescence method). Calculated maximum fidelities for fluorescence state detection of a single ^{87}Rb atom with a cavity (η=20 %) and with a high numerical aperture (NA) objective (η=0.6 %), where η is the detection probability of a scattered photon. Fidelities are limited by an insufficient number of detected photons, optical pumping, and detector dark counts. Unidirectional probe light can expel the atom from an optical dipole trap after scattering $\approx$ 100 photons (dashed line) for a trap depth of 2 mK (see text for details). The novel regime of cavity-enhanced fluorescence readout introduced in this work is indicated by a black circle. A state detection fidelity of 99.98 % is feasible with less than 100 scattered photons.

atom loss and unwanted state pumping, the detection efficiency η will emerge as a crucial parameter. The detection efficiency is defined as the probability with which a scattered photon causes a "click" at the detector.

Ideally, a σ^+-polarized probe laser drives the $|F = 2, m_F = 2\rangle \leftrightarrow |F' = 3, m_{F'} = 3\rangle$ cycling transition such that off-resonant pumping into the dark hyperfine state is suppressed. In practice, such a unidirectional laser beam easily ejects the atom from an optical dipole trap before scattering a number[1] of photons sufficient to identify the atomic hyperfine state. For this reason, counter-propagating laser beams are advantageous to balance radiation pressure. Using a lin$\perp$lin polarization configuration avoids standing light wave effects. However, off-resonant excitation of the nearby $F' = 2$ state opens a decay channel

[1]Scattering of 100 photons from an unidirectional laser beam can be sufficient to expel a Rb atom from a 2 mK deep trap. This assumes all momentum transfer due to absorption is in one direction and corresponds to an atom with a slow periodic motion in the trap. In our example, this holds for a photon scattering rate on the order of 1 MHz and a trap frequency of less than 5 kHz along the propagation direction of the probe laser beam. However, for higher trap frequencies the periodic atomic motion randomizes the sign of momentum kicks caused by absorption. In this case, the atom is heated out of the trap due to a random walk in momentum space after scattering approximately 3000 photons. In a counterpropagating probe beam configuration, the number of scattered photons at which loss occurs is not well-defined as it depends on heating or cooling effects induced by the probe beam.

to the dark state. Therefore, high-fidelity state readout requires a sufficient number of fluorescence photons to be detected before pumping into the dark state occurs.

With a high numerical aperture objective the total photon detection efficiency is low. One of the best reported values in a single-atom setup is η=0.6 % [87]. This experiment used a specifically optimized lens system with a high NA = 0.7 resulting in a collection efficiency of spontaneously emitted photons of 15 %. However, the output of the objective is far from single-mode. Stray light suppression and difficult detector mode matching lead to an overall performance with small η. In this parameter range for free space fluorescence detection, the theoretically achievable fidelity is limited to 99.0 % and requires scattering of thousands of photons (Fig. 4.4).

However, η is dramatically increased with an optical cavity. The coupling of the atom to the cavity enhances the total fluorescence scattering rate and channels the photons into a well-defined cavity output mode. For the experiment described here, this causes about 60 % of all scattered photons to be emitted into the cavity mode resulting in a total detection probability of η=20 % per scattered photon. Moreover, the Purcell-enhancement of the fluorescence transition leads to a relative suppression of off-resonant decay paths and therefore reduces the effect of unwanted bright to dark state pumping. In our model, a remarkably high atomic state readout fidelity of 99.98 % can be achieved with less than 100 scattered photons. This novel regime of cavity-enhanced fluorescence state detection is indicated by a circle in figure (4.4). While operating at such low numbers of scattered photons minimizes the heating caused by state detection, it also enables high readout speeds.

The calculated achievable fidelities as a function of the average number of scattered photons N are shown for the two scenarios in (Fig. 4.4). At low numbers of scattered photons, the fidelity is limited by an insufficient number of detection events for the bright state. At high numbers of scattered photons the fidelity is limited by optical pumping. Dark counts reduce the fidelity for low and intermediate numbers of scattered photons. Non-monotonic behaviour of $\mathcal{F}(N)$ appears at shifts of the discrimination level d. For all regions where $\mathcal{F}(N)$ is rising, we find $C_{\mathrm{bright}} < C_{\mathrm{dark}}$. $\mathcal{F}(N)$ decreases in the small regions where $C_{\mathrm{bright}} > C_{\mathrm{dark}}$. This counterintuitive behaviour stems from our conservative definition of fidelity. Fidelities above 99% are reached for average scattered photon numbers of $N \geq 24$ (cavity case) and $N \geq 2700$ (free space). In these caluclations, we have used $s = 0.1$, $R_{dc} = 25\ s^{-1}$, $\Delta_a = \Delta_c = 0$ and assume equal populations of the available Zeeman-sublevels throughout the probe interval.

The high detection efficiency with a cavity can also enhance the speed of state readout. Calculations at probe power level $s = 1$ (at the validity limit of our model) suggest that state detection can be performed with a fidelity $\mathcal{F} > 99\,\%$ in a probe interval of $\tau_D = 10\,\mu$s for the parameters of our experimental setup.

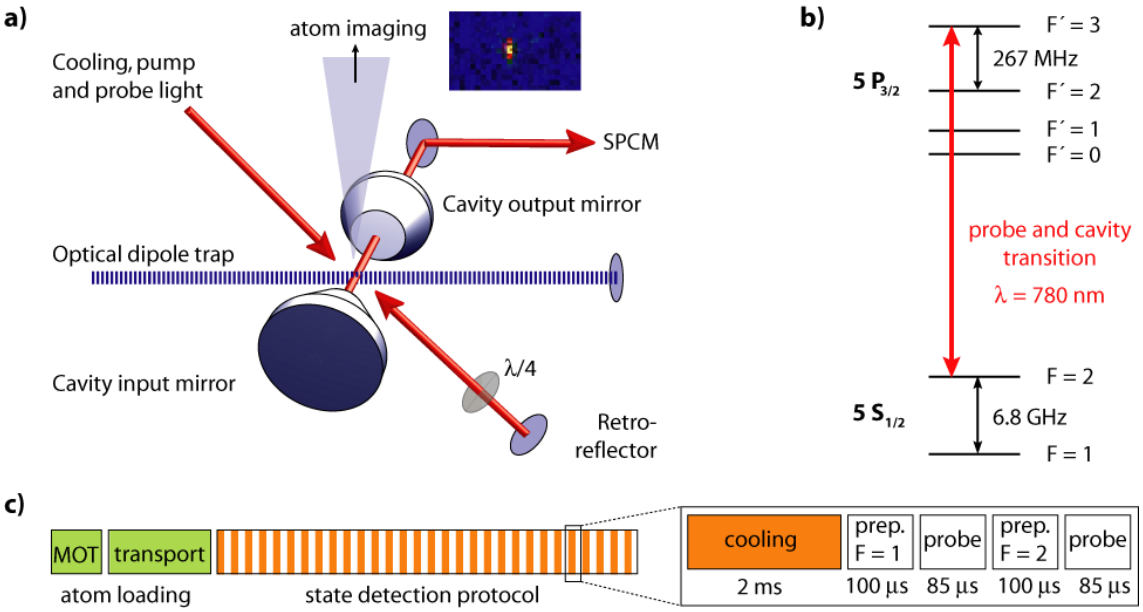

Figure 4.5: Experimental setup and protocol for cavity-enhanced fluorescence state detection. a) Experimental apparatus. A single ^{87}Rb atom is trapped in the cavity at the focus of the standing wave dipole-trap. A CCD camera system monitors the position of the atom (inset: CCD camera image of a single intracavity atom, image size 15 μm × 25 μm). For optical cooling and state preparation of the atom, laser beams near-resonant with the $5S_{1/2} \leftrightarrow 5P_{3/2}$ transitions are applied orthogonal to the cavity axis and retro-reflected with a lin⊥lin polarization ($\lambda/4$: quarter wave-plate). For atomic state detection, a probe laser resonant with the $F = 2 \leftrightarrow F' = 3$ transition is applied orthogonal to the cavity axis for cavity-enhanced fluorescence state detection. Photons emitted into the cavity output mode are detected by a single photon counting module (SPCM). **b)** Energy level diagram of the ^{87}Rb D2-transition, not to scale. **c)** Experimental protocol used for atomic state detection (see text).

4.2.4 Experimental results

In the experiment (Fig. 4.5), a single ^{87}Rb atom is trapped at the focus of the standing-wave dipole trap in the center of the cavity mode. To characterize cavity-enhanced fluorescence state detection, we repeatedly apply a protocol of optical cooling, atomic state preparation and atomic state readout at a rate of 400 Hz. The atom is first cooled (2 ms), alternately prepared in the $F = 1$ or $F = 2$ hyperfine ground state by optical pumping (100 μs) and finally probed during a state-detection interval (85 μs). We set the cavity and probe laser frequencies equal ($\Delta_c = 0$) and red-detuned from the $F = 2 \leftrightarrow F' = 3$ atomic resonance by $\Delta_a/2\pi = 30$ MHz, where Δ_a refers to the detuning between probe laser and the maximally Stark-shifted atomic transition. The detuning is chosen to avoid probe-light induced heating of the atom. The probe laser is applied orthogonal to the cavity axis and retro-reflected in a lin⊥lin polarization configuration with a power of 40 nW and a beam waist radius of $\approx 50\,\mu$m. With the CCD-camera system we determine the position of single atoms trapped in the cavity by collecting light scattered during optical cooling of the atoms. For the data presented here, we trap exactly one atom in the center ($\pm 10\,\mu$m) of the cavity mode.

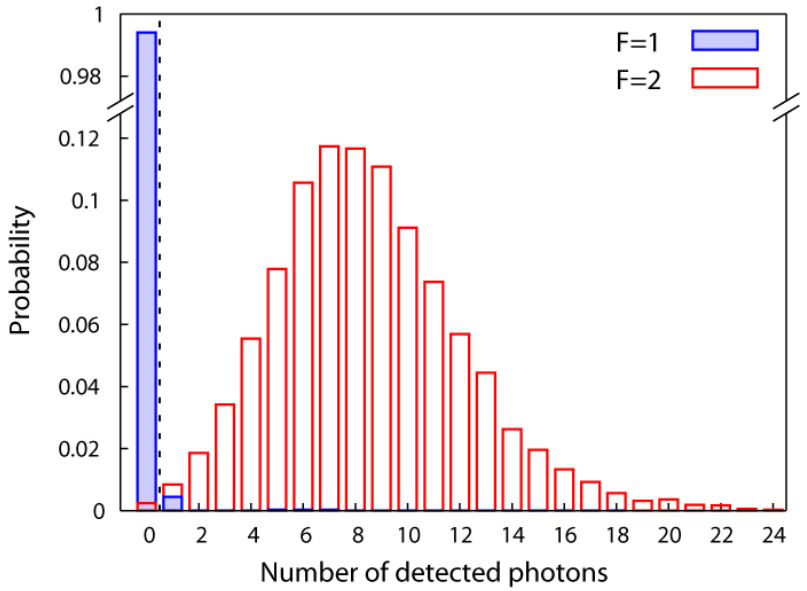

Figure 4.6: Cavity-enhanced fluorescence state detection. Measured probability distributions of the number of detected photons N per probe interval with the atom either prepared in the $F = 2$ (red histogram) or in the $F = 1$ hyperfine ground state (blue histogram). The atom is illuminated with a 85 μs pulse of probe light orthogonal to the cavity axis and near-resonant with the $5S_{1/2}$ $F = 2 \leftrightarrow 5P_{3/2}$ $F' = 3$ transition. Identifying probe intervals with $N = 0$ as the $F = 1$ state and intervals with $N \geq 1$ as the $F = 2$ state (dashed discrimination line) results in a hyperfine state detection fidelity of 99.4±0.1% (uncertainty is statistical) mainly limited by detector dark counts and state preparation errors (contribution to infidelity 0.4% and 0.1%, respectively). The bright state photon number distribution is nearly Poissonian, but broadened due to uncertainties in atomic position and Stark shift (Mandel Q parameter Q=0.5).

Analyzing the number of detected fluorescence photons N during each probe interval, we find a clear distinction between the dark $F = 1$ and the bright $F = 2$ hyperfine state (Fig. 4.6). The presented histograms are based on 23200 state readout attempts of 29 single atoms, corresponding to 800 attempts per atom. This means that the hyperfine state of each atom was interrogated 800 times without loss of the atom. Identifying probe intervals with $N = 0$ as the $F = 1$ state and intervals with $N \geq 1$ as the $F = 2$ state results in a hyperfine state detection fidelity of 99.4±0.1 % (uncertainty is statistical). The measured fidelity is close to the theoretically achievable 99.6 % for the experimental parameters. The measured fidelity is limited by state preparation errors (contribution to infidelity $\approx$0.1 %) as well as detector dark counts (contribution to infidelity $\approx$0.5 %).

The readout fidelities for dark and bright state evaluated separately are $\mathcal{F}_{\text{dark}} = 99.4\,\%$ and $\mathcal{F}_{\text{bright}} = 99.8\,\%$. We conclude that the total fidelity is limited by failure of identifying the dark state as dark. The dark state infidelity of 0.6 % is dominated by "one-click" events ($p_{\text{dark}}(1) = 0.5\,\%$, while $p_{\text{dark}}(n \geq 2) = 0.1\,\%$). The occurence of intervals with one registered click $n = 1$ is consistent with a measured total dark count rate of the detector of approximately $R_{dc} \approx 55$ Hz causing a false click with 0.5 % probability within the 85 μs gate interval. Readout intervals with more than one registered detector click are supposedly caused by failure of dark state preparation as the expected dark to bright

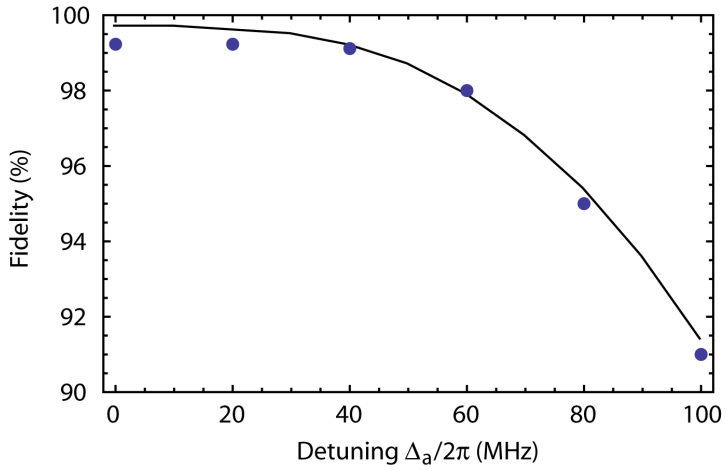

Figure 4.7: The cavity-enhanced fluorescence scheme is robust against detuning. Measured fidelity (dots) as a function of atomic detuning for hyperfine state detection by cavity-enhanced fluorescence. The probe laser power is adjusted such that for every value of the detuning the average number of detected photons is $\bar{N} = 8$. The fidelity proves robust against atomic detuning. At small detunings $\Delta_a/2\pi \leq 40\,\mathrm{MHz}$, the measured fidelity is limited by dark counts and state preparation errors, at larger detunings it is limited by bright-to-dark state pumping. Solid line: Calculated fidelity for on average $\bar{N} = 8$ detected photons for an atom in the bright state and an assumed atomic Stark shift distribution as measured in section (4.5).

pumping probability is exceedingly small ($\alpha_{dark} \approx 10^{-7}$). The measured bright state infidelity of 0.2 % is larger than the expected effect of bright to dark pumping (0.06%) as well as the 0.03 % probability of detecting 0 clicks in a Poissonian distribution with a mean of 8 clicks. We therefore attribute the measured infidelity to failure of state preparation and to a non-Poissonian distribution of the detection events (Mandel Q parameter Q=0.5) due to residual atomic motion (g-averaging, Stark shift sampling).

Next, we investigate the dependence of the state readout fidelity on atomic detuning (Fig. 4.7). This is important because neutral atoms are usually trapped in optical dipole potentials and may experience significant AC-Stark shift variations. We mimic this effect by keeping the probe laser and cavity resonant ($\Delta_c = 0$) and by detuning them from the Stark-shifted atomic resonance (probe-atom detuning $\Delta_a/2\pi = 0...100\,\mathrm{MHz}$). We note that the atom experiences position-dependent Stark shifts in the dipole trap and the detuning we apply here is additionally superimposed. The probe laser power is increased with Δ_a such that the mean photon number detected from the bright state is kept constant ($\lambda_{\mathrm{bright}} \approx 8$). Fidelities on the order of 99% are maintained up to 40 MHz detuning, decreasing to 91% at $\Delta_a/2\pi = 100\,\mathrm{MHz}$ due to off-resonant excitation of the $F' = 2$ state as Δ_a approaches the excited state hyperfine splitting ($\omega_{HFP}/2\pi = 267\,\mathrm{MHz}$). The observed robustness of cavity-enhanced fluorescence readout is confirmed by our statistical model (Fig. 4.7). Conceptually, the fidelities remain high because the detection rate of fluorescence photons is large compared to the hyperfine pumping rate. Additionally, the cavity favours the $F' = 3$ to $F = 2$ decay path and thereby lowers the probability of bright-to-dark state pumping.

4.3 State detection by differential transmission

4.3.1 Transmission of the atom-cavity system

The internal state-dependent response of an atom to a light field naturally opens two avenues for optical state readout: fluorescence light detection (as discussed above) and differential transmission of a probe beam. In free space, differential transmission shows minute effects for a single atom and is difficult to detect at all [123]. The effect can be enhanced by an optical cavity, where the presence of a single atom can drastically change the transmission [110, 109, 124, 48]. Differential transmission measurements are closely linked to normal-mode spectroscopy of the coupled atom-cavity system. A high differential transmission contrast therefore requires the strong-coupling regime of cavity quantum electrodynamics. Here, we briefly introduce the necessary parameters which affect the contrast.

The steady-state intracavity photon number N_{cav} of a coupled atom-cavity system driven along the cavity axis at a rate η_c by a probe laser is given by

$$N_{cav} = \frac{|\eta_c|^2}{\Delta_c^2 + \kappa^2} \frac{1}{|1-\nu|^2}\,. \tag{4.24}$$

We recall the complex cooperativity $\nu = g^2/\left((\Delta_a - i\gamma)\,(\Delta_c - i\kappa)\right)$, with the detuning of atom Δ_a and cavity Δ_c with respect to the probe laser . Equation (4.24) is valid in the limit of weak driving (low saturation of the atom, [92]). The atomic state dependence of the transmission is incorporated in (4.24) via the atom-probe laser detuning Δ_a.

In the following, we choose probe laser and cavity resonant ($\Delta_c = 0$) and approximately resonant with the Stark-shifted atomic $F = 2 \leftrightarrow F' = 3$ transition. With the atom prepared in the $F = 1$ state, the atom is effectively detuned from cavity and probe laser by about the ground state hyperfine splitting $\Delta_a \approx \omega_{HFS} \approx 6.8\,\mathrm{GHz}$. Hence, the effective cooperativity vanishes ($\Delta_a \gg (\kappa, \gamma, g)$) and the transmission remains at the empty cavity (no atom) value. With the atom prepared in the $F = 2$ state, cavity and atom are resonant ($\Delta_a \approx 0$) and the intracavity photon number reduces according to equation (4.24). The differential transmission ratio for an atom prepared in either $F = 2$ or $F = 1$ is thus given by:

$$T = \frac{T_2}{T_1} = \frac{N_{\mathrm{cav},2}}{N_{\mathrm{cav},1}} \cong \frac{1}{|1-\nu|^2}. \tag{4.25}$$

The expected transmission of the coupled atom-cavity system (Eq. 4.25) is shown in figure (4.8) for different values of g while assuming $\Delta_a = \Delta_c = 0$. In our setup, a single maximally coupled atom ($g_{\max}/2\pi = 7.9\,\mathrm{MHz}$) can reduce the transmitted intensity to T=1.5 %. With an effective coupling of $g/2\pi = 3.0\,\mathrm{MHz}$ due to spatial and polarization averaging, we can expect a transmission of $T = 24\,\%$. This reduction would be sufficient to discriminate the atomic hyperfine states with a fidelity of 99 % at a probe level of on average 20 detected photons per readout interval for an atom in $F = 1$.

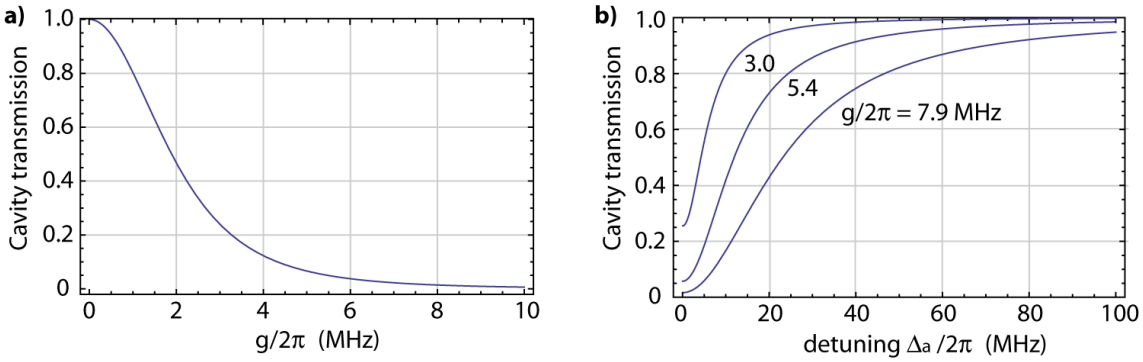

Figure 4.8: Cavity transmission. The transmission of the atom-cavity system depends on the coupling strength g and the atomic detuning Δ_a. Probe laser and cavity are assumed to be resonant ($\Delta_c = 0$). **a)** Relative transmission as a function of coupling constant g for $(\kappa, \gamma, \Delta_a)/2\pi = (2.8, 3.0, 0)\,\mathrm{MHz}$. **b)** Relative transmission as a function of atomic detuning Δ_a for the cases of $g = 7.9\,\mathrm{MHz}$, $g = 5.4\,\mathrm{MHz}$ and $g = 3.0\,\mathrm{MHz}$.

4.3.2 Experimental results

The experimental sequence for atomic state detection by differential cavity transmission is equivalent to the fluorescence measurement. A single atom centrally trapped inside the cavity mode is repeatedly cooled (9 ms), prepared in $F = 1$ or $F = 2$ (100 μs) and probed by a cavity transmission measurement (300 μs). However, the transmission contrast for a single atom has proven very sensitive to AC-Stark shifts. Therefore, we reduce the dipole trap depth from 3 mK to 0.6 mK during the transmission probe interval to minimize the Stark shift and concomitant variations in Δ_a. The cavity and probe laser frequencies are set equal ($\Delta_c = 0$) and resonant with the Stark shifted atomic $F = 2 \leftrightarrow F' = 3$ transition. The probe laser is applied along the cavity axis for 300 μs and is σ^+-polarized such that it in principle drives the $|F = 2, m_F = 2\rangle \leftrightarrow |F' = 3, m_{F'} = 3\rangle$ cycling transition. A magnetic field of ≈ 250 mG is applied along the cavity axis to provide a quantization axis. However, tests at different probe polarizations have revealed uncompensated off-axis magnetic fields. We can therefore not exclusively address the transition $|F = 2, m_F = 2\rangle \leftrightarrow |F' = 3, m_{F'} = 3\rangle$ leading to Clebsch-Gordan averaging of g.

We analyze the number of photons detected during each transmission probe interval and obtain two well separated probability distributions corresponding to atom preparation in the two hyperfine states (Fig. 4.9). The presented data is based on 75 separately trapped single atoms subject to 240 readout attempts. With the atom prepared in the $F = 1$ state, the cavity transmission is virtually unaffected by the presence of the atom and remains at $T = 100\,\%$. With the atom prepared in the $F = 2$ state, the measured transmission reduces to approximately 40 %. From the data we deduce a readout fidelity of $99.0 \pm 0.5\,\%$ for a single 300 μs probe interval (quoted error is statistical).

The measured attenuation of the probe beam by a single atom to 40 % is less than expected from theory (24 % for $g/2\pi = 3.0\,\mathrm{MHz}$). We attribute this discrepancy to remaining Stark shift variations of the probe transition on the order of $\approx 10\,\mathrm{MHz}$ and a detailed

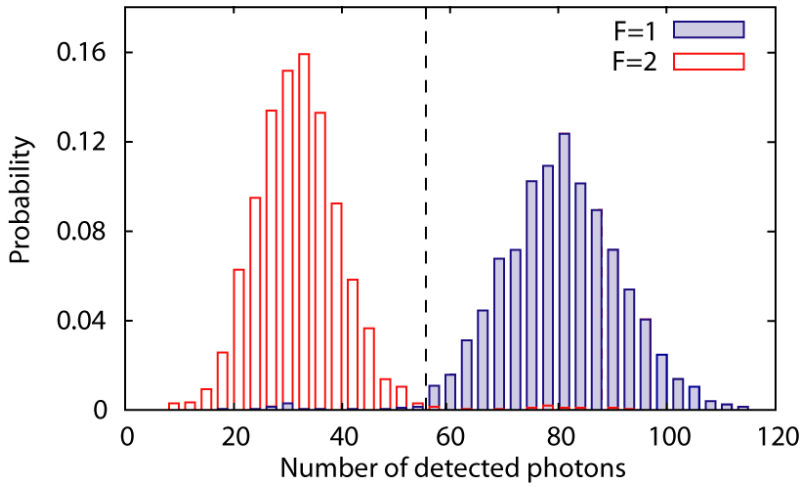

Figure 4.9: Atomic hyperfine state readout by differential cavity transmission yields a fidelity of $99.0 \pm 0.5\,\%$. The histograms show the probability distributions of photon detection events for atoms prepared in $F = 2$ (red) and $F = 1$ (blue). The average transmission values are $\lambda_{|2\rangle} = 32$ and $\lambda_{|1\rangle} = 79$ resulting in $T = 40\,\%$. The discrimination level is set to $d = 55$ detection events, such that an atom is identified as being in $F = 2$ for $n \leq 55$ and in $F = 1$ for $n > 55$.

investigation is given below. For the measured average values of $\lambda_{|2\rangle} = 32$ and $\lambda_{|1\rangle} = 79$ detected photons, two ideal Poissonian distributions would overlap by only 0.07% and would allow a fidelity of 99.9 %. The measured fidelity of 99.0±0.5% is lower due to failure of state preparation (estimated 0.6 %) and due to the non-Poissonian shape of the detected probability distributions (reduction of fidelity 0.4 %). These deviations are explainable by a time-varying Stark shift (atomic motion, intensity ramp down of dipole trap) and technical limitations such as cavity lock stability and drift of the probe laser power (estimated transmitted intensity variations $\approx 5\,\%$).

By increasing the duration of the probe interval or the intensity of the probe laser, the overlap of the two probability distributions could theoretically be reduced. However, the number of detected photons per probe interval is in practice limited by atom loss. From extensive test measurements (probe power, probe duration, probe polarization, detunings), the paramter range with probe intervals of a few hundred microseconds, low absolute Stark shift and minimized atom-cavity detuning emerged as an optimum for short detection time, high fidelity and tolerable atom heating. In this regime, a sufficient number of detected photons requires a sufficiently high probe intensity, which is ultimately limited by the onset of saturation of the atom-cavity system and by atom loss due to heating. The effect of unwanted state-pumping during probing is negligible as has been verified by time-resolved evaluation of probe intervals.

We find evidence for the crucial role of Δ_a by deliberately detuning probe laser and cavity from the Stark-shifted atomic transition. We keep cavity and probe laser frequencies equal ($\Delta_c = 0$) and shift them to realize different values of Δ_a. The measured contrast and hence the fidelity reduces dramatically when the atomic detuning is increased to $\Delta_a/2\pi = 20$ MHz and $\Delta_a/2\pi = 40$ MHz (Fig. 4.10).

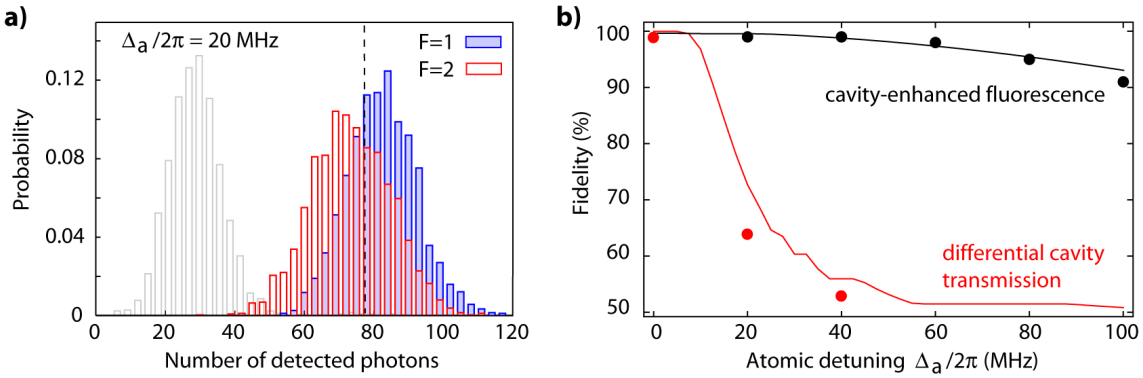

Figure 4.10: Fidelity as a function detuning for differential transmission. **a)** The transmission contrast decreases as the atom-cavity detuning is increased to $\Delta_a/2\pi = 20\,\mathrm{MHz}$ (gray histogram: resonant case, shown for comparison). **b)** Measured fidelity (dots) as a function of detuning for differential cavity transmission and for cavity-enhanced fluorescence. Solid lines: Theoretical model.

Even on resonance ($\Delta_a = 0$), the measured average transmission reduction of 60 % by a single trapped atom is far from the maximum achievable 98.5 % at $g_{\max}/2\pi = 7.9\,\mathrm{MHz}$. How much transmission contrast can in principle be gained is demonstrated with a different dipole trap configuration. We use the transport dipole trap as a shallow potential in which the atoms probabilistically drift through the cavity mode (maximum Stark shift at the cavity $\Delta_s/2\pi = 3$ MHz). The density of the atomic cloud passing through the cavity is chosen low enough such that two-atom events are negligible. Typical examples of the observed transmission dips of cavity probe light caused by single atoms are shown in figure (4.11). Depending on the individual trajectories, atoms may fly through a cavity field node or anti-node. The transmission for single maximally coupled atoms is found to be as low as 5%. Applied to atomic state readout via differential cavity transmission this contrast could enable high fidelities with few detected photons. However, to achieve this contrast with a permanently trapped atom, the atom would need to be cold (Stark shift variations $\Delta_s \leq \gamma$) and localized at a cavity field maximum [111].

4.4 Comparison and discussion of the results

The internal state-dependent response of an atom to a light field naturally opens two avenues for atomic state readout: fluorescence light detection and differential transmission of a probe beam. Both methods benefit from enhanced light-matter interaction in an optical cavity. In our setup, we have achieved hyperfine state detection fidelities of 99 % with both techniques for a single trapped ^{87}Rb atom. The performed protocols give a result in every readout attempt and no post-selection is required. Most important, the readout does not cause loss of the atom. We have thus demonstrated an efficient realization of diVincenzo's requirement for qubit readout [31] in neutral atoms. Further, the elimination of atom-loss at detection establishes neutral atoms as truly stationary carriers of quantum information.

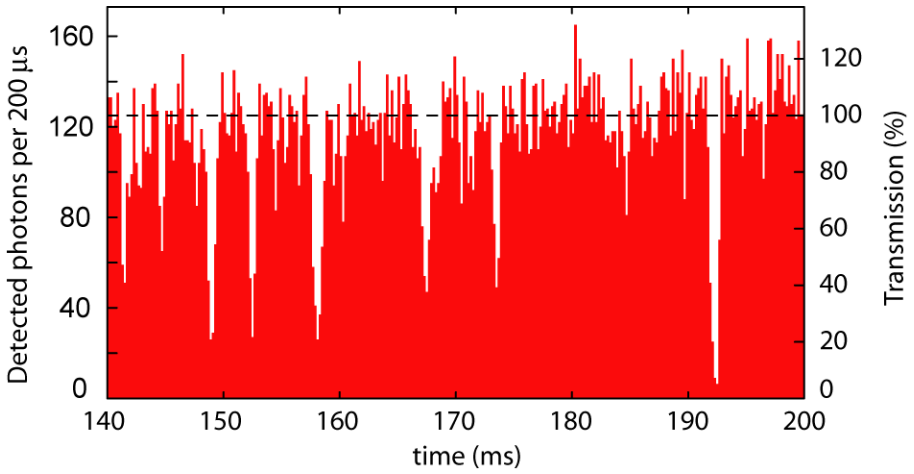

Figure 4.11: Transit of single atoms through the cavity. In a shallow transport dipole trap, the atoms experience only small Stark shifts and probabilistically drift through the cavity mode. Some trajectories cross a maximum of the cavity mode and atoms couple strongly to the cavity resulting in a reduction of the transmitted probe light (histogram bars). Single optimally coupled atoms can reduce the transmission to $T/T_0 \simeq 5\%$.

As a first method, a cavity-enhanced fluorescence detection scheme has been introduced. From statistical analysis, the detection efficiency η emerges as a crucial parameter. In our setup, a remarkably high $\eta = 20\,\%$ enables hyperfine state detection with a fidelity of $99.4\,\%$ in $85\,\mu$s. The achievable fidelity is mainly limited by dark counts. Cavity-enhanced fluorescence proves robust against atomic detuning allowing operation in deep optical dipole traps. It does not require the strong-coupling regime of cavity quantum electrodynamics which simplifies technical implementation. In the presence of unwanted decay channels (i.e. state pumping during probing), the Purcell effect supports a preferential decay path and establishes an efficient coupling to the detector. The combination of high fidelity, experimental robustness and readout speeds which are fast compared to hyperfine qubit decoherence times [72] makes cavity-enhanced fluorescence a useful tool for quantum protocols based on neutral atoms [73, 75, 74]. Finally, this scheme is applicable to other physical systems with optically accessible qubits such as quantum dots, NV centers in diamond or cold molecules.

The second readout method studied in this chapter is based on cavity transmission. We found that the differential transmission contrast critically depends on variations of the atomic Stark shift and the coupling g. For a cavity operating in the intermediate coupling regime, the transmission method appears to be less suitable than the fluorescence technique. In comparison, the cavity-enhanced fluorescence technique achieves higher fidelities over a large range of detunings while operating at higher readout speeds. Moreover, the required cavity parameters (moderate size and coupling, moderate linewidth) are generally easier to implement.

In future experiments, cavity-enhanced fluorescence readout may be achieved within a few microseconds. Operating at higher probe power, a fidelity $\mathcal{F} \geq 99\%$ within a probe interval of $10\,\mu s$ is expected. With an adaptive technique [122], the average readout time

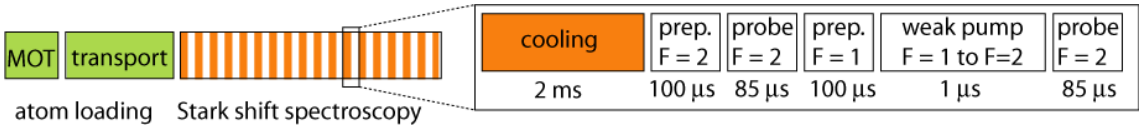

Figure 4.12: Sequence for Stark shift spectroscopy. First, a reference signal level is generated by preparing atoms in $F = 2$ and probing with a $|5^2S_{1/2}\, F = 2\rangle \leftrightarrow |5^2P_{3/2}\, F' = 3\rangle$ resonant laser. Next, the atoms are prepared in $F = 1$ and a weak pump laser of variable frequency partially transfers atoms into $F = 2$. The final population in $F = 2$ is probed again. By comparison of this signal with the reference, we determine the transfer efficiency as a function of pump laser frequency which corresponds to a Stark shift spectrum. The total repetition rate is 400 Hz.

may be further reduced: In our data, the first photon detection event is sufficient to identify the atomic state. All additional information aquired during the same probe interval is redundant. Using the existing capabilities for deterministic atom transport in optical dipole traps [77, 70, 125], a cavity may serve as a readout head into and out of which neutral atom qubit registers are shifted. Lossless atomic state detection can also improve the performance of atomic clocks [126]. The two schemes outlined here discriminate atomic hyperfine states but can be extended to the detection of Zeeman states. This is relevant for applications in atom-photon and atom-atom entanglement experiments. In this respect, hyperfine state detection should be complemented by hyperfine qubit rotations and capabilities for mapping a Zeeman qubit onto the hyperfine qubit. Both rotation and mapping are standard techniques and have been demonstrated in other experiments by use of microwaves or Raman laser pairs [113, 115].

4.5 Applications of cavity-enhanced fluorescence

4.5.1 Stark shift spectroscopy

Hyperfine state detection can be used for Stark shift spectroscopy of the atom-cavity system. The basic concept is to measure the Stark shift-dependent efficiency of optical pumping between the states $F = 1$ and $F = 2$. The experimental protocol for Stark shift spectroscopy involves three sequential steps. In a first step, the atoms are prepared in $F = 1$. Next, a weak pump laser beam is applied coupling $F = 1$ and $F' = 2$ which can optically pump atoms from $F = 1$ to $F = 2$. The efficiency of this state transfer is highest when the laser is resonant with the actual Stark-shifted $F = 1$ to $F' = 2$ transition. In a third step, the final population of state $F = 2$ is measured via cavity-enhanced fluorescence. We repeatedly apply this protocol and determine the transfer efficiency as a function of the pump laser frequency.

In practice, the experimental sequence is complemented by a reference measurement with atoms directly prepared in $F = 2$. This allows to remove systematic drifts in the signal level and to work with many atoms loaded into the cavity which improves the data aquisition rate. A typical protocol used for Stark shift spectroscopy is depicted in figure (4.12). In general, the area of the optical pump pulse must be chosen low enough to avoid high

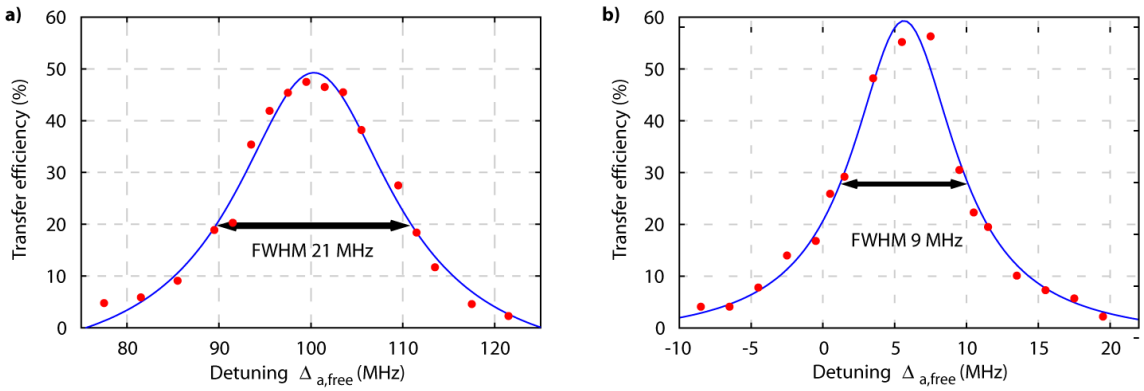

Figure 4.13: Stark shift spectroscopy. Graphs **a)** and **b)** show the hyperfine state transfer efficiency as a function of the $F = 1$ to $F' = 2$ pump laser frequency for high and low power of the dipole trap laser: **a)** standing wave trap at 2.5 W, **b)** transport trap at 4 W. The transfer is most efficient when the weak pump laser is resonant with the Stark-shifted atomic transition. From numerical fits (solid lines), we obtain Stark shift distributions centered at $\Delta_s/2\pi = 100$ MHz for a) and $\Delta_s/2\pi = 6$ MHz for b) and a full width at half maximum of 21 MHz and 9 MHz, respectively.

transfer efficiencies on resonance as this would distort the obtained Stark shift spectra.

As an example, measurements of the transfer efficiencies as a function of pump laser frequency are shown in figure (4.13) for two settings of the optical dipole trap. The first setting (standing wave trap, $P = 2.5$ W) represents the standard atom trapping condition of our experiment. We find a near-Lorentzian distribution with a width of 21 MHz centered at $\Delta_s/2\pi = 100$ MHz. This agrees well with the predicted Stark shift of 100 to 125 MHz (uncertainty due to laser beam alignment) and indicates the finite temperature of the atoms. For the transport trap (running wave, $P = 4$ W) with weak dipole potential in the cavity region, we find the atomic center frequency at $\Delta_s/2\pi = 6$ MHz and a width of approximately 9 MHz.

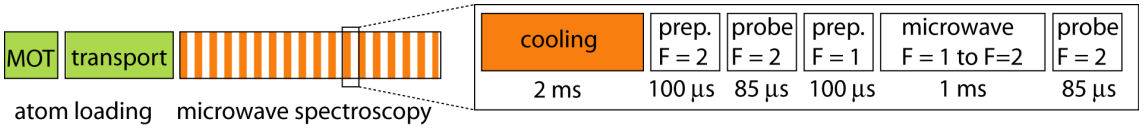

Figure 4.14: Sequence for microwave spectroscopy. A microwave pulse of variable frequency is applied to atoms prepared in $F = 1$ and partially transfers atoms into $F = 2$. The population in $F = 2$ is probed to determine the transfer efficiency as a function of microwave frequency. A signal derived from atoms directly prepared in $F = 2$ serves as a reference level.

4.5.2 Measurement of the magnetic field

Knowledge and control of the magnetic field at the position of the atom is essential for full control over the atom-cavity system. The influence of the magnetic field is especially relevant for entanglement experiments employing the atomic Zeeman states. Non-zero or fluctuating magnetic field components are a major source of decoherence [127, 72]. Here, we use cavity-enhanced fluorescence state detection in combination with microwave fields for a direct measurement of the magnetic field at the position of the atom.

The experimental protocol is equivalent to the Stark shift spectroscopy outlined above. However, the optical pumping via the atomic excited states is replaced by direct state transfer between $F = 1$ and $F = 2$ using microwave radiation. The ground state population transfer is monitored as a function of microwave frequency in order to identify transitions between the Zeeman sublevels. Once these Zeeman state resonances can be measured, the absolute magnetic field at the position of the atom is known and can be minimized by applying counteracting fields using the external Helmholtz compensation coils.

Quantitatively, a magnetic field $\vec{B}$ lifts the degeneracy of the Zeeman sublevels with quantum number m_F and shifts their energy by

$$\Delta E_{|Fm_F\rangle} = \mu_B \cdot g_F \cdot m_F \cdot B \tag{4.26}$$

where μ_B denotes the Bohr Magneton, B is the absolute value of the magnetic field, and g_F is the Landé factor of the atomic hyperfine state. For the hyperfine states $5^2\mathrm{S}_{1/2}\, F = 1$ and $5^2\mathrm{S}_{1/2}\, F = 2$ of ^{87}Rb the effective shifts are:

$$\begin{aligned} 5^2\mathrm{S}_{1/2}\, F = 1: &\quad \Delta E_{|1m_1\rangle} = -B \cdot m_1 \cdot 0.7\ \mathrm{MHz/\ G} \quad m_1 \in \{-1, \ldots, +1\} \\ 5^2\mathrm{S}_{1/2}\, F = 2: &\quad \Delta E_{|2m_2\rangle} = B \cdot m_2 \cdot 0.7\ \mathrm{MHz/\ G} \quad m_2 \in \{-2, \ldots, +2\} \end{aligned} \tag{4.27}$$

The microwave (magnetic dipole) transition frequencies depend on the absolute value of the magnetic field as:

$$\omega_n = 6.834683\ \mathrm{GHz} + B \cdot n \cdot 0.7\ \ \mathrm{MHz/\ G} \qquad n \in \{-3, \ldots, +3\} \tag{4.28}$$

The microwave radiation is applied with a microwave horn mounted above the vacuum system and pointing towards the cavity assembly at a distance of approx. 10 cm. The

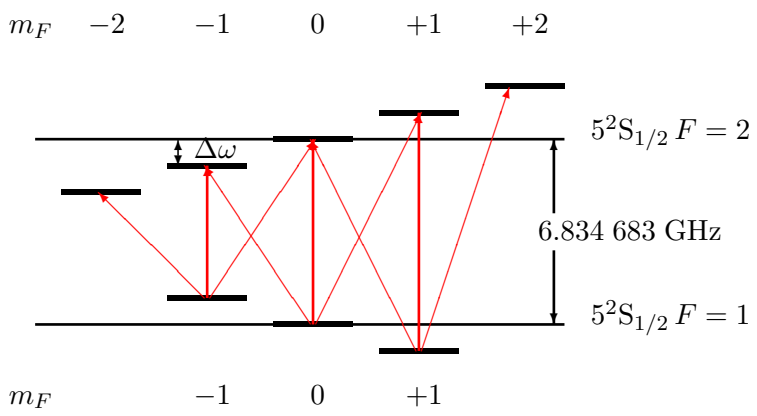

Figure 4.15: Microwave transition scheme. Arrows indicate microwave transitions between magnetic sublevels of the hyperfine states $5^2S_{1/2}\,F=1$ and $5^2S_{1/2}\,F=2$ of ^{87}Rb. A non-zero magnetic field lifts the degeneracy of the Zeeman states with quantum number m_F. The energy of levels with $m_F=0$ remains unaffected.

horn can be adjusted to emit all microwave polarizations. As a microwave source, we use a high-frequency function generator. Its cw-output is switched and amplified (final output power 32 dBm). To our disadvantage, the piezo tube stabilizing the cavity length is plated and shields the microwaves from the intracavity region. Only the mm-size holes in the piezo permit an evanescent microwave field to leak into the cavity volume. In the experiment, we find that the microwave field at the location of the atom is too weak to observe coherent Rabi oscillations of the hyperfine state populations. Yet the signal is sufficient for microwave spectroscopy. The fact that the piezo partially absorbs microwave power is substantiated by the microwave-induced thermal drifts of the cavity length.

In a first test measurement, we disable the external magnetic field compensation coils and observe the Zeeman splitting caused by the background magnetic field (figure 4.16) [2]. The average frequency difference of the microwave resonances is $\Delta\omega/2\pi = 456$ kHz corresponding to a background magnetic field of $B \simeq 651\,\mathrm{mG}$. The resonance frequencies and widths of the microwave resonances as deduced from individual Lorentz fits are summarized in the following table.

Resonance	−3.	−2.	−1.	−0.	+1.	+2.	+3.
FWHM (kHz)	36	21	12	4	12	27	44
Peak Pos.(kHz)	−1365	−908	−455	0	455	910	1369

We notice that the peak width grows linearly with detuning from the $|F=1, m_F=0\rangle \leftrightarrow |F=2, m_F=0\rangle$ transition. This points at a fluctuating absolute value of the magnetic field. The length of the microwave pulses of 1 ms corresponds to 1 kHz in the frequency domain – the observed peak width is therefore not Fourier-limited.

[2] In central Europe the earth's magnetic field components in horizontal and vertical direction are $B_{\mathrm{hor,vert}} \simeq (0.2; 0.4)\,\mathrm{G}$.

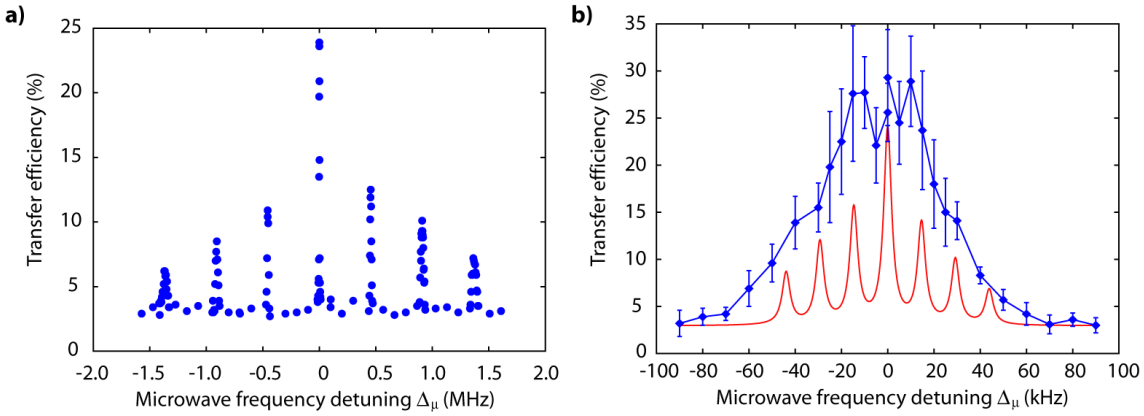

Figure 4.16: Magnetic field optimization. **a)** Measured microwave spectrum of the $|5^2S_{1/2}\, F = 1\rangle \leftrightarrow |5^2S_{1/2}\, F = 2\rangle$ transition with compensation field coils turned off (blue dots). The microwave detuning Δ_μ is given with respect to the $|5^2S_{1/2}\, F = 1, m_1 = 0\rangle \leftrightarrow |5^2S_{1/2}\, F = 2, m_2 = 0\rangle$ transition at 6.834683 GHz. The resonances at which hyperfine state transfer occurs are separated by $\Delta\omega = 456\,\text{kHz}$ corresponding to a background magnetic field of $B \simeq 651\,\text{mG}$. **b)** Measured microwave spectrum (blue curve) with the background magnetic field compensated by 3 pairs of external Helmholtz coils. The microwave resonances have merged and the residual magnetic field is estimated to be $B = (24 \pm 7)\,\text{mG}$. A corresponding theoretical spectrum is shown for comparison using a linewidth of 4 kHz (red curve). The measured spectrum is considerably blurred – probably due to temporal fluctuations of the magnetic field during the measurement.

In a second experiment, we reduce the magnetic field at the location of the atom by applying compensation fields using three pairs of Helmholtz coils surrounding the vacuum system. Our goal is to merge all microwave resonances at the value of the $|5^2S_{1/2}\, F = 1, m_1 = 0\rangle \leftrightarrow |5^2S_{1/2}\, F = 2, m_2 = 0\rangle$ transition. We finally obtain a microwave spectrum as depicted in figure (4.16). We estimate the remaining magnetic field by assuming an underlying spectrum with an average peak separation of $\Delta\omega/2\pi \simeq (17 \pm 5)$ kHz corresponding to an absolute magnetic field value of $B = (24 \pm 7)\,\text{mG}$. However, the observed blurred spectrum is most certainly caused by temporal fluctuations of the magnetic field. A further reduction of the absolute magnetic field and its temporal fluctuations requires considerable technical effort. The passive stability can be improved by removing laboratory equipment causing fluctuating stray fields or by proper magnetic shielding. An active stabilization scheme involves precise monitoring of the magnetic field on all relevant time scales (sub-millisecond to days) with a precision of $\approx 1\,\text{mG}$ in the vicinity of the atom. The measured values would serve as an input for electronic feedback onto the compensation field coils. It has been shown in [72] that these techniques can reduce magnetic field fluctuations to less than 2 mG corresponding to atomic Zeeman state coherence times of 150 μs.

5 EIT with single atoms in a cavity

This chapter gives a brief summary of experiments in which we observe electromagnetically induced transparency (EIT) with single trapped atoms in the cavity.

The content of this chapter has partially been published in:
"Electromagnetically induced transparency with single atoms in a cavity",
M. Mücke, E. Figueroa, J. Bochmann, C. Hahn, K. Murr, S. Ritter, C. J. Villas-Boas, and G. Rempe, *Nature* **465**, 755 (2010).

5.1 EIT: Controlling light with light

Electromagnetically induced transparency (EIT) allows the coherent control of the transmission of a probe beam through an optically dense medium [128, 129]. The physical concept behind EIT is the creation of a coherent dark state when a three-level medium is driven by two coherent fields. Typically, EIT is observed in atomic ensembles (alkali vapour cells at room temperature) employing a Λ-type level scheme. In this scheme, two hyperfine ground states are coupled to one common excited state by two laser beams (equivalent to Fig. 5.1c). One of the laser beams is used to probe the transmission of the medium, while the second beam can coherently control the optical properties of the medium. The atomic system driven by the laser fields is appropriately described in a basis of new eigenstates which are superpositions of the uncoupled atomic states. Remarkably, when the two laser fields are Raman resonant, one of these eigenstates is a superposition of the two atomic ground states and does not contain the atomic excited state. Atoms in this "dark" state do not interact with light and become transparent for the probe beam. Therefore the transmission spectrum of the atomic medium exhibits a characteristic transparency feature at the probe beam frequency for which the Raman resonance condition is fulfilled. The width, height and absolute frequency of the EIT transmission window is adjustable via the frequency and strength of the control laser field. In this sense, the optical properties of the medium can be externally controlled.

The phenomenon of EIT has a multitude of interesting aspects. A prime example is the observation of slow light [130, 131], while in other experiments, the EIT scheme has been extended to the storage and controlled read-out of light pulses [132, 133, 134, 135]. Naturally, EIT provides a tool to switch light with light [136] and the inclusion of additional atomic states and field modes can result in complex behaviour of light fields inside a medium [129, 137].

An exciting prospect which we will follow in this chapter is the scaling of EIT into the regime of a few atoms and eventually a single atom. The interest in EIT with a single atom has been put forward in several theory works over the past decade, especially in the context of nonlinear optics and quantum information [138, 139, 140, 141, 142, 143]. In the

quantum domain of few atoms and few photons, EIT may enable control of the photon statistics of propagating light fields [142] or the realization of strongly interacting photon gases [144, 145]. However, a single atom in free space has minute effects on a propagating laser beam [123] and can not be considered as an optically dense medium. Nevertheless, we have seen in chapter (4) that an optical cavity can enhance the matter-light interaction such that a single atom has an appreciable effect on the transmission of a probe field. This allows us to create an optically dense medium with only a few atoms. The presence of the cavity adds cavity QED features to the phenomenon of EIT. In fact, cavity EIT (CEIT) has attracted considerable interest, both theoretically and experimentally [146, 147, 148].

5.2 Observation of EIT with single atoms in a cavity

The characteristic features of CEIT are best observed in our apparatus when many atoms couple to the cavity simultaneously and create an optically dense medium. The collective atom-cavity coupling strength is then given by $g_N = \sqrt{N}g$ where g is the average coupling constant per atom as introduced in the previous chapters. With $N \approx 15$ atoms in the cavity and $g = 2\pi \times 2\,\mathrm{MHz}$ for the $F = 1 \leftrightarrow F' = 1$ transition the system operates in the collective strong coupling regime and can be considered as optically dense for a resonant transmission probe beam (see section 4.3).

The basis for the observation of cavity EIT is the measurement protocol previously used for differential transmission (Sec. 4.3). Here, the cavity frequency is set resonant with the $F = 1$ to $F' = 1$ transition and approximately 15 atoms are trapped inside the cavity. We record the transmission of the probe laser for three distinct conditions (Fig. 5.1). In the first step of the experimental protocol, we shelve the atoms in the hyperfine state $F = 2$ which effectively decouples them from the cavity. This yields an empty-cavity transmission spectrum used as a reference. In the second step, the atoms are prepared in $F = 1$, such that we realize the case of two-level atoms coupled to the cavity. In the third step, we apply an additional control laser transverse to the cavity axis and resonant with the $F = 2 \leftrightarrow F' = 1$ transition. This forms a Λ-level scheme suitable for the generation of a coherent dark state (Fig. 5.1). The experimental protocol is continuously repeated at a rate of 25 Hz while the probe laser frequency is shifted for every repetition cycle. Thus, we simultaneously measure the three transmission spectra for a given set of trapped atoms.

The recorded spectra are shown in figure (5.1). The empty cavity transmission (atoms prepared in $F = 2$, black data points and theory curve) is of the expected Lorentzian shape. The transmission with atoms prepared in $F = 1$ and only the probe light present (red data and dashed curve) displays the characteristic normal-mode spectrum with a vacuum-Rabi splitting of $2g_N$. At the empty cavity resonance (probe-cavity detuning $\Delta \approx 0$) the transmission is less than 5 % and the atom-cavity system is optically dense. However, this typical cavity QED spectrum changes significantly when the control laser is added to the system (blue data and theory curve) and we obtain a characteristic CEIT spectrum. First, the normal-mode resonances are shifted further apart due to the "dressing" of the atom-cavity energy levels by the control laser. Second, and most important, a narrow

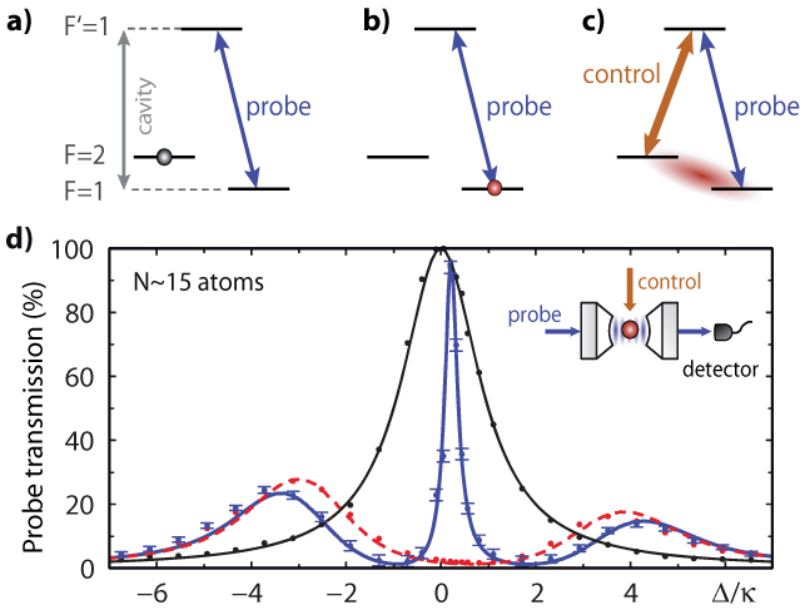

Figure 5.1: Experimental protocol and cavity EIT. The transmission of the atom-cavity system is probed with a weak laser (probe laser-cavity detuning Δ) under three conditions. The cavity frequency is set resonant with the atomic $F = 1 \leftrightarrow F' = 1$ transition (D2-line). **a)** With atoms shelved in the hyperfine state $F = 2$, we record the empty cavity transmission as a reference (black data and curve in d)). **b)** With atoms prepared in $F = 1$, we realize a situation of "two-level atoms" coupled to the cavity and observe a vacuum Rabi splitting with a large collective g (red data and curve in d)). **c)** An additional laser is used to coherently control the optical properties of the atom-cavity system (cavity EIT, blue data and curve in d)). **d)** Measured transmission spectra for on average 15 atoms coupled to the cavity. A narrow transparency window (full width at half maximum $\approx 900\,\mathrm{kHz}$) at the two-photon resonance testifies to the existence of a coherent dark state. Experimental parameters: maximum intracavity photon number 0.02, control power $9\,\mu\mathrm{W}$ (equivalent Rabi frequency $1.3\,\kappa$). Error bars are statistical.

transmission window emerges corresponding to the coherent dark state. We verified that this transmission feature appears at the two-photon resonance by shifting the control laser frequency.

In the next experiment, the transmission measurements introduced above are performed with a single atom trapped in the cavity. The results of these measurements are shown in figure (5.2). The data are an average over 169 complete spectra each obtained using exactly one trapped atom. Without control light present (red data points), the on-resonance transmission is lowered but the vacuum-Rabi splitting is not resolved [1]. This is a consequence of a low effective cooperativity. However, with the control field added, we observe cavity EIT with one atom (blue data points and curve). The transmitted spectrum is no-

[1] The lower transmission contrast for a single atom as compared to section (4.3) is due to the weaker dipole moment of the $F = 1$ to $F' = 1$ transition which limits the maximum achievable coupling to $g_{max} = 2\pi \times 5\,\mathrm{MHz}$. The measured effective g (spatial averaging) on this transition is on the order of $g \approx 2\pi \times 2\,\mathrm{MHz}$. Position dependent Stark shift variations and optical pumping into $F = 2$ further limit the measured transmission contrast.

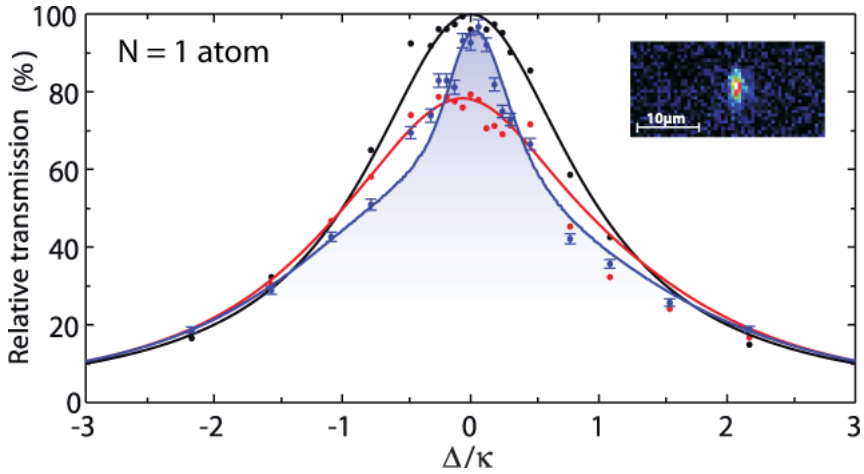

Figure 5.2: Cavity EIT with a single atom. Measured transmission spectra for exactly one atom coupled to the cavity and a control laser power of $3\,\mu$W (equivalent Rabi frequency $0.8\,\kappa$). Colour coding same as in figure (5.1). Under the conditions of CEIT, the transmitted spectrum is notably narrowed, and a nearly perfect transparency is obtained (96 %). The measured transmission contrast is 20 % with respect to the control laser switched off. The inset shows a CCD camera image of a single atom trapped in the cavity (image size $33\,\mu\text{m} \times 16\,\mu\text{m}$).

tably narrowed, and a nearly perfect transparency is obtained. In this respect, the system realizes a quantum light switch based on a single atom with a contrast of about 20%.

Our results present an implementation of CEIT in a completely new regime as the number of atoms is many orders of magnitude smaller than in previous realizations with atomic ensembles [147, 148]. For the concept of CEIT with a single atom our experiment serves as an important proof-of-principle. However, further research which fully exploits the promises of CEIT with single atoms may require higher single atom-cavity coupling.

A detailed analysis of the CEIT experiments and the scaling with atoms added one by one will be subject of the PhD thesis by my colleague Martin Mücke.

6 Phase shaping of single-photon wave packets

While the phase of a coherent light field can be precisely known, the phase of individual photons is not defined [149, 150]. Phase changes within single-photon wave packets, however, have observable effects. In the experiment presented in this chapter, we make use of the atom-cavity system as a deterministic photon source and control the phase within the duration of single-photon wave packets. This phase control is probed in a two-photon interference experiment in which the well-known Hong-Ou-Mandel effect can be reversed.

The results presented in this chapter have been published in:
"Phase shaping of single-photon wave packets",
H. P. Specht, J. Bochmann, M. Mücke, B. Weber, E. Figueroa, D. L. Moehring, and G. Rempe, *Nature Photonics* **3**, 469 (2009).

6.1 Hong-Ou-Mandel effect revisited

A single atom coupled to a cavity is an excellent source of photons with well controlled properties. Using a cavity-mediated Raman process, the generation of single photons with controlled wave packet shape, frequency and polarization has been shown in our group [93, 151, 152, 153, 154]. A distinguishing feature of this photon generation scheme is the ability to produce photons with durations that are much longer than the time resolution of the photodetectors. In two-photon interference experiments, the generated photons have further proven to be indistinguishable [152, 153]. Moreover, the long photon wave packet durations have enabled the time-resolved investigation of two-photon interference [152].

Two-photon interference is a fundamental example of quantum optics and finds applications in linear optical quantum computing [155, 156]. The effect has first been studied in a groundbreaking experiment by Hong, Ou and Mandel in 1987 [157, 158]. In the standard setting of two-photon interference, two identical photons impinge on the two input ports (A and B) of a 50/50 non-polarizing beam splitter (NPBS), represented by the initial state $|\Psi_i\rangle = |1_A 1_B\rangle$ (see Fig. 6.1). Due to the indistinguishability of the photons, the detection of one photon in output port C or D at time t_0 projects the initial product state $|\Psi_i\rangle$ into the "which path" superposition state $|\Psi_\pm(t_0)\rangle = (|1_A, 0_B\rangle \pm |0_A, 1_B\rangle)/\sqrt{2}$ of the remaining photon. For the detection of the second photon, the probability amplitudes of all possible measurement outcomes interfere which gives rise to the Hong-Ou-Mandel effect: In an ideal experiment, the second photon is always detected in the same output port of the beam splitter as the first photon. The Hong-Ou-Mandel effect has attracted continued interest over the past years and various versions of two-photon interference experiments have been discussed [158, 159, 160, 161].

Here, we extend the conventional setting of the Hong-Ou-Mandel effect by allowing an arbitrary phase Δ_ϕ between the components of the superposition states $|\Psi_\pm\rangle$ after the

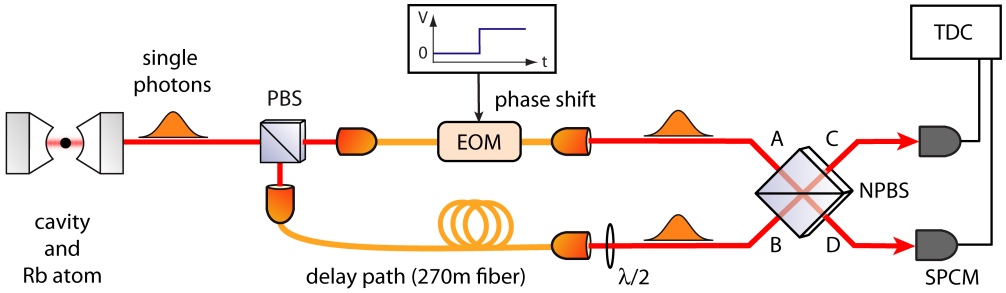

Figure 6.1: Experimental setup. Single photons are generated in a Raman process from single ^{87}Rb atoms traversing the cavity mode. A polarizing beam splitter (PBS) directs the photons randomly into one of two optical paths. In the first path, an electro-optic modulator (EOM) is used to arbitrarily shape the phase of the single photon wave packets. A delay fiber in the second optical path allows two subsequently generated photons to synchronously impinge on a 50/50 non-polarizing beam splitter (NPBS). The photons are detected by single photon counting modules (SPCMs) which are connected to a time to digital converter (TDC). A half wave-plate ($\lambda/2$) rotates the polarization in the delay path to erase which-way information after the PBS.

detection of the first photon. The phase-dependent wave function of the remaining single photon reads

$$|\tilde{\Psi}_{\pm}(t_0+\tau)\rangle = (|1_A, 0_B\rangle \pm e^{i\Delta_\phi(\tau)}|0_A, 1_B\rangle)/\sqrt{2}. \tag{6.1}$$

As a consequence, the probability with which the second photon is detected in either of the two output ports depends on the phase shift Δ_ϕ. Quantitatively, the probability to detect the two photons of an impinging pair in opposite output ports – the coincidence probability p_{coinc} – depends on the magnitude of the accumulated phase shift between the two photon detection events as

$$p_{\text{coinc}} = \sin^2(\Delta_\phi/2). \tag{6.2}$$

Hence, with well tailored phase shifts, one gains control over the photon detection correlations, i. e. wether the two photons are detected in the same or opposite output ports of the beam splitter. Remarkably, at a phase shift of $\Delta_\phi = \pi$ the usual photon coalescence of the Hong-Ou-Mandel effect is turned into anti-coalescence.

The phase shift between the photon detection events can, for example, be induced by a frequency difference between the photons [162, 152]. In the experiment considered in the following, arbitray phase patterns can be imprinted on the single photon superposition state $|\Psi_{\pm}\rangle$ using a fast electro-optic modulator in one input port of the beam splitter.

6.2 Experiment and results

In our experiment, we can indeed realize the ideal situation of two indistinguishable single photons simultaneously impinging on a beam splitter (Fig. 6.1). The photons are generated one-after-the-other using a cavity-mediated STIRAP process (see chapter (2.6) and [93, 151]). After emission from the cavity, the photons are randomly distributed into two

optical paths which are later recombined on a NPBS. One of the two paths acts as a delay line such that a photon which has travelled this path can arrive at the NPBS simultaneously with a subsequently generated photon which has taken the other path. Thus, the stream of independent photons at the cavity ouput is (randomly) converted into photon pairs which are spatially and temporally mode-matched at the input ports of the NPBS.

In our setup, the delay path consists of an optical fiber with a length of 270 m which introduces a propagation time delay of 1.35 μs. The other optical path accomodates a fiber-based electro-optic modulator (EOM) which is used as a fast optical phase shifter. The two output ports of the NPBS are mapped onto single photon detectors (SPCM's, see figure 6.1). Note that when a photon pair causes both detectors to click this is called a "coincidence" event. However, for the spatial correlation of the photons in the output modes of the NPBS this actually means "anti-coalescence".

The photons are generated at a rate of 740 kHz with a Gaussian wave packet shape and a duration of 150 ns. The photon duration is chosen to be much longer than the detector time resolution (2 ns) and the switching times of the EOM (approx. 1 ns) but shorter than the time delay introduced by the delay path (1.35 μs). The rate of photon generation matches this propagation time delay. We operate the experiment in the continuous loading regime (chapter 2) where single atoms probabilistically drift through the cavity in a shallow optical dipole potential. The single photon nature of emission from the atom-cavity system is verified in a Hanbury Brown-Twiss correlation measurement.

The EOM can create arbitrary optical phase shifts between 0 and 3π at a modulation bandwidth of 10 GHz. In principle, any phase structure within this parameter range can be imprinted on a photon wave packet propagating through the EOM. Temporal step functions, linear ramps and sawtooth patterns of the phase shift have been realized experimentally. In the following, we restrict ourselves to the case of a step function type phase modulation. It is applied as a sudden phase shift at the center of the photon wave packet's temporal shape.

For an analysis of the photon coalescence behaviour, the recorded data must be post-selectively grouped into two subensembles depending on wether the applied phase shift occured between the two detection events or not. This is because the phase shift Δ_ϕ introduced by the EOM only becomes effective for photon pairs in which one photon is detected before the phase shift and the other photon is detected after the phase shift.

In figure (6.2) the measured coincidence detection probability is shown as function of the applied phase shift Δ_ϕ for the two subensembles of detected photon pairs. We find that photon pairs for which both detections occured before or after the phase shift always coalesce. This is in agreement with the Hong-Ou-Mandel effect and testifies to the indistinguishability of the impinging photons. However, photon pairs for which the phase shift occured between the detections events exhibit a $\sin^2(\Delta_\phi/2)$ dependence of the coincidence probability, as given by equation (6.2). As expected, a maximum number of coincidences is observed for phase shifts of odd multiples of π, whereas the photons coalesce for even multiples of π.

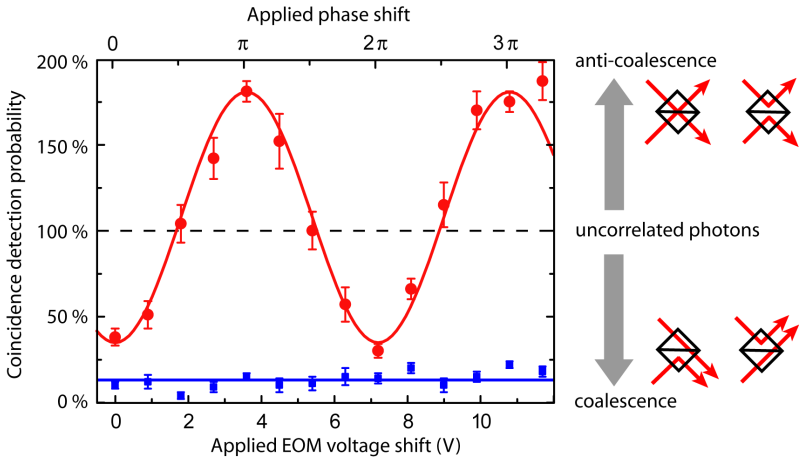

Figure 6.2: Coincidence rate vs. applied phase shift. Red dots show the coincidence detection probability (normalized to uncorrelated photon pairs) as a function of the applied phase shift for the subensemble of photon pairs in which the phase shift occured between the detection events. The solid fitted line follows the sinusoidal behaviour of equation (6.2) with a visibility of $67 \pm 3\,\%$. The coincidence rate for photon pairs detected both before or after the phase shift remains at a low value of $\approx 14\,\%$ (blue squares; average value: solid blue line, offset of 5% is due to multi-atom events and SPCM dark counts). The given error bars are statistical (1 standard deviation). The possible realizations of photon detection events which contribute to the measured coincidence probability are schematically represented for the regimes of coalescence (Hong-Ou-Mandel effect) and anti-coalescence.

It is evident from our data that the usual coalescence of photons as known from standard Hong-Ou-Mandel experiments is turned into anti-coalescence at π-phase shift of the EOM. In the subensemble of photon pairs in which the π-phase shift is effective, the probability to find the two photons in opposite output ports of the NPBS is measured to be $p_{\mathrm{coinc}} = 183 \pm 6\%$ when compared to the random detection of uncorrelated photon pairs (used as $100\,\%$ reference level). In the subensemble with no effective phase shift, the coincidence detection probability is only $16 \pm 2\%$. The deviation from the respective ideal values of 0% and 200% can be easily explained by experimentally limited mode matching (temporally, frequency) between the two sequentially generated photons [163], rare multi-atom events and detector dark counts.

Taken together, our results show that the two-photon interference as described by Hong, Ou and Mandel [157] can be generalized by introducing an arbitrary phase in the which-path superposition of a single photon. In the experiment, the coalescence probabilities of photon pairs is controlled by applying appropriate phase shifts. It must be noted that the observed effect is manifestly different from classical interference of electromagnetic fields but rather originates from the interference of probability amplitudes in the detection process [161].

A detailed analysis of the topic introduced in this chapter will be subject of the PhD thesis of my colleague Holger Specht.

7 Summary and outlook

A new single atom-cavity apparatus has been constructed during the course of this work. It operates in the intermediate-coupling regime of cavity quantum electrodynamics (CQED) and allows the quasi-permanent storage of single atoms. The new atom-cavity system is well-suited as a light-matter interface at the level of single atoms and single photons. In the experiments reported in this thesis, we have observed fundamental phenomena of quantum optics and cavity quantum electrodynamics. We use the enhanced light-matter interaction in the cavity for the controlled generation of single photons, for the efficient detection of atomic states and for realizing light-light interaction mediated by just one atom. As will be explained in the following, the single atom-cavity system described here opens many fascinating perspectives for future experiments.

In the first experiment reported here, we have observed the coherent exchange of energy between a single atom and the intracavity field upon excitation with a short laser pulse. The time-resolved observation of such vacuum Rabi oscillations presents a textbook-type example of CQED in the optical domain. The agreement of the data with theoretical prediction is excellent and a quantitative analysis of the vacuum Rabi oscillations enabled time-domain normal-mode spectroscopy of the atom-cavity system. The short pulse excitation scheme employed in this experiment also allows to produce single photons in a well-defined output mode at the push of a button. Single photon generation by short pulse excitation operates in a regime which significantly differs from the previously studied STIRAP scheme. The emitted photon wave packets have a duration on the order of 100 ns and the repetition rate can be several MHz. Further, this scheme can generate single photons in a superposition of two tunable frequencies.

In a second series of experiments, we have studied schemes for internal state detection of single neutral atoms. Internal state readout of single atoms is at the heart of atomic physics but is also an essential prerequisite for quantum information with neutral atoms. So far, state readout of single atoms had been hampered by atom loss, comparably long readout times or extremely difficult experimental requirements. Here, we overcome these problems and introduce an efficient readout scheme for atomic hyperfine states based on cavity-enhanced fluorescence. This technique has proven to be robust against experimental parameter variations and does not require the strong-coupling regime of CQED. We achieve atomic state readout with a fidelity of better than 99 % in less than 100 μs. Most important, a single atom can be interrogated many hundred times without loss from the optical dipole trap. This presents an essential advancement and establishes neutral atoms as truly stationary carriers of quantum information.

The subsequent investigations of atomic state dependent transmission of the cavity lead to the observation of electromagnetically induced transparency with a single trapped atom. In these measurements, the transmission of a weak light beam through the atom-cavity system has been coherently controlled by means of a transversally applied control laser.

With careful choice of experimental parameters, the optical properties of the atom-cavity system are determined by a coherent dark state. This proof-of-principle experiment marks the starting point for a wealth of related phenomena which remain to be explored in the future (see below).

Finally, we have used the atom-cavity system as a source for exceptionally well-defined single photons. The photon wave packet duration is much larger than the detector time resolution and long enough to imprint user-defined optical phase patterns onto single propagating photons. In a two-photon interference experiment, these phase shaped photons exhibit a tunable coalescence behaviour which emerges as a generalization of the well-known Hong-Ou-Mandel effect.

The experiments named above indicate the high degree of control over single atoms and single photons which has already been achieved. However, future experiments could be spurred by a precise localization of the atom at an antinode of the cavity field and by the elimination of atomic Stark shift variations. Both problems can be solved when the atom is cooled to the motional ground state of the intracavity dipole trap potential [60, 110, 164]. Further, the probabilistic loading of atoms into the cavity may in the future be aided by deterministic re-positioning of atoms into the geometric center of the TEM_{00}-mode of the cavity [77] in order to achieve a high and reproducible value of the atom-cavity coupling.

The experiments presented in this thesis draw their strength from trapping exactly one atom in the cavity and from generating exactly one photon at a time. While working at this level has been a long standing goal in optical CQED and quantum optics, this approach does not yet take advantage of the scalability which neutral atoms and in particular atom-cavity systems offer. In future experiments, the controlled scaling to finite atom numbers and the scaling to two or more connected atom-cavity systems may supersede the now familiar single atom-single photon regime of CQED.

In our setup, the single atom-imaging system already allows to work with a defined number of atoms coupled to the cavity mode. This enables future experiments on two-atom entanglement via projective measurements [165, 102] and possibly cavity-mediated quantum gate operations [166, 167, 168]. Extension to larger atom numbers opens perspectives for spin squeezing [66, 169] and the realization of infinitely long-range interactions in many-body quantum systems [36, 37].

Further exploration of the cavity EIT phenomenon naturally includes the slowing and storage of photons. Of particular interest are effects which depend on the number of atoms and photons such as Fock state dependent slowing of a light pulse or the Fock state specific transmission of light pulses through the cavity. First numerical evaluations have shown that these effects may be observable. However, the signatures are small due to the currently low average atom-cavity coupling strength. With these options at hand, coherent dark states and EIT with a defined number of atoms in a high-finesse cavity present tools with which quantum states of light can be generated, stored and filtered photon by photon.

An exciting prospect for atom-cavity systems is the scalability to distributed quantum

networks [68, 69, 170]. In such a network, photons communicate quantum information to remote locations and establish correlations between distant stationary atoms. Indeed, during the course of this work, first steps have been taken to couple two independent atom-cavity systems. Among a variety of coupling schemes, two options appear especially relevant. In a first scheme, a joint measurement on photons emitted by two atom-cavity systems projects the remote atoms into an entangled state [165, 102]. In another possible realization, one atom-cavity system sends a photon which is entangled with the intracavity atom directly to the second atom-cavity system where the photon is absorbed [68]. Naturally, such quantum networks are testbeds for long-distance teleportation [171] and the construction of a quantum repeater [172].

8 Appendix

8.1 Atom-cavity coupling strength

The atom-light interaction in a cavity is characterized by the coherent coupling rate g and the cooperativity C. The cooperativity is defined as

$$C = \frac{g^2}{2\gamma\kappa} \ . \tag{8.1}$$

With atom and cavity on resonance in the bad cavity limit, the ratio of the probabilities for atomic polarization decay into the cavity output mode and decay into free space is simply

$$\frac{R_{cav}}{R_{spont}} = \frac{2g^2/\kappa}{2\gamma} = 2C \ . \tag{8.2}$$

The cooperativity is directly related to the critical atom number in the cavity $N_a = 1/C$ at which the on-resonance cavity transmission $T/T_0 = (1+2C)^{-2}$ is significantly altered ($T(N_a)/T_0 = 1/9$). Equivalently, the critical photon number $N_p = \gamma^2/(2g^2)$ gives the average number of intracavity photons which are necessary to saturate a given atomic transition. Note that the effective cooperativity $\nu = g^2/[(\Delta_a - i\gamma)(\Delta_c - i\kappa)]$ introduced in [92] and chapter (4) is a generalization of $-2C$.

The coherent atom-cavity coupling rate g_0 at a cavity-field antinode is determined by the dipole matrix element μ_{ge} of the atomic transition and the cavity mode volume V ($V = \pi w_0 d/4$, mode waist w_0, cavith length d).

$$g_0 = \sqrt{\frac{\omega_c}{2\epsilon_0 V\hbar}} \cdot \mu_{ge} \tag{8.3}$$

The applicable value of μ_{ge} depends on the polarization of the cavity field and the internal state of the atom.

For the strongest electric dipole transition of the Rubidium D2-line $5^2\mathrm{S}_{1/2}\ F = 2, m_F = 2$ to $5^2\mathrm{P}_{3/2}\ F' = 3, m_{F'} = 3$, we find $g_0/2\pi = 7.9\,\mathrm{MHz}$ in our cavity. This results in a maximum cooperativity $C = 3.6$, a critical atom number of $N_a = 0.3$ and a critical photon number of $N_p = 0.07$. For isotropic light polarization the coupling is $g_0/2\pi$=5.4 MHz ($C = 1.7, N_a = 0.6, N_p = 0.16$) for the $F = 2 \leftrightarrow F' = 3$ transition. The values of g_0 in our experiment for all transitions of the Rb D2-line are listed in tables a)-d) at the end of this section.

The atom-cavity coupling rate g_0 is spatially modulated by the standing wave structure of cavity field mode $\psi_c(\mathbf{r})$:

$$g(\mathbf{r}) = g_0\psi_c(\mathbf{r}) \ . \tag{8.4}$$

The residual motion of an atom trapped inside the cavity samples this spatial modulation of g. The time scales at which this averaging becomes effective are given by the trap frequencies of the optical dipole potential. Along the axis of the standing wave dipole trap (1064 nm, waist 16 μm, depth $\approx$3 mK), the trap frequency is on the order of 1 MHz. However, along the radial direction of this trap (e.g. the cavity axis), the trap frequency is only a few kHz. The spatial averaging discussed below becomes effective for single probe intervals with duration larger than 10 μs.

In the following, g-averaging along all three axes of atomic motion is discussed. First, we assume the atom is permanently trapped in one potential well of the standing wave dipole trap in the center of the cavity mode. Along the cavity axis, the atom moves over a range of up to 6 μm (inferred from camera images, see section 2.6). Therefore, the atom samples more than 10 nodes and antinodes of the cavity mode $\psi_c(\mathbf{r})$ and averaging along the cavity axis reduces the coupling g (g^2) to 64% (50%) of g_0 ($g_0{}^2$). Along the vertical spatial axis, we estimate the atom also moves over a range of 6 μm. Due to geometry, the concomitant reduction in g and g^2 is negligible ($\leq$1%).

In different loading attempts, single atoms may be trapped in different potential wells of the dipole trap. The ensemble average of g depends on the probability distribution of trapping locations relative to the center of cavity mode. Assuming a random distribution in the region $\pm$12.5 μm from the geometric cavity center (compare cavity mode waist: $w_0 = 30\,\mu$m) reduces the effective g to 94% of g_0 and the effective g^2 to 89% of $g_0{}^2$.

In conclusion, the effective spatially averaged g for a trapped atom is about 60 % of g_0. For the $F = 2 \leftrightarrow F' = 3$ transition and assuming isotropic probe light polarization ($g_0/2\pi = 5.4$ MHz), we find an average coupling rate $g_{av}/2\pi = 3.2$ MHz. This value is consistent with experimental observations. Similarly, we find for the $F = 1 \leftrightarrow F' = 1$ transition and isotropic polarization ($g_0/2\pi = 4.2$ MHz) an average coupling rate $g_{av}/2\pi =$ 2.5 MHz. Finally, the effective cooperativities associated with these values of g must include averaging over the atomic detuning caused by position-dependent Stark shifts.

a) Atom-cavity coupling constants g_0 (in units of MHz/2π) for dipole transitions from $5^2\mathrm{S}_{1/2}$ $F = 2, m_F$ to $5^2\mathrm{P}_{3/2}$ $F', m_{F'} = m_F + 1$ (σ^+-polarized light).

	$m_F = -2$	$m_F = -1$	$m_F = 0$	$m_F = 1$	$m_F = 2$
F'=3	2.0	3.5	5.0	6.4	7.9
F'=2	3.2	3.9	3.9	3.2	0
F'=1	2.5	1.8	1.0	0	0

b) Atom-cavity coupling constants g_0 (in units of MHz/2π) for dipole transitions from $5^2\mathrm{S}_{1/2}$ $F = 2, m_F$ to $5^2\mathrm{P}_{3/2}$ $F', m_{F'} = m_F$ (π-polarized light).

	$m_F = -2$	$m_F = -1$	$m_F = 0$	$m_F = 1$	$m_F = 2$
F'=3	-4.6	-5.8	-6.1	-5.8	-4.6
F'=2	-4.6	-2.3	0	2.3	4.6
F'=1	0	1.8	2.0	1.8	0

c) Atom-cavity coupling constants g_0 (in units of MHz/2π) for dipole transitions from $5^2S_{1/2}$ $F = 1, m_F$ to $5^2P_{3/2}$ $F', m_{F'} = m_F + 1$ (σ^+-polarized light).

	$m_F = -1$	$m_F = 0$	$m_F = 1$
F'=2	2.3	3.9	5.6
F'=1	5.1	5.1	0
F'=0	4.6	0	0

d) Atom-cavity coupling constants g_0 (in units of MHz/2π) for dipole transitions from $5^2S_{1/2}$ $F = 1, m_F$ to $5^2P_{3/2}$ $F', m_{F'} = m_F$ (π-polarized light).

	$m_F = -1$	$m_F = 0$	$m_F = 1$
F'=2	-3.9	-4.6	-3.9
F'=1	-5.1	0	5.1
F'=0	0	4.6	0

8.2 Single atom imaging system

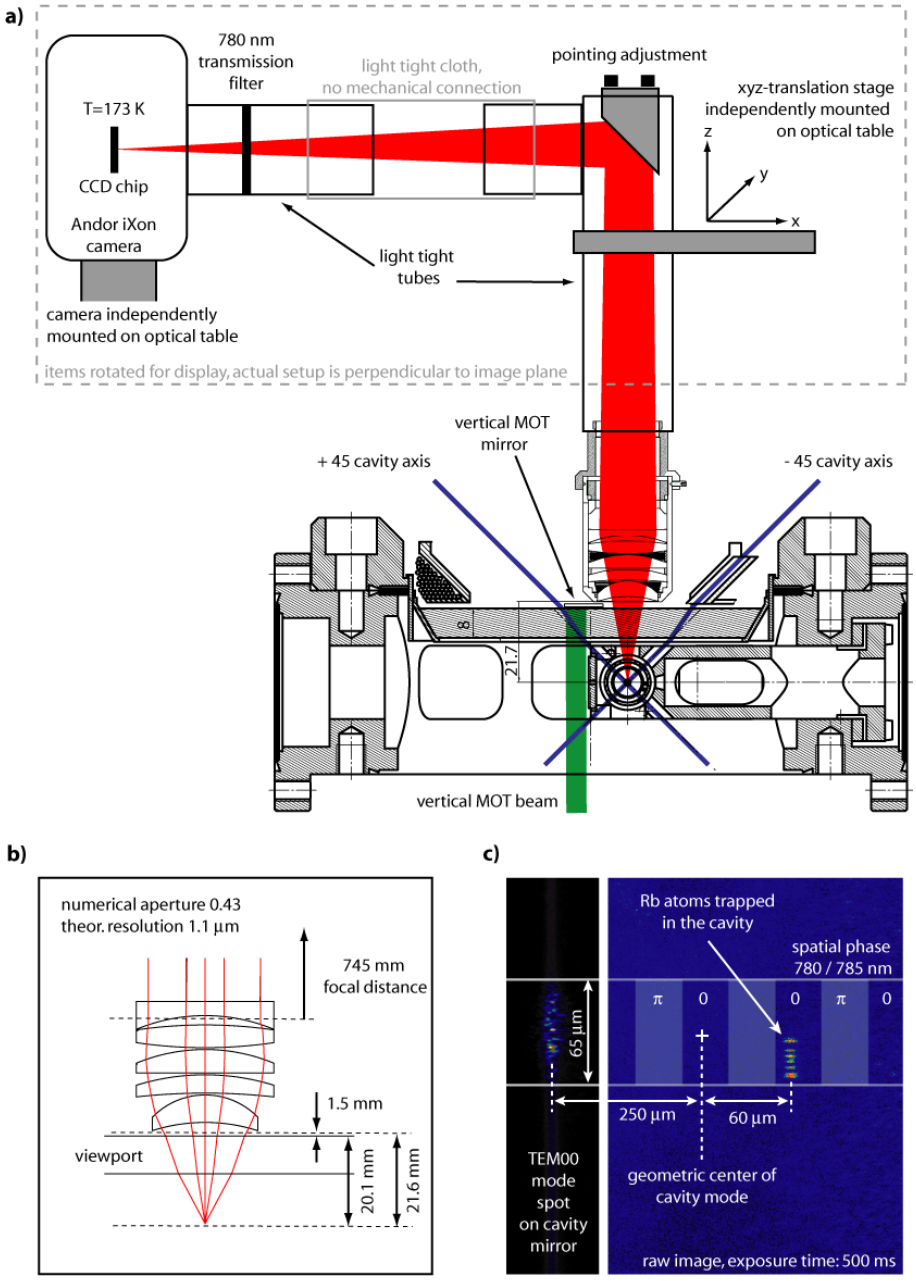

Figure 8.1: Imaging system. a) Layout of vacuum chamber and imaging system. **b)** Schematic of objective and lenses. **c)** Sample image of atoms trapped inside the cavity. The position of atoms relative to the geometric center of the cavity mode is determined with $\pm 5\mu$m precision. Scattering of light in the cavity mode at the cavity mirror surfaces (example shown in left column) serves as geometric reference for localizing the cavity mode.

8.3 Dimensions of the vacuum system

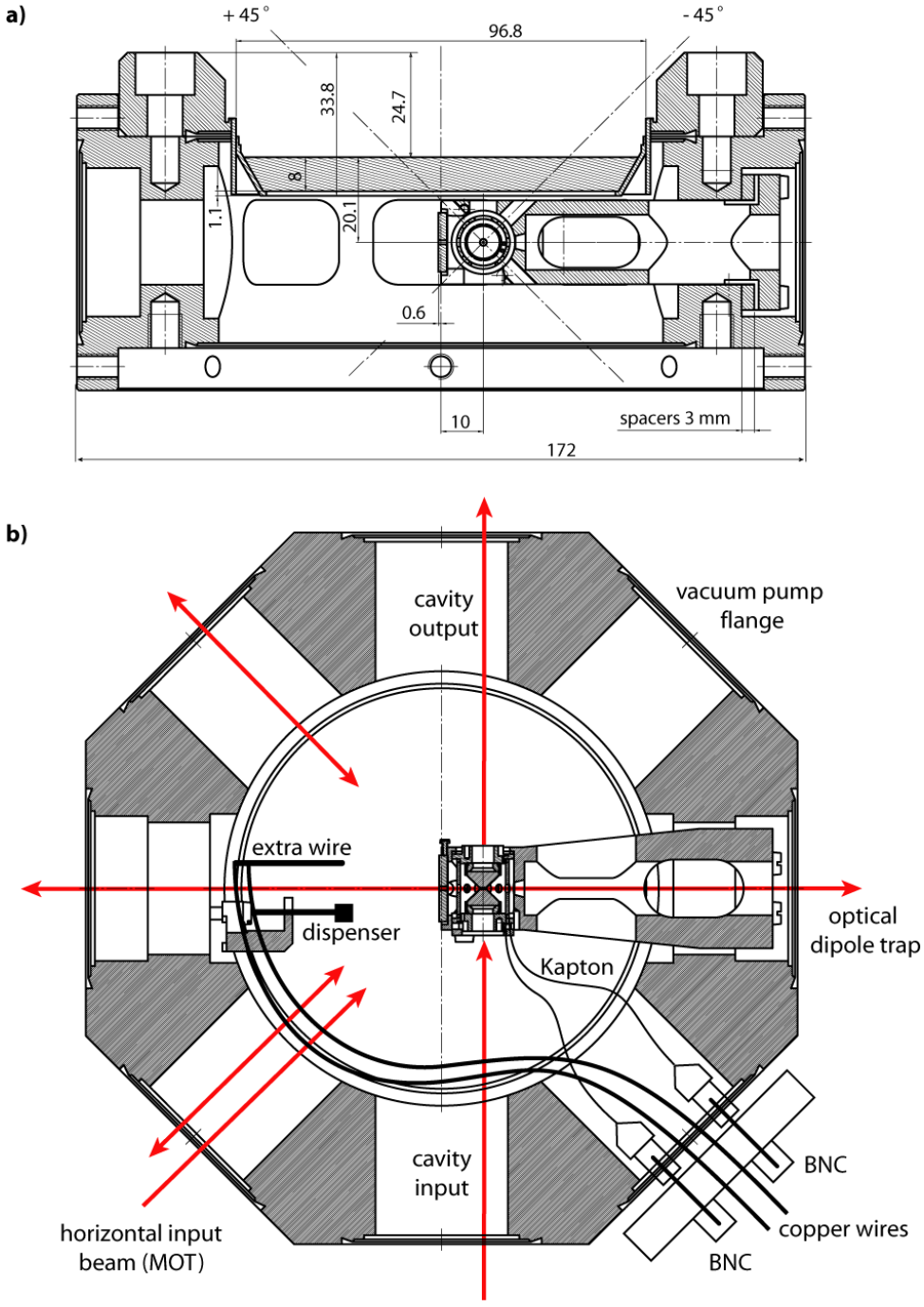

Figure 8.2: Vacuum system. a) Scale drawing of the vacuum chamber and cavity holder (side view). **b)** Scale drawing of the vacuum chamber and cavity holder (top view). The electrical wiring for the Rb dispenser and cavity piezo is indicated by black solid lines. Laser beams are indicated by arrows.

8.4 Schematic layout of the optical table

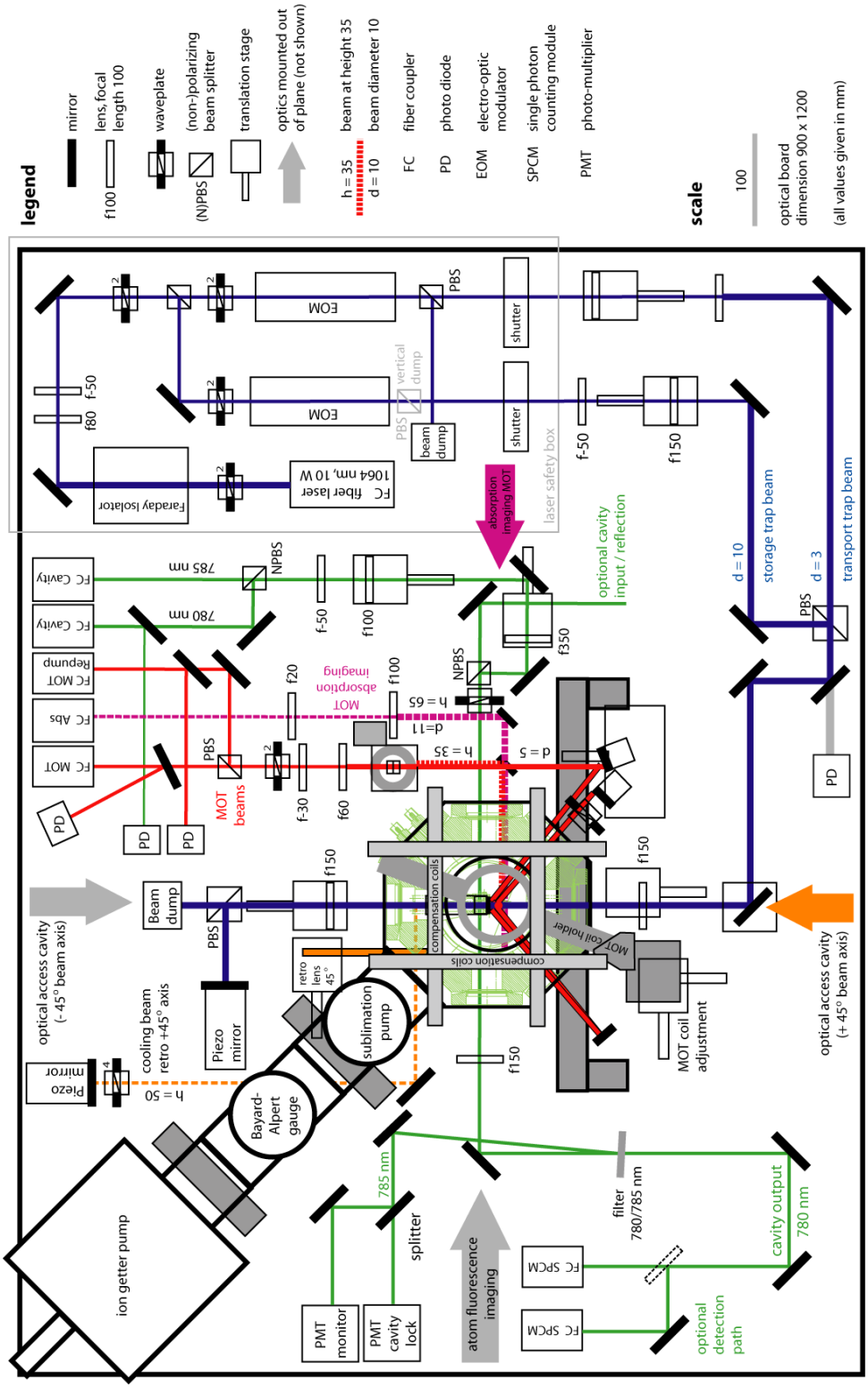

8.5 Frequency comb

In our experimental setup, a frequency comb system serves as an absolute frequency standard. In the years 2006 to 2009, a frequency comb signal was provided by the precision measurement group of Prof. Hänsch (T. Udem, R. Holzwarth) via a 120 m optical fiber link. Initially, it had served as a reference for the cavity stabilization laser at 785 nm but has later been adopted for other purposes as well. As of 2009, our laboratory hosts its own frequency comb system whose signal is supplied to all laboratories of our group.

At the heart of the frequency comb system is a pulsed laser with repetition rate f_{rep} whose output spectrum exhibits a distinct comb structure of frequency components with spacing f_{rep} (Fig. 8.3). Further, the absolute position of this comb structure is given by the offset frequency f_{CEO}. It depends on the carrier-envelope phase which is the temporal phase of the electromagnetic field oscillation with respect to the envelope function of each laser pulse. A shift of the carrier-envelope phase from one pulse to the next is called carrier-envelope phase slip (Fig. 8.3). The absolute optical frequencies of the comb spectrum are completely determined by the simple equation

$$f_n = f_{CEO} + n f_{rep} \tag{8.5}$$

where n is a large integer number. Both frequencies f_{rep} and f_{CEO} are in the 10 ... 300 MHz range which is easily accessible with electronic counters and AD-converters. Therefore, a frequency comb system universally maps the precision of standard atomic clocks (radio frequency domain) to the optical domain (10^{15} Hz).

Our frequency comb was manufactured by MenloSystems and set up in our laboratory in September 2009. It consists of several independent modules. At its core is a pulsed fiber laser with a repetition rate $f_{rep} = 250$ MHz. This rate is fine-tuned and stabilized via a piezo-electric element which controls the pulse round trip time in the laser. The optical output spectrum is centered around 1550 nm. Self-mode locking operation is optimized by additional piezo-elements which tweak the optical fiber. A second essential module is the f-2f interferometer which is needed for determining the carrier-envelope offset-frequency f_{CEO}. In this module, a share of the original comb spectrum interferes with its frequency-doubled counterpart. The value of f_{CEO} can be extracted by interfering a comb peak A at the blue end of the original spectrum with a frequency-doubled comb peak B from the red end of the spectrum one octave away ($n_A = 2n_B$). The CEO frequency emerges as a lowest beat frequency because $2(f_{CEO} + n_B f_{rep}) - (f_{CEO} + n_A f_{rep}) = f_{CEO}$. This self-referencing of the comb requires an originally octave spanning optical spectrum. The broad spectrum is obtained by broadening of the pulsed laser output using non-linear processes in a hollow core fiber. The CEO frequency can be actively stabilized to a desired value (here: 10 MHz) via the power of the pump laser diodes of the fiber laser.

The feedback loops for the stabilization of CEO and repetition rate are based on optical beat note detection. Direct feedback circuitry is accompanied by control software which ensures long term stability. In the current operation mode, the frequency comb system can run independently for weeks. As a 10 MHz reference signal for the beat note stabilization we use a stable hydrogen-maser signal supplied by the group of Prof. Hänsch. Additionally

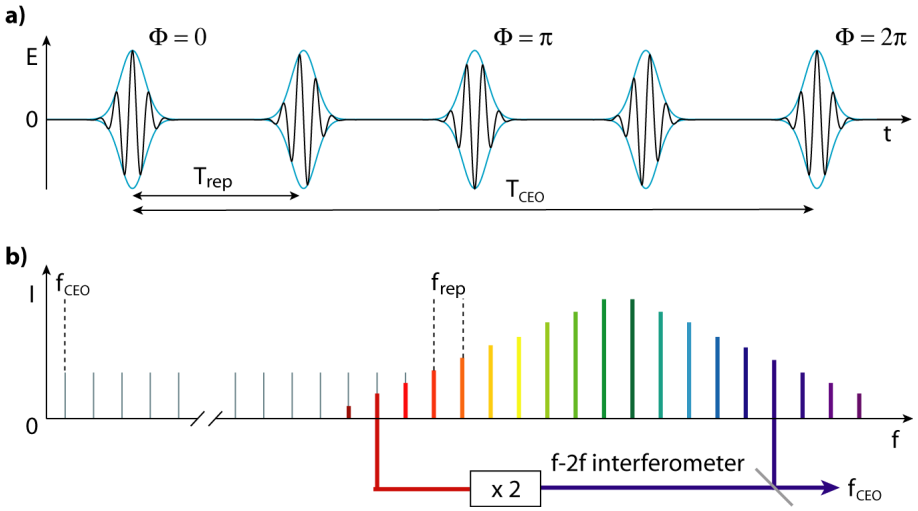

Figure 8.3: Frequency comb output in the time and frequency domain. a) Electrical field of a coherent pulsed source in the time domain. Pulses are emitted at time intervals T_{rep} with a characteristic carrier-envelope phase shift Φ from one pulse to the next which accumulates to 2π within a time T_{CEO}. **b)** In the frequency domain, the output field exhibits a comb-like structure with frequency components separated by the repetition rate f_{rep} and carrier-envelope offset frequency f_{CEO} which can be measured with the f-2f interferometer. The frequencies f_{rep} and f_{CEO} are actively stabilized and fall into the MHz regime. The optical output spectrum must span one ocatve to allow self-referencing in the f-2f interferometer.

installed modules of the frequency comb system amplify the optical output spectrum for use in the spectral ranges 775 to 795 nm and 1000 to 2000 nm. The whole comb setup is placed on a separate optical table shielded from sonic noise and air currents by a massive housing.

The absolute frequency stability of the comb on time scales longer than 1 s is outstanding and naturally sufficient for our experiments. This has been confirmed by a benchmark measurement of the relative frequency stability of two frequency combs technically equivalent to ours carried out in 2007 by B. Bernhard et al. [173]. The passive short-term stability of the frequency comb has so far proven sufficient for our experiments which typically require a laser frequency stability on the order of 100 kHz on all time scales. From measurements in three separate cavity setups (”Pistol”, ”QGate”, ”Cavies”), we can state that in the range of 1 ms to 1 s we do not observe frequency fluctuations in the comb spectrum.

The frequency comb delivers approx. 100 mW of optical power in the spectral range 760 to 800 nm (Fig. **??**). This output is coupled into a fiber network which supplies the laboratories of our group. Typically 10 mW of optical power are delivered to each laboratory. A beat lock of a diode laser to a comb line can be realized with 1 mW of diode laser light and 100 μW of comb light (integrated power over a 5 nm wide spectrum). Monitoring the diode laser frequency with a high-precision wavemeter with resolution better than 100 MHz (e.g. ”HighFinesse WS” series) allows us to lock the laser to a specific spectral peak of the frequency comb.

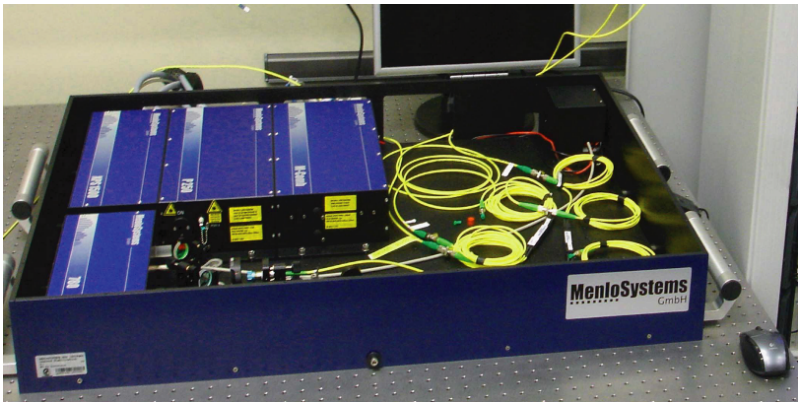

Figure 8.4: Photograph of the installed frequency comb system without the acoustic noise shielding.

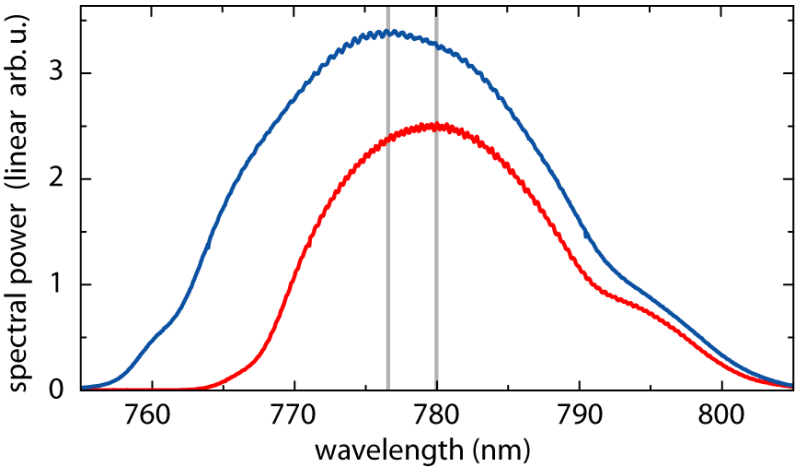

Figure 8.5: Measured spectral power distribution of the comb output at 760 - 800 nm. Upper blue curve: Standard spectrum with a total power of 100 mW, individual comb lines are not resolved in this measurement. In one attempt, the spectral maximum of the output has been shifted to longer wavelengths (lower red curve) by tuning of temperature and angle of the frequency-doubler crystal. The shift is accompanied by a loss in total power and does not increase the signal at 795 nm.

Bibliography

[1] Freedman, S. J. and Clauser, J. F. Experimental test of local hidden-variable theories. *Phys. Rev. Lett.*, **28** 938–941 (1972).

[2] Aspect, A., Grangier, P., and Roger, G. Experimental tests of realistic local theories via bell's theorem. *Phys. Rev. Lett.*, **47** 460–463 (1981).

[3] Bouwmeester, D., Pan, J.-W., Mattle, K., Eibl, M., Weinfurter, H., and Zeilinger, A. Experimental Quantum Teleportation. *Nature*, **390** 575–579 (1997).

[4] Bergquist, J. C., Hulet, R. G., Itano, W. M., and Wineland, D. J. Observation of quantum jumps in a single atom. *Phys. Rev. Lett.*, **57** 1699–1702 (1986).

[5] Leibfried, D., Knill, E., Seidelin, S., Britton, J., Blakestad, R. B., Chiaverini, J., Hume, D. B., Itano, W. M., Jost, J. D., Langer, C., *et al.* Creation of a six-atom "Schrödinger cat" state. *Nature*, **438** 639–642 (2005).

[6] Duerr, S., Nonn, T., and Rempe, G. Fringe visibility and which-way information in an atom interferometer. *Phys. Rev. Lett.*, **81** 5705–5709 (1998).

[7] Nogues, G., Rauschenbeutel, A., Osnaghi, S., Brune, M., Raimond, J. M., and Haroche, S. Seeing a single photon without destroying it. *Nature*, **400** 239 – 242 (1999).

[8] Hämäläinen, M., Hari, R., Ilmoniemi, R. J., Knuutila, J., and Lounasmaa, O. V. Magnetoencephalography—theory, instrumentation, and applications to noninvasive studies of the working human brain. *Rev. Mod. Phys.*, **65** 413–497 (1993).

[9] Grünberg, P. A. Nobel lecture: From spin waves to giant magnetoresistance and beyond. *Rev. Mod. Phys.*, **80** 1531–1540 (2008).

[10] Wineland, D. J., Bollinger, J. J., Itano, W. M., Moore, F. L., and Heinzen, D. J. Spin squeezing and reduced quantum noise in spectroscopy. *Physical Review A*, **46** R6797–R6800 (1992).

[11] Bergquist, J., Jefferts, S., and Wineland, D. Time measurement at the millennium. *Physics Today*, **54** 37–42 (2001).

[12] Chou, C. W., Hume, D. B., Koelemeij, J. C. J., Wineland, D. J., and Rosenband, T. Frequency comparison of two high-accuracy Al+ optical clocks. *Phys. Rev. Lett.*, **104** 070802 (2010).

[13] Dowling, J. and Milburn, G. Quantum technology: The second quantum revolution. *Philos. Trans. R. Soc. Lond. Ser. A-Math. Phys. Eng. Sci.*, **361** 1655–1674 (2003).

[14] Feynman, R. Simulating physics with computers. *Int. J. Theor. Phys.*, **21** 467–488 (1982).

[15] Deutsch, D. Quantum theory, the Church-Turing principle and the universal quantum computer. *Proc. R. Soc. Lond. A*, **400** 97–117 (1985).

[16] Bennett, C. H. Quantum Information and Computation. *Phys. Today*, **October** 24–30 (1995).

[17] Benioff, P. The computer as a physical system: A microscopic quantum mechanical Hamiltonian model of computers as represented by Turing machines. *Journal of Statistical Physics*, **22** 563 (1980).

[18] Grover, L. *Proc. 28 Annual ACM Symposium on the Theory of Computing*. ACM Press New York (1996).

[19] Deutsch, D. and Jozsa, R. Rapid Solution of Problems by by Quantum Computation. *Proc. R. Soc. Lond.*, **439** 553 (1992).

[20] Shor, P. W. Polynomal-time algorithms for prime factorization and discrete logarithms on a quantum computer. *SIAM Review*, **41** 303–332 (1997).

[21] Cleve, R., Ekert, A., Macchiavello, C., and Mosca, M. Quantum algorithms revisited. *arXiv*, pages quant–ph/9708016 (1997).

[22] Gershenfeld, N. A. and Chuang, I. L. Bulk Spin-Resonance Quantum Computation. *Science*, **275** 350–356 (1997).

[23] Lloyd, S. Universal Quantum Simulators. *Science*, **273** 1073–1078 (1996).

[24] Friedenauer, A., Schmitz, H., Glueckert, J. T., Porras, D., and Schaetz, T. Simulating a quantum magnet with trapped ions. *Nature Phys.*, **4** 757–761 (2008).

[25] Bloch, I., Dalibard, J., and Zwerger, W. Many-body physics with ultracold gases. *Rev. Mod. Phys.*, **80** 885–964 (2008).

[26] Gerritsma, R., Kirchmair, G., Zaehringer, F., Solano, E., Blatt, R., and Roos, C. F. Quantum simulation of the Dirac equation. *Nature*, **463** 68–72 (2010).

[27] Bennett, C. and Brassard, G. In *Proc. IEEE Int. Conference on Computers, Systems and Signal Processing*. IEEE, New York (1984).

[28] Jennewein, T., Simon, C., Weihs, G., Weinfurter, H., and Zeilinger, A. Quantum cryptography with entangled photons. *Phys. Rev. Lett.*, **84** 4729–4732 (2000).

[29] Gisin, N., Ribordy, G., Tittel, W., and Zbinden, H. Quantum Cryptography. *Rev. Mod. Phys.*, **74** 145 – 195 (2002).

[30] Zoller, P., Beth, T., Binosi, D., Blatt, R., Briegel, H., Bruss, D., Calarco, T., Cirac, J., Deutsch, D., Eisert, J., *et al.* Quantum information processing and communication - Strategic report on current status, visions and goals for research in Europe. *Eur. Phys. J. D*, **36** 203–228 (2005).

[31] DiVincenzo, D. P. The Physical Implementation of Quantum Computation. *Fortschr. Phys.*, **48** 771 (2000).

[32] Purcell, E. M. Spontaneous Emission Probabilities at Radio Frequencies. *Phys. Rev.*, **69** 681 (1946).

[33] Jaynes, E. T. and Cummings, F. W. Comparison of Quantum and Semiclassical Radiation Theories with Application to the Beam Maser. *Proc. IEEE*, **51** 89–109 (1963).

[34] Shore, B. W. and Knight, P. L. The Jaynes-Cummings model. *Journal of Modern Optics*, **40** 1195–1238 (1993).

[35] Raimond, J. M., Brune, M., and Haroche, S. Colloquium: Manipulating quantum entanglement with atoms and photons in a cavity. *Rev. Mod. Phys.*, **73** 565 – 582 (2001).

[36] Solano, E., Agarwal, G., and Walther, H. Strong-driving-assisted multipartite entanglement in cavity QED. *Phys. Rev. Lett.*, **90** (2003).

[37] Baumann, C., Guerlin, C., Brennecke, F., and Esslinger, T. Dicke quantum phase transition with a superfluid gas in an optical cavity. *Nature*, **464** 1301–1306 (2010).

[38] Kaluzny, Y., Goy, P., Gross, M., Raimond, J. M., and Haroche, S. Observation of self-induced rabi oscillations in two-level atoms excited inside a resonant cavity: The ringing regime of superradiance. *Phys. Rev. Lett.*, **51** 1175–1178 (1983).

[39] Meschede, D., Walther, H., and Muller, G. One-atom MASER. *Phys. Rev. Lett.*, **54** 551–554 (1985).

[40] Rempe, G. and Walther, H. Observation of quantum collapse and revival in a one-atom MASER. *Phys. Rev. Lett.*, **58** 353–356 (1987).

[41] Brune, M., Raimond, J. M., Goy, P., Davidovich, L., and Haroche, S. Realization of a two-photon maser oscillator. *Phys. Rev. Lett.*, **59** 1899–1902 (1987).

[42] Brune, M., Nussenzveig, P., Schmidt-Kaler, F., Bernardot, F., Maali, A., Raimond, J. M., and Haroche, S. From lamb shift to light shifts: Vacuum and subphoton cavity fields measured by atomic phase sensitive detection. *Phys. Rev. Lett.*, **72** 3339–3342 (1994).

[43] Gleyzes, S., Kuhr, S., Guerlin, C., Bernu, J., Deléglise, S., Hoff, U. B., Brune, M., Raimond, J.-M., and Haroche, S. Quantum jumps of light recording the birth and death of a photon in a cavity. *Nature*, **446** 297–300 (2007).

[44] Rempe, G., Thompson, R. J., Brecha, R. J., Lee, W. D., and Kimble, H. J. Optical Bistability and Photon Statistics in Cavity Quantum Electrodynamics. *Phys. Rev. Lett.*, **67** 1727–1730 (1991).

[45] Thompson, R. J., Rempe, G., and Kimble, H. J. Observation of Normal-Mode Splitting for an Atom in an Optical Cavity. *Phys. Rev. Lett.*, **68** 1132–1135 (1992).

[46] Pinkse, P. W. H., Fischer, T., Maunz, P., and Rempe, G. Trapping an Atom with Single Photons. *Nature*, **404** 365–368 (2000).

[47] Hood, C. J., Lynn, T., Doherty, A., Parkins, A., and Kimble, H. The atom-cavity microscope: Single atoms bound in orbit by single photons. *Science*, **287** 1447–1453 (2000).

[48] Boca, A., Miller, R., Birnbaum, K. M., Boozer, A. D., McKeever, J., and Kimble, H. J. Observation of the Vacuum Rabi Spectrum for One Trapped Atom. *Phys. Rev. Lett.*, **93** 233603 (2004).

[49] Maunz, P., Puppe, T., Schuster, I., Syassen, N., Pinkse, P. W. H., and Rempe, G. Cavity cooling of a single atom. *Nature*, **428** 50–52 (2004).

[50] Schuster, I., Kubanek, A., Fuhrmanek, A., Puppe, T., Pinkse, P., Murr, K., and Rempe, G. Nonlinear spectroscopy of photons bound to one atom. *Nature Physics*, **4** 382–385 (2008).

[51] Imamoglu, A., Awschalom, D. D., Burkard, G., DiVincenzo, D. P., Loss, D., Sherwin, M., and Small, A. Quantum information processing using quantum dot spins and cavity QED. *Phys. Rev. Lett.*, **83** 4204–4207 (1999).

[52] Solomon, G. S., Pelton, M., and Yamamoto, Y. Single-mode spontaneous emission from a single quantum dot in a three-dimensional microcavity. *Phys. Rev. Lett.*, **86** 3903–3906 (2001).

[53] Yoshie, T., Scherer, A., Hendrickson, J., Khitrova, G., Gibbs, H., Rupper, G., Ell, C., Shchekin, O., and Deppe, D. Vacuum Rabi splitting with a single quantum dot in a photonic crystal nanocavity. *Nature*, **432** 200–203 (2004).

[54] Reithmaier, J. P., Sek, G., Loffler, A., Hofmann, C., Kuhn, S., Reitzenstein, S., Keldysh, L. V., Kulakovskii, V. D., Reinecke, T. L., and Forchel, A. Strong coupling in a single quantum dot-semiconductor microcavity system. *Nature*, **432** 197–200 (2004).

[55] Wallraff, A., Schuster, D. I., Blais, A., Frunzio, L., Huang, R. S., Majer, J., Kumar, S., Girvin, S. M., and Schoelkopf, R. J. Strong coupling of a single photon to a superconducting qubit using circuit quantum electrodynamics. *Nature*, **431** 162–167 (2004).

[56] Fink, J. M., Goeppl, M., Baur, M., Bianchetti, R., Leek, P. J., Blais, A., and Wallraff, A. Climbing the Jaynes-Cummings ladder and observing its root n nonlinearity in a cavity QED system. *Nature*, **454** 315–318 (2008).

[57] Deppe, F., Mariantoni, M., Menzel, E. P., Marx, A., Saito, S., Kakuyanagi, K., Tanaka, H., Meno, T., Semba, K., Takayanagi, H., *et al.* Two-photon probe of the Jaynes-Cummings model and controlled symmetry breaking in circuit QED. *Nature Phys.*, **4** 686–691 (2008).

[58] Vernooy, D. W., Furusawa, A., Georgiades, N. P., Ilchenko, V. S., and Kimble, H. J. Cavity QED with High-Q Whispering Gallery Modes. *Phys. Rev. A*, **57** R2293 (1998).

[59] Spillane, S. M., Kippenberg, T. J., Vahala, K. J., Goh, K. W., Wilcut, E., and Kimble, H. J. Ultrahigh-Q toroidal microresonators for cavity quantum electrodynamics. *Phys. Rev. A*, **71** 013817 (2005).

[60] Colombe, Y., Steinmetz, T., Dubois, G., Linke, F., Hunger, D., and Reichel, J. Strong atom-field coupling for Bose-Einstein condensates in an optical cavity on a chip. *Nature*, **450** 272–276 (2007).

[61] Dayan, B., Parkins, A. S., Aoki, T., Ostby, E. P., Vahala, K. J., and Kimble, H. J. A photon turnstile dynamically regulated by one atom. *Science*, **319** 1062–1065 (2008).

[62] Poellinger, M., O'Shea, D., Warken, F., and Rauschenbeutel, A. Ultrahigh-Q Tunable Whispering-Gallery-Mode Microresonator. *Phys. Rev. Lett.*, **103** (2009).

[63] Arcizet, O., Cohadon, P. F., Briant, T., Pinard, M., and Heidmann, A. Radiation-pressure cooling and optomechanical instability of a micromirror. *Nature*, **444** 71–74 (2006).

[64] Brennecke, F., Ritter, S., Donner, T., and Esslinger, T. Cavity optomechanics with a Bose-Einstein condensate. *Science*, **322** 235–238 (2008).

[65] Murch, K. W., Moore, K. L., Gupta, S., and Stamper-Kurn, D. M. Observation of quantum-measurement backaction with an ultracold atomic gas. *Nature Phys.*, **4** 561–564 (2008).

[66] Leroux, I. D., Schleier-Smith, M. H., and Vuletić, V. Implementation of cavity squeezing of a collective atomic spin. *Phys. Rev. Lett.*, **104** 073602 (2010).

[67] Schliesser, A., Arcizet, O., Riviere, R., Anetsberger, G., and Kippenberg, T. J. Resolved-sideband cooling and position measurement of a micromechanical oscillator close to the Heisenberg uncertainty limit. *Nature Phys.*, **5** 509–514 (2009).

[68] Cirac, J. I., Zoller, P., Kimble, H. J., and Mabuchi, H. Quantum state transfer and entanglement distribution among distant nodes in a quantum network. *Phys. Rev. Lett.*, **78** 3221–3224 (1997).

[69] Kimble, H. J. The quantum internet. *Nature*, **453** 1023–1030 (2008).

[70] Schrader, D., Dotsenko, I., Khudaverdyan, M., Miroshnychenko, Y., Rauschenbeutel, A., and Meschede, D. Neutral atom quantum register. *Phys. Rev. Lett.*, **93** 150501 (2004).

[71] Lengwenus, A., Kruse, J., Volk, M., Ertmer, W., and Birkl, G. Coherent manipulation of atomic qubits in optical micropotentials. *Appl. Phys. B: Lasers and Optics*, **86** 377–383 (2007).

[72] Rosenfeld, W., Hocke, F., Henkel, F., Krug, M., Volz, J., Weber, M., and Weinfurter, H. Towards long-distance atom-photon entanglement. *Phys. Rev. Lett.*, **101** 260403 (2008).

[73] Karski, M., Förster, L., Choi, J.-M., Steffen, A., Alt, W., Meschede, D., and Widera, A. Quantum walk in position space with single optically trapped atoms. *Science*, **325** 174 (2009).

[74] Wilk, T., Gaëtan, A., Evellin, C., Wolters, J., Miroshnychenko, Y., Grangier, P., and Browaeys, A. Entanglement of two individual neutral atoms using rydberg blockade. *Phys. Rev. Lett.*, **104** 010502 (2010).

[75] Isenhower, L., Urban, E., Zhang, X. L., Gill, A. T., Henage, T., Johnson, T. A., Walker, T. G., and Saffman, M. Demonstration of a neutral atom controlled-not quantum gate. *Phys. Rev. Lett.*, **104** 010503 (2010).

[76] Nußmann, S. *Kühlen und Positionieren eines Atoms in einem optischen Resonator*. Ph.D. thesis, Max-Planck Institut für Quantenoptik (2005).

[77] Nußmann, S., Hijlkema, M., Weber, B., Rohde, F., Rempe, G., and Kuhn, A. Sub-Micron Positioning of Single Atoms in Micro Cavities. *Phys. Rev. Lett.*, **95** 173602 (2005).

[78] Nußmann, S., Murr, K., Hijlkema, M., Weber, B., Kuhn, A., and Rempe, G. Vacuum-stimulated cooling of single atoms in three dimensions. *Nature Physics*, **1** 122 (2005).

[79] Metcalf, H. J. and van der Straten, P. *Laser Cooling and Trapping*. Springer, New York (1999).

[80] Grimm, R., Weidemuller, M., and Ovchinnikov, Y. B. Optical dipole traps for neutral atoms. *Adv. At. Mol. Opt. Phys.*, **42** 95–170 (2000).

[81] Hijlkema, M. *Single photons from a single atom trapped in a high-finesse optical cavity*. Ph.D. thesis, Max-Planck-Institut für Quantenoptik und Technische Universität München (2007).

[82] Karski, M., Förster, L., Choi, J. M., Alt, W., Widera, A., and Meschede, D. Nearest-neighbor detection of atoms in a 1d optical lattice by fluorescence imaging. *Phys. Rev. Lett.*, **102** 053001 (2009).

[83] Hijlkema, M., Weber, B., Specht, H. P., Webster, S. C., Kuhn, A., and Rempe, G. A single-photon server with just one atom. *Nature Physics*, **3** 253–255 (2007).

[84] Murr, K., Nußmann, S., Puppe, T., Hijlkema, M., Weber, B., Webster, S., Kuhn, A., and Rempe, G. Three-dimensional cavity cooling and trapping in an optical lattice. *Phys. Rev. Lett.*, **96** 253001 (2006).

[85] Kuhn, A. and Rempe, G. Optical cavity QED: Fundamentals and application as a single-photon light source. In F. D. Martini and C. Monroe, editors, *Experimental Quantum Computation and Information*, vol. CXLVIII, pages 37–66. Int. School of Physics Enrico Fermi, IOS Press, Amsterdam (2002).

[86] Blinov, B. B., Moehring, D. L., Duan, L.-M., and Monroe, C. Observation of entanglement between a single trapped atom and a single photon. *Nature*, **428** 153–157 (2004).

[87] Darquié, B., Jones, M. P. A., Dingjan, J., Beugnon, J., Bergamini, S., Sortais, Y., Messin, G., Browaeys, A., and Grangier, P. Controlled single-photon emission from a single trapped two-level atom. *Science*, **309** 454–456 (2005).

[88] Santori, C., Fattal, D., Vučković, J., Solomon, G. S., and Yamamoto, Y. Indistinguishable photons from a single-photon device. *Nature*, **419** 594 – 597 (2002).

[89] Gaebel, T., Popa, I., Gruber, A., Domhan, M., Jelezko, F., and Wrachtrup, J. Stable single-photon source in the near infrared. *New Journal of Physics*, **6** 98 (2004).

[90] Grangier, P. e. Focus on single photons on demand. *New Journal of Physics*, **6** (2004).

[91] Brune, M., Schmidt-Kaler, F., Maali, A., Dreyer, J., Hagley, E., Raimond, J. M., and Haroche, S. Quantum Rabi oscillation: A direct test of field quantization in a cavity. *Phys. Rev. Lett.*, **76** 1800–1803 (1996).

[92] Murr, K. On the suppression of the diffusion and the quantum nature of a cavity mode. Optical bistability: Forces and friction in driven cavities. *J. Phys. B*, **36** 2515 (2003).

[93] Hennrich, M. *Kontrollierte Erzeugung einzelner Photonen in einem optischen Resonator hoher Finesse*. Ph.D. thesis, Max-Planck-Institut für Quantenoptik und Technische Universität München (2003).

[94] Schuster, I. *Nonlinear spectroscopy of single atom-cavity system*. Ph.D. thesis, Max-Planck-Institut für Quantenoptik und Technische Universität München (2008).

[95] Plenio, M. B. and Knight, P. L. The quantum-jump approach to dissipative dynamics in quantum optics. *Rev. Mod. Phys.*, **70** 101–144 (1998).

[96] Hennrich, M., Legero, T., Kuhn, A., and Rempe, G. Vacuum-stimulated raman scattering based on adiabatic passage in a high-finesse optical cavity. *Phys. Rev. Lett.*, **85** 4872–4875 (2000).

[97] Brecha, R. J., Orozco, L. A., Raizen, M. G., Xiao, M., and Kimble, H. J. Observation of oscillatory energy exchange in a coupled-atom-cavity system. *J. Opt. Soc. Am. B*, **12** 2329 (1995).

[98] Mielke, S. L., Foster, G. T., Gripp, J., and Orozco, L. A. Time response of a coupled atoms-cavity system. *Opt. Lett.*, **22** 325–327 (1997).

[99] Haroche, S., Paisner, J. A., and Schawlow, A. L. Hyperfine quantum beats observed in cs vapor under pulsed dye laser excitation. *Phys. Rev. Lett.*, **30** 948–951 (1973).

[100] Wilk, T., Webster, S. C., Kuhn, A., and Rempe, G. Single-atom single-photon quantum interface. *Science*, **317** 488–490 (2007).

[101] DiFidio, C., Vogel, W., Khanbekyan, M., and Welsch, D.-G. Photon emission by an atom in a lossy cavity. *Phys. Rev. A*, **77** 043822 (2008).

[102] Moehring, D. L., Maunz, P., Olmschenk, S., Younge, K. C., Matsukevich, D. N., Duan, L.-M., and Monroe, C. Entanglement of single-atom quantum bits at a distance. *Nature*, **449** 68 (2007).

[103] Kubanek, A., Ourjoumtsev, A., Schuster, I., Koch, M., Pinkse, P. W. H., Murr, K., and Rempe, G. Two-photon gateway in one-atom cavity quantum electrodynamics. *Phys. Rev. Lett.*, **101** 203602 (2008).

[104] Duan, L.-M., Madsen, M. J., Moehring, D. L., Maunz, P., Kohn, Jr., R. N., and Monroe, C. Probabilistic quantum gates between remote atoms through interference of optical frequency qubits. *Phys. Rev. A*, **73** 062324 (2006).

[105] Lan, S.-Y., Jenkins, S. D., Chaneliere, T., Matsukevich, D. N., Campbell, C. J., Zhao, R., Kennedy, T. A. B., and Kuzmich, A. Dual-species matter qubit entangled with light. *Phys. Rev. Lett.*, **98** 123602 (2007).

[106] Schön, C., Solano, E., Verstraete, F., Cirac, J. I., and Wolf, M. M. Sequential generation of entangled multiqubit states. *Phys. Rev. Lett.*, **95** 110503 (2005).

[107] Terraciano, M. L., Olson Knell, R., Norris, D. G., Jing, J., Fernandez, A., and Orozco, L. A. Cavity-based single atom preparation and high-fidelity hyperfine state readout. *Nature Phys.*, **5** 480–484 (2009).

[108] Takeuchi, M., Takei, N., Zhang, P., Ueda, M., and Kozuma, M. Single nuclear spin cavity qed. *arXiv:0907.0336v3 [quant-ph]* (2009).

[109] Khudaverdyan, M., Alt, W., Kampschulte, T., Reick, S., Thobe, A., Widera, A., and Meschede, D. Quantum jumps and spin dynamics of interacting atoms in a strongly coupled atom-cavity system. *Phys. Rev. Lett.*, **103** 123006 (2009).

[110] Boozer, A. D., Boca, A., Miller, R., Northup, T. E., and Kimble, H. J. Cooling to the ground state of axial motion for one atom strongly coupled to an optical cavity. *Phys. Rev. Lett.*, **97** 083602 (2006).

[111] Gehr, R., Volz, J., Dubois, G., Steinmetz, T., Colombe, Y., Lev, B. L., Long, R., Estève, J., and Reichel, J. Cavity-based single atom preparation and high-fidelity hyperfine state readout. *Phys. Rev. Lett.*, **104** 203602 (2010).

[112] Kuhr, S., Alt, W., Schrader, D., Dotsenko, I., Miroshnychenko, Y., Rauschenbeutel, A., and Meschede, D. Analysis of dephasing mechanisms in a standing-wave dipole trap. *Phys. Rev. A*, **72** 023406 (2005).

[113] Volz, J., Weber, M., Schlenk, D., Rosenfeld, W., Vrana, J., Saucke, K., Kurtsiefer, C., and Weinfurter, H. Observation of entanglement of a single photon with a trapped atom. *Phys. Rev. Lett.*, **96** 030404 (2006).

[114] Yavuz, D. D., Kulatunga, P. B., Urban, E., Johnson, T. A., Proite, N., Henage, T., Walker, T. G., and Saffman, M. Fast ground state manipulation of neutral atoms in microscopic optical traps. *Phys. Rev. Lett.*, **96** 063001 (2006).

[115] Jones, M. P. A., Beugnon, J., Gaëtan, A., Zhang, J., Messin, G., Browaeys, A., and Grangier, P. Fast quantum state control of a single trapped neutral atom. *Phys. Rev. A*, **75** 040301 (2007).

[116] Rosenfeld, W., Weber, M., Volz, J., Henkel, F., Krug, M., Cabello, A., Zukowski, M., and Weinfurter, H. Towards a Loophole-Free Test of Bell's Inequality with Entangled Pairs of Neutral Atoms. *Advanced Science Letters*, **2** 469–474 (2009).

[117] Blatt, R. and Zoller, P. Quantum jumps in atomic systems. *Eur. J. Phys.*, **9** 250–256 (1988).

[118] Blatt, R., Häffner, H., Roos, C. F., Becher, C., and Schmidt-Kaler, F. Ion trap quantum computing with Ca^+ ions. *Quantum Inf. Proc.*, **3** 61–73 (2004).

[119] Acton, M., Brickman, K.-A., Haljan, P. C., Lee, P. J., Deslauriers, L., and Monroe, C. Near-perfect simultaneous measurement of a qubit register. *Quant. Inf. Comp.*, **6** 465–482 (2006).

[120] Hume, D. B., Rosenband, T., and Wineland, D. J. High-fidelity adaptive qubit detection through repetitive quantum nondemolition measurements. *Phys. Rev. Lett.*, **99** 120502 (2007).

[121] Olmschenk, S., Younge, K. C., Moehring, D. L., Matsukevich, D. N., Maunz, P., and Monroe, C. Manipulation and detection of a trapped yb hyperfine qubit. *Phys. Rev. A*, **76** 052314 (2007).

[122] Myerson, A. H., Szwer, D. J., Webster, S. C., Allcock, D. T. C., Curtis, M. J., Imreh, G., Sherman, J. A., Stacey, D. N., Steane, A. M., and Lucas, D. M. High-fidelity readout of trapped-ion qubits. *Phys. Rev. Lett.*, **100** 200502 (2008).

[123] Tey, M. K., Chen, Z., Aljunid, S. A., Chng, B., Huber, F., Maslennikov, G., and Kurtsiefer, C. Strong interaction between light and a single trapped atom without the need for a cavity. *Nature Phys.*, **4** 924–927 (2008).

[124] Maunz, P., Puppe, T., Schuster, I., Syassen, N., Pinkse, P. W. H., and Rempe, G. Normal-mode spectroscopy of a single-bound-atom˘cavity system. *Phys. Rev. Lett.*, **94** 033002 (2005).

[125] Fortier, K. M., Kim, S. Y., Gibbons, M. J., Ahmadi, P., and Chapman, M. S. Deterministic loading of individual atoms to a high-finesse optical cavity. *Phys. Rev. Lett.*, **98** 233601 (2007).

[126] Lodewyck, J., Westergaard, P. G., and Lemonde, P. Nondestructive measurement of the transition probability in a sr optical lattice clock. *Phys. Rev. A*, **79** 061401 (2009).

[127] Weber, B., Specht, H. P., Müller, T., Bochmann, J., Mücke, M., Moehring, D. L., and Rempe, G. Photon-photon entanglement with a single trapped atom. *Phys. Rev. Lett.*, **102** 030501 (2009).

[128] Harris, S. E. Electromagnetically induced transparency. *Phys. Today*, **50** 36–42 (1997).

[129] Lukin, M. D. Colloquium: Trapping and manipulating photon states in atomic ensembles. *Rev. Mod. Phys.*, **75** 457–472 (2003).

[130] Kasapi, A., Jain, M., Yin, G. Y., and Harris, S. E. Electromagnetically induced transparency: Propagation dynamics. *Phys. Rev. Lett.*, **74** 2447–2450 (1995).

[131] Hau, L. V., Harris, S. E., Dutton, Z., and Behroozi, C. H. Light speed reduction to 17 metres per second in an ultracold atomic gas. *Nature*, **397** 594–598 (1999).

[132] Fleischhauer, M. and Lukin, M. D. Dark-State Polaritons in Electromagnetically Induced Transparency. *Phys. Rev. Lett.*, **84** 5094–5097 (2000).

[133] Hammerer, K., Mølmer, K., Polzik, E. S., and Cirac, J. I. Light-matter quantum interface. *arXiv*, pages quant–ph/0312156 (2003).

[134] Julsgaard, B., Sherson, J., Cirac, I., Fiurassek, J., and Polzik, E. S. Experimental demonstration of quantum memory for light. *Nature*, **432** 482 – 486 (2004).

[135] Chaneliere, T., Matsukevich, D. N., Jenkins, S. D., Lan, S. Y., Kennedy, T. A. B., and Kuzmich, A. Storage and retrieval of single photons transmitted between remote quantum memories. *Nature*, **438** 833–836 (2005).

[136] Bajcsy, M., Hofferberth, S., Balic, V., Peyronel, T., Hafezi, M., Zibrov, A. S., Vuletic, V., and Lukin, M. D. Efficient all-optical switching using slow light within a hollow fiber. *Phys. Rev. Lett.*, **102** 203902 (2009).

[137] Fleischhauer, M., Imamoglu, A., and Marangos, J. P. Electromagnetically induced transparency: Optics in coherent media. *Rev. Mod. Phys.*, **77** 633–673 (2005).

[138] Werner, M. J. and Imamoglu, A. Photon-photon interactions in cavity electromagnetically induced transparency. *Phys. Rev. A*, **61** 011801 (1999).

[139] Rebic, S., Tan, S. M., Parkins, A. S., and Walls, D. F. Large kerr nonlinearity with a single atom. *J. Opt. B: Quantum Semiclass. Opt.*, **1** 490–495 (1999).

[140] Bermel, P., Rodriguez, A., Johnson, S. G., Joannopoulos, J. D., and Soljačić, M. Single-photon all-optical switching using waveguide-cavity quantum electrodynamics. *Phys. Rev. A*, **74** 043818 (2006).

[141] Cardimona, D. A., Alsing, P. M., Mozer, H., and Rhodes, C. Interference effects in a three-level atom in a cavity beyond the weak-field approximation. *Phys. Rev. A*, **79** 063817 (2009).

[142] Rebic, S., Parkins, A. S., and Tan, S. M. Photon statistics of a single-atom intracavity system involving electromagnetically induced transparency. *Phys. Rev. A*, **65** 063804 (2002).

[143] Nikoghosyan, G. and Fleischhauer, M. Photon-number selective group delay in cavity induced transparency. *arXiv:0910.1900* (2009).

[144] Hartmann, M. J., Brandao, F. G. S. L., and Plenio, M. B. Strongly interacting polaritons in coupled arrays of cavities. *Nature Phys.*, **2** 849–855 (2006).

[145] Greentree, A. D., Tahan, C., Cole, J. H., and Hollenberg, L. C. L. Quantum phase transitions of light. *Nature Phys.*, **2** 856–861 (2006).

[146] Lukin, M. D., Fleischhauer, M., Scully, M. O., and Velichansky, V. L. Intracavity electromagnetically induced transparency. *Opt. Lett.*, **23** 295–297 (1998).

[147] Hernandez, G., Zhang, J., and Zhu, Y. Vacuum rabi splitting and intracavity dark state in a cavity-atom system. *Phys. Rev. A*, **76** 053814 (2007).

[148] Wu, H., Gea-Banacloche, J., and Xiao, M. Observation of intracavity electromagnetically induced transparency and polariton resonances in a doppler-broadened medium. *Phys. Rev. Lett.*, **100** 173602 (2008).

[149] Carruthers, P. and Nieto, M. M. Phase and angle variables in quantum mechanics. *Rev. Mod. Phys.*, **40** 411–440 (1968).

[150] Lvovsky, A. I. and Raymer, M. G. Continuous-variable optical quantum-state tomography. *Rev. Mod. Phys.*, **81** 299–332 (2009).

[151] Kuhn, A., Hennrich, M., and Rempe, G. Deterministic single-photon source for distributed quantum networking. *Phys. Rev. Lett.*, **89** 067901 (2002).

[152] Legero, T., Wilk, T., Hennrich, M., Rempe, G., and Kuhn, A. Quantum beat of two single photons. *Phys. Rev. Lett.*, **93** 070503 (2004).

[153] Wilk, T., Webster, S. C., Specht, H. P., Rempe, G., and Kuhn, A. Polarization-controlled single photons. *Phys. Rev. Lett.*, **98** 063601 (2007).

[154] Wilk, T. *Single-Atom Single-Photon Quantum Interface*. Ph.D. thesis, Max-Planck-Institut für Quantenoptik und Technische Universität München (2008).

[155] Knill, E., Laflamme, R., and Milburn, G. J. A scheme for efficient quantum computing with linear optics. *Nature*, **409** 46–52 (2001).

[156] Kok, P., Munro, W. J., Nemoto, K., Ralph, T. C., Dowling, J. P., and Milburn, G. J. Linear optical quantum computing with photonic qubits. *Rev. Mod. Phys.*, **79** 135–174 (2007).

[157] Hong, C. K., Ou, Z. Y., and Mandel, L. Measurement of Subpicosecond Time Intervals between Two Photons by Interference. *Phys. Rev. Lett.*, **59** 2044 – 2046 (1987).

[158] Shih, Y. H. and Alley, C. O. New Type of Einstein-Podolsky-Rosen-Bohm experiment using pairs of light quanta produced by optical parametric down conversion. *Phys. Rev. Lett.*, **61** 2921 – 2924 (1988).

[159] Kwiat, P. G., Steinberg, A. M., and Chiao, R. Y. Observation of a "quantum eraser": A revival of coherence in a two-photon interference experiment. *Phys. Rev. A*, **45** 7729–7739 (1992).

[160] Herzog, T. J., Kwiat, P. G., Weinfurter, H., and Zeilinger, A. Complementarity and the quantum eraser. *Phys. Rev. Lett.*, **75** 3034–3037 (1995).

[161] Pittman, T. B., Strekalov, D. V., Migdall, A., Rubin, M. H., Sergienko, A. V., and Shih, Y. H. Can two-photon interference be considered the interference of two photons? *Phys. Rev. Lett.*, **77** 1917–1920 (1996).

[162] Legero, T., Wilk, T., Kuhn, A., and Rempe, G. Time-Resolved Two-Photon Quantum Interference. *Appl. Phys. B*, **77** 797–802 (2003).

[163] Legero, T. Ph.D. thesis, Technische Universitat Munchen (2005).

[164] Förster, L., Karski, M., Choi, J.-M., Steffen, A., Alt, W., Meschede, D., Widera, A., Montano, E., Lee, J. H., Rakreungdet, W., *et al.* Microwave control of atomic motion in optical lattices. *Phys. Rev. Lett.*, **103** 233001 (2009).

[165] Simon, C. and Irvine, W. T. M. Robust long-distance entanglement and a loophole-free bell test with ions and photons. *Phys. Rev. Lett.*, **91** 110405 (2003).

[166] van Enk, S. J., Cirac, J. I., and Zoller, P. Purifying two-bit quantum gates and joint measurements in cavity QED. *Phys. Rev. Lett.*, **79** 5178–5181 (1997).

[167] Yi, X. X., Su, X. H., and You, L. Conditional quantum phase gate between two 3-state atoms. *Phys. Rev. Lett.*, **90** (2003).

[168] Duan, L. M., Wang, B., and Kimble, H. J. Robust quantum gates on neutral atoms with cavity-assisted photon scattering. *Phys. Rev. A*, **72** 032333 (2005).

[169] Mekhov, I. B. and Ritsch, H. Quantum nondemolition measurements and state preparation in quantum gases by light detection. *Phys. Rev. Lett.*, **102** 020403 (2009).

[170] van Enk, S., Cirac, J. I., Zoller, P., Kimble, H. J., and Mabuchi, H. Quantum state transfer in a quantum network: A quantum optical implementation. *J. Mod. Opt.*, **44** 1727 (1997).

[171] Olmschenk, S., Matsukevich, D. N., Maunz, P., Hayes, D., Duan, L.-M., and Monroe, C. Quantum Teleportation Between Distant Matter Qubits. *Science*, **323** 486–489 (2009).

[172] Briegel, H.-J., Dür, W., Cirac, J. I., and Zoller, P. Quantum repeaters: The role of imperfect local operations in quantum communication. *Phys. Rev. Lett.*, **81** 5932–5935 (1998).

[173] Bernhardt, B., Haensch, T. W., and Holzwarth, R. Implementation and characterization of a stable optical frequency distribution system. *Optics Express*, **17** 16849–16860 (2009).

Publications

- "Electromagnetically induced transparency with single atoms in a cavity",
  M. Mücke, E. Figueroa, J. Bochmann, C. Hahn, K. Murr, S. Ritter, C. J. Villas-Boas, and G. Rempe,
  Nature **465**, 755 (2010).

- "Lossless state detection of single neutral atoms",
  J. Bochmann, M. Mücke, C. Guhl, S. Ritter, G. Rempe, and D. L. Moehring,
  Physical Review Letters **104**, 203601 (2010).

- "Phase shaping of single-photon wave packets",
  H. P. Specht, J. Bochmann, M. Mücke, B. Weber, E. Figueroa, D. L. Moehring, and G. Rempe,
  Nature Photonics **3**, 469 (2009).

- "Photon-photon entanglement with a single trapped atom",
  B. Weber, H. P. Specht, T. Müller, J. Bochmann, M. Mücke, D. L. Moehring and G. Rempe,
  Physical Review Letters **102**, 030501 (2009).

- "Fast excitation and photon emission of a single-atom-cavity system",
  J. Bochmann, M. Mücke, G. Langfahl-Klabes, C. Erbel, B. Weber, H. P. Specht, D. L. Moehring and G. Rempe,
  Physical Review Letters **101**, 223601 (2008).

Acknowledgment

This work has truly been a team effort to which many people contributed in many different ways. Foremost, I would like to thank Gerhard Rempe for his continued support.

I have had the pleasure to receive postdoctoral advice and lots of encouragement from Axel Kuhn, Simon Webster, David Moehring, Eden Figueroa, Stephan Ritter and Karim Murr. I thank "my" diploma students Gunnar Langfahl-Klabes, Christoph Erbel and Christoph Guhl for their friendship, enthusiasm and creative ideas. I appreciate the help I received from Bernhard Weber, Thomas Rieger and Niels Syassen in my first steps of setting up a new experiment. I acknowledge the outstanding work by Stefan Nußmann and Axel Kuhn who devised the prototype of this setup. Tom Wiesmeier, Josef Bayerl, Franz Denk and Helmut Stehbeck provided excellent technical support. I also thank Birgitta Bernhardt, Thomas Udem and Ronald Holzwarth for providing a frequency comb signal.

Certainly one of the best things that happened was Martin Mücke's decision to join this experiment in 2007. I'm glad to have shared the lab not only with a brilliant co-worker but also with a good friend.

I want to thank all current and past members of Gerhard Rempe's group and all the friends I made at MPQ for the great time I had.